

REPORT DOCUMENTATION PAGE

Public reporting burden for this collection of information is estimated to average 1 hour per response, including the time for reviewing instructions, collecting and maintaining data, preparing the report, and reviewing the collection of information. Send comments regarding this burden estimate or any other aspect of this collection of information, to the Office of Management and Operations and Reports, 1215 Jefferson Davis Highway, Suite 1204, Arlington, VA 22202-4302, and to the Office of Management and

imploring and reviewing
for information

1. AGENCY USE ONLY (Leave blank)		2. REPORT DATE	3. REPORT TYPE AND DATES COVERED	
		1 October 1999	Final Technical Report (1 Jul 97 to 30 Jun 99)	
4. TITLE AND SUBTITLE		5. FUNDING NUMBERS		
Focused Application Software for Ferrite Patch Antennas		F49620-97-C-0022		
6. AUTHOR(S)		8. PERFORMING ORGANIZATION REPORT NUMBER		
Dr. Keith D. Trott Mr. Rene D. Guidry Mr. Christopher G. Repesh				
7. PERFORMING ORGANIZATION NAME(S) AND ADDRESS(ES)		10. SPONSORING/MONITORING AGENCY REPORT NUMBER		
Mission Research Corporation 147 John Sims Parkway Valparaiso, FL 32580		F49620-97-C-0022		
9. SPONSORING/MONITORING AGENCY NAME(S) AND ADDRESS(ES)		12a. DISTRIBUTION AVAILABILITY STATEMENT		
AFOSR/NM 801 N. Randolph St, Rm 732 Arlington, VA 22203-1977		Approved for Public Release; Distribution Unlimited.		
11. SUPPLEMENTARY NOTES		12b. DISTRIBUTION CODE		
13. ABSTRACT (Maximum 200 words) The objective of this Phase II effort was to develop computational electromagnetic (CEM) codes capable of modeling the radiation properties (pattern, input impedance, efficiency, and bandwidth) of conformal arrays printed on ferrite substrates or superstrates. The codes developed under this effort model inhomogeneous ferrites and dielectrics, non-planar surfaces, heterogeneous elements, complex feed mechanisms, and performance control devices such as shorting pins and lumped loads. The FE-BI codes (brick and tetrahedral elements) are combined by MRC via a graphical user interface (GUI) into a user-friendly code capable of modeling conformal antennas with ferrite sub- and superstrates recessed in planar surfaces.				
14. SUBJECT TERMS			15. NUMBER OF PAGES	
			16. PRICE CODE	
17. SECURITY CLASSIFICATION OF REPORT		18. SECURITY CLASSIFICATION OF THIS PAGE	19. SECURITY CLASSIFICATION OF ABSTRACT	20. LIMITATION OF ABSTRACT
UNCLASSIFIED		UNCLASSIFIED	UNCLASSIFIED	UL

Standard Form 298 (Rev. 2-89) (EG)
Prescribed by ANSI Std. Z39-18
Designed using Perform Pro, WHS/DIOR, Oct 94

0001

Focused Application Software for Ferrite Patch Antennas

R&D Final Report for Phase II SBIR

Reporting Period: 1 July 97-1 July 99

Contract Number: F49620-97-C-0022

SBIR Topic: AF96-003

MRC Project: 97054

Prepared by:

Dr. Keith D. Trott, Mr. Rene D. Guidry, and Mr. Christopher G. Repesh
Mission Research Corporation
147 John Sims Parkway
Valparaiso, FL 32580

Dr. John L. Volakis, Mr. Arik D. Brown, Mr. Lars Andersen, and Ms. Zhifang Li
Radiation Laboratory
University of Michigan
1301 Beal Ave
Ann Arbor, MI 48109-2122

Dr. Hoton H. How and Dr. Carmine Vittoria
ElectroMagnetic Applications, Inc
300 Commercial St., Suite 805
Boston, MA 02109

“Distribution is authorized to DoD agencies only, as the data is PROPRIETARY (see section 5.8 of DoD SBIR program solicitation 96.1).” Requests for release shall be referred to AFOSR/NM.

Table of Contents

A. INTRODUCTION.....	1
B. OBJECTIVE.....	1
C. BACKGROUND	2
C.1 FERRITE MATERIALS.....	2
C.1.1 <i>Ferrite Material Model</i>	2
C.1.2 <i>Propagation Constants</i>	5
C.2 THE FINITE ELEMENT (FE) METHOD	5
C.2.1 <i>Finite Element Formulation for Anisotropic Materials</i>	6
C.2.2 <i>Finite Element-Boundary Integral Formulation for Anisotropic Materials</i>	8
D. TASKS.....	11
D.1 TASK 1. DEVELOPMENT OF FINITE ELEMENT (FE) ANALYSIS ENGINES	11
D.1.1 <i>Enhancement of Brick-FFT (FE-BI) Code</i>	11
D.1.2 <i>Development of PRISM Code</i>	12
D.1.3 <i>Development of Perfectly Matched Layer (PML) Mesh Closure</i>	16
D.1.4 <i>Development of Static magnetic Field H_0 Model</i>	16
D.2 TASK 2. VALIDATION OF COMPUTER CODES.....	16
D.2.1 <i>Ferrite Antenna Design and Fabrication</i>	16
D.2.2 <i>Ferrite Antenna Measurements</i>	17
D.2.3 <i>Comparison of Computed Data with Measured Data</i>	17
D.3 TASK 3: EXPLORATION OF FERRITE ANTENNA CAPABILITIES.....	23
D.3.1 <i>Ferrite Antenna Optimization</i>	24
D.3.2 <i>Applications</i>	25
D.4 TASK 4: INTEGRATION OF FE ENGINES WITH GRAPHICAL USER INTERFACE (GUI).....	29
D.4.1 <i>Graphical User Interface (GUI)</i>	30
E. PUBLISHED PAPERS.....	34
F. RESEARCHERS AND STUDENTS SUPPORTED	37
F.1 MISSION RESEARCH CORPORATION (MRC).....	37
F.2 UNIVERSITY OF MICHIGAN	37
F.3 ELECTROMAGNETIC APPLICATIONS, INC, (EMA)	37
G. INVENTIONS.....	37
H. CONCLUSIONS AND SUGGESTIONS FOR FUTURE WORK	37
H.1 CONCLUSIONS	37
H.2 SUGGESTIONS FOR FUTURE WORK.....	37
I. REFERENCES.....	38
APPENDIX A: USER'S MANUAL FOR THE MRC GRAPHICAL USER INTERFACE.....	39
APPENDIX B: USER'S MANUAL FOR FEMTETRA: A TETRAHEDRAL FE-BI CODE	50
APPENDIX C: USER'S MANUAL FOR MR_TETRA: MULTI-RESOLUTION FE-BI CODE.....	85
APPENDIX D: USER'S MANUAL FOR STRUCTURED 2D AND 3D MESHING	102

Table of Figures

FIGURE C-1: ILLUSTRATION OF MAGNETIC LINE WIDTH (AFTER POZAR [1])	4
FIGURE C-2: COMPUTATIONAL VOLUME (V), BOUNDING SURFACE (S), AND RADIATION CONDITION SURFACE (S ₀)	7
FIGURE C-3: ILLUSTRATION OF A CAVITY-BACKED APERTURE LOCATED IN AN INFINITE GROUND PLANE.	10
FIGURE C-4. VARIOUS FINITE ELEMENT SHAPES.....	11
FIGURE D-1: TETRAHEDRAL ELEMENT DEFINED WITH SIMPLEX VOLUME COORDINATES	13
FIGURE D-2: GEOMETRY FOR CAVITY-BACKED PATCH ANTENNA WITH AN AIR DIELECTRIC	14
FIGURE D-3: REAL AND IMAGINARY IMPEDANCE SPECTRUM FOR THE AIR-FILLED ANTENNA.....	15
FIGURE D-4: GEOMETRY FOR FERRITE-FILLED CAVITY-BACKED PATCH ANTENNA.	15
FIGURE D-5: REAL AND IMAGINARY IMPEDANCE SPECTRUM FOR THE FERRITE-LOADED ANTENNA	16
FIGURE D-6: FERRITE PHASE SHIFTER GEOMETRY WITH YIG/GGG/YIG SUBSTRATES	18
FIGURE D-7: INSERTION LOSS AND PHASE SHIFT FOR OUR X-BAND FERRITE PHASE SHIFTER. <i>CALCULATIONS ARE SOLID LINES WHILE MEASUREMENTS ARE THE CIRCLES AND SQUARES.</i>	19
FIGURE D-8: DESIGNS FOR 4-ELEMENT FERRITE ARRAY. <i>REGION IV IS THE FERRITE MATERIAL. MAXIMUM PHASE SHIFT OCCURS FOR THE RIGHT-MOST ELEMENT</i>	21
FIGURE D-9: NOVEL FOUR-ELEMENT FERRITE PHASE SHIFTER. <i>THE DARK WEDGE IS THE FERRITE MATERIAL. DESIGN ELIMINATES THE NEED FOR A SEPARATE PHASE SHIFTER FOR EACH CHANNEL OF THE ANTENNA. PHOTO ON THE RIGHT SHOWS THE ARRAY INSTALLED IN MAGNETIC BIASING CIRCUIT.</i>	22
FIGURE D-10: MEASURED (SOLID) AND CALCULATED (DOTTED) PATTERNS FOR TWO DIFFERENT BIAS LEVELS OF THE FOUR-ELEMENT PHASED ARRAY. <i>EXTERNAL BIAS FIELD FOR LEFT PLOT IS 4750 Oe AND RIGHT PLOT IS 4920 Oe. MEASUREMENT AND CALCULATION VERIFY THE FERRITE PHASE SHIFTER IS CAPABLE OF SCANNING A BEAM BY VARYING THE STRENGTH OF THE STATIC BIAS FIELD.</i>	22
FIGURE D-11: MEASURED MAIN BEAM PROPERTIES PLOTTED AS A FUNCTION OF THE EXTERNAL BIAS FIELD	23
FIGURE D-12: GEOMETRY OF THE CAVITY-BACKED PATCH ANTENNA.....	26
FIGURE D-13: RESONANT FREQUENCY FOR THE PATCH IN FIGURE D-12 AS A FUNCTION OF THE BIAS FIELD AND SATURATION MAGNETIZATION (NORMAL BIAS).	26
FIGURE D-14: RESONANT FREQUENCY FOR THE PATCH IN FIGURE D-12 AS A FUNCTION OF THE BIAS FIELD AND SATURATION MAGNETIZATION (X-BIAS).	27
FIGURE D-15: RESONANT FREQUENCY FOR THE PATCH IN FIGURE D-12 AS A FUNCTION OF THE BIAS FIELD AND SATURATION MAGNETIZATION (Y-BIAS).	27
FIGURE D-16: GEOMETRY OF THE CAVITY-BACKED PATCH ANTENNA FOR THE BEAM STEERING PROBLEM.	28
FIGURE D-17: GEOMETRY OF A SINGLE PATCH UNDER A FERRITE COVER LAYER (SUPERSTRATE).	28
FIGURE D-18: SCANNING OF SINGLE PATCH AT 6.180GHz: Y-BIAS, $\phi = 0$ CUT, 3 VARIABLES.....	28
FIGURE D-19: SCANNING OF SINGLE PATCH AT 6.9GHz: Y-BIAS, $\phi = 0$ CUT. ONLY H_0 IS VARIED, WITH $H_{SF} = 0.2$ CM, AND $4\pi M_s = 1300$ G	29
FIGURE D-20: GUI CAVITY FOLDER SCREEN. <i>BASIC PARAMETERS FOR CAVITY AND PATCH GEOMETRY ARE ENTERED</i>	31
FIGURE D-21: GEOVIEW OUTPUT FOR A PATCH EXAMPLE. <i>DISPLAYS THE PATCH AND THE NODE NUMBERS. NODE NUMBERS ARE NEEDED TO DETERMINE THE FEED LOCATIONS. RED INDICATES THE PATCH LOCATION.</i>	31
FIGURE D-22: GUI MATERIAL FOLDER SCREEN. <i>SETS UP THE MATERIAL AND FERRITE PROPERTIES</i>	32
FIGURE D-23: GUI OBSERVATION FOLDER SCREEN. <i>WHERE OBSERVATION PARAMETERS ARE ENTERED</i>	32
FIGURE D-24: GUI SIMULATION FOLDER SCREEN. <i>WHERE THE DESIRED SIMULATION PARAMETERS ARE SET. IN THIS CASE, THE FEM ANALYSIS IS BEING ACCOMPLISHED.</i>	33
FIGURE D-25: GUI POSTPROCESSING FOLDER SCREEN. <i>A PATCH IMPEDANCE PLOT IS SHOWN.</i>	33

List of Tables

TABLE D-1: FE CODE DEVELOPMENT STATUS.....	11
TABLE D-2: SUMMARY OF CASES USING DIFFERENT EDGE LENGTHS AND ORDER OF BASIS FUNCTIONS (AIR)	14

A. Introduction

Under this Phase II SBIR effort, Mission Research Corporation (MRC), the University of Michigan (UM), and ElectroMagnetic Applications, Inc. (EMA) undertook a study involving the application of recent innovations in the finite element (FE) method to the problem of modeling conformal antennas embedded in or on (substrate or superstrate) ferrite materials.

Ferrite materials have been suggested by the antenna community as a unique antenna loading material due to its tunable electrical properties. In particular, by appropriate application of a static magnetic bias field, a ferrite sample can exhibit a wide variety of electrical properties from nearly transparent to nearly opaque without mechanical intervention. Ferrites can also be magnetically tuned to preferentially interact with a given electromagnetic field polarization. For example, the sample can appear to be opaque to one polarization while transparent to the orthogonal polarization. Such properties can be exploited by antenna and low observable (LO) designers. This will be discussed in Section C.1

The finite element (FE) method (FEM) is uniquely suitable for analyzing the properties of ferrite materials since the FEM is typically formulated in the frequency domain, and hence can readily accommodate the frequency-dependent properties of ferrites. In addition, since the FEM requires no Green's function for the ferrite volume, its formulation and implementation is particularly straightforward. Also, since the finite element method is based on partial differential equations (PDEs), it possesses a locality property such that only field expansions in the near vicinity of one another couple directly. All of these features lead to the conclusion that the FEM is well suited for ferrite material modeling.

The FE method also permits considerable geometrical flexibility (unlike the FD-TD method) and it has been used to model very complex interior geometries such as waveguide junctions and cavities. However, unlike the integral equation (IE) method, a direct enforcement of the radiation condition must be imposed in order to arrive at a unique solution for open domain problems such as antenna radiation and scattering calculations. An alternative is to use a surface integral equation to close the mesh, thus creating a hybrid approach using the best qualities of the FE and IE methods. Hybrid finite element methods (HFEM) have been explored for several years, most often being called either the finite element-boundary integral (FE-BI) or the finite element-integral equation (FE-IE) method which combines the finite element and integral equation methods. The MRC Team has been a leading innovator in custom FE-BI solutions for antenna analysis. FE-BI is the only leading CEM technology capable of providing the geometric fidelity, efficiency, and accuracy required for demanding conformal antenna design and characterization. This will be discussed in more detail in Section C.2

B. Objective

The objective of this Phase II effort was to develop computational electromagnetic (CEM) codes capable of modeling the radiation properties (pattern, input impedance, efficiency, and bandwidth) of conformal arrays printed on ferrite substrates or superstrates. The codes developed under this effort model inhomogeneous ferrites and dielectrics, non-planar surfaces, heterogeneous elements, complex feed mechanisms, and performance control devices such as shorting pins and lumped loads. The FE-

BI codes (brick and tetrahedral elements) are combined by MRC via a graphical user interface (GUI) into a user-friendly code capable of modeling conformal antennas with ferrite sub- and superstrates recessed in planar surfaces.

This final technical report presents a comprehensive technical summary of this work. For completeness, the report begins with a discussion of ferrite materials, followed by a discussion of the basic finite element method. This is followed by a discussion of the accomplishments for each task: Development of FE Engines, Validation, Exploration of Capabilities, and Development of the GUI. Some specific results are discussed in detail; however, since most of the work appears in the many published journal articles and conference papers listed Section 0 and the dissertations and theses supported listed in Section F, many accomplishments are only summarized. The deliverables are the computer codes and the various user manuals. Each user manual is given as an appendix to this report.

C. Background

C.1 Ferrite Materials

Low-loss, thin-film frequency agile (ferrite and ferroelectric) materials provide the ability to vary the material properties by varying the applied bias field. A ferrite material's effective permeability (μ_{eff}) is varied by changing the applied magnetic field; whereas, a ferroelectric material's effective permittivity (ϵ_{eff}) is varied by changing the applied electric field. Ferrite antennas are conformal antenna elements with a ferrite loading material typically as either a sub- or superstrate. This thin-film ferrite substrate or superstrate can be used for phase shifting to steer the array. These antennas may be planar or singly-curved and are flush-mounted. Ferrite loading of the antenna offers many flexibility enhancements to the traditional conformal antenna element. It has been shown that ferrite-loaded antennas offer the following advantages over dielectric-loaded antennas:

- Single feed point circular polarization
- Polarization agility
- Frequency agility
- Miniaturization
- Beam steering without phase shifting circuitry
- Reduced radar cross section using the ferrite properties to create a shutterable radome

These ferrite antenna features are all achieved through judicious selection of the ferrite material and the application of an appropriately oriented static magnetic bias field (\mathbf{H}_0).

C.1.1 Ferrite Material Model

Ferrite materials exhibit dispersive properties that can be manipulated by adjusting the strength and orientation of a static magnetic bias field; that is, the material "looks" different to a dynamic field as the static "control" field is altered. In this section, the ferrite material model will be presented along with a discussion of some important parameters and terms. The most common representation of the material properties of a ferrite involves a scalar permittivity (typically fairly large ~9 to 16) and a

tensor permeability. The tensor permeability has different forms depending on the orientation of the applied static bias field (e.g. polarized longitudinal or transverse to the direction of propagation).

The Pölder tensors for the three Cartesian directions are given by

$$\begin{aligned}\bar{\bar{\mu}}_r &= \begin{bmatrix} 1 & 0 & 0 \\ 0 & \mu & j\kappa \\ 0 & -j\kappa & \mu \end{bmatrix} \quad x\text{-bias} \\ \bar{\bar{\mu}}_r &= \begin{bmatrix} \mu & 0 & j\kappa \\ 0 & 1 & 0 \\ -j\kappa & 0 & \mu \end{bmatrix} \quad y\text{-bias} \\ \bar{\bar{\mu}}_r &= \begin{bmatrix} \mu & j\kappa & 0 \\ -j\kappa & \mu & 0 \\ 0 & 0 & 1 \end{bmatrix} \quad z\text{-bias}\end{aligned}\quad (1)$$

where μ and κ are given by

$$\mu = \left(1 + \frac{\omega_0 \omega_m}{\omega_0^2 - \omega^2} \right) = \left(1 + \frac{f_0 f_m}{f_0^2 - f^2} \right) \quad (2)$$

$$\kappa = \left(\frac{\omega \omega_m}{\omega_0^2 - \omega^2} \right) = \left(\frac{f f_m}{f_0^2 - f^2} \right) \quad (3)$$

and $\omega = 2\pi f$. The Pölder tensors given above assume the $e^{+j\omega t}$ time convention.

In (2) and (3), several different important frequencies are defined. The operating frequency is denoted by f . The Lamor or precession frequency is indicated by f_0 , while the precession frequency is represented by f_m . The precession frequency in MHz is given by

$$f_0^{\text{MHz}} = 2.8 \times H_0, \quad (4)$$

where H_0 is the applied static magnetic bias field *within the ferrite sample* and in (4) this quantity is assumed to be given in terms of Oersteds (Oe). Note, H_0 is not necessarily equal to the external applied static magnetic field (H_e) since, for practical sample geometries, demagnetization may occur such that $H_0 \leq H_e$ depending on sample geometry and applied field orientation. The interested reader is encouraged to review Pozar's chapter concerning ferrite materials for further details¹. The precession frequency in MHz is given by

¹ D.M. Pozar, Microwave Engineering, New York, Addison-Wesley, 1990.

$$f_m^{\text{MHz}} = 2.8 \times (4\pi M_s) \quad (5)$$

where the saturation magnetization ($4\pi M_s$) is assumed to be given in Gauss. M_s is the peak magnetization achieved within a ferrite sample as an increasingly strong static bias field is applied; therefore, it represents an important intrinsic material property of ferrites. The permeability represented by the combination of (2) and (3) assumes no magnetic loss. To include such loss, a line width is typically defined. The line width, (ΔH), represents a spread or distribution around the bias. The effect is to modify (4) by including an imaginary component

$$f_0^{\text{MHz}} = 2.8 \times \left(H_0 + j \frac{\Delta H}{2} \right); \quad (6)$$

therefore, the precession frequency is now complex. Line width (ΔH) is illustrated in Figure C-1.

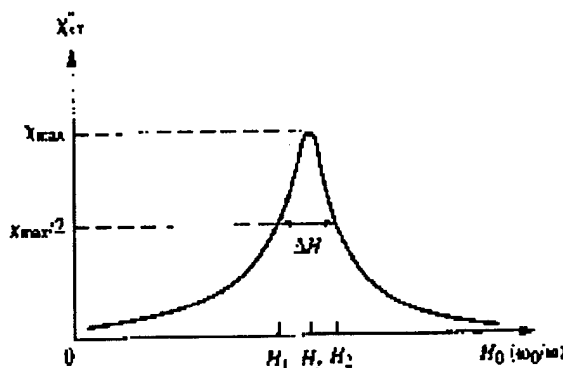


Figure C-1: Illustration of magnetic line width (After Pozar [1])

Several interesting phenomena arise as a result of the various frequency parameters associated with a ferrite material (e.g. f_0 , f_m , H_0 , ΔH , and $4\pi M_s$). For example, when the operating frequency is equal to the precession frequency $f = f_0$, a gyromagnetic or ferromagnetic resonance (FMR) occurs and the ferrite permeability is infinite. Since the skin depth is inversely proportional to the permeability, at the gyromagnetic resonance, the field cannot penetrate into the ferrite sample and the ferrite sample becomes very lossy. This condition cannot occur when a magnetic loss is included since the precession frequency becomes complex while the operating frequency remains real. Another interesting phenomena occurs when the effective permeability becomes zero. At this frequency, a ferromagnetic anti-resonance (FMAR) occurs and the skin depth is infinite. Hence, the ferrite is perfectly transparent. These are both narrow band effects, however, there is some hope for extending these effects over a wider bandwidth and this is a subject of future research.

C.1.2 Propagation Constants

There are two separate cases that determine the effective permeability (μ_{eff}) within the ferrite – the longitudinal case where the propagation is parallel to the applied bias field and the transverse case where propagation is orthogonal to the applied bias field. In the longitudinal or normally biased case, we have two circularly polarized waves whose μ_{eff} is defined by

$$\mu_{\text{eff}} = \mu \pm \kappa. \quad (7)$$

The $\mu_{\text{eff}} = \mu + \kappa$ is related to propagation of the right-hand circularly polarized (RHCP) wave and the $\mu_{\text{eff}} = \mu - \kappa$ is related to propagation of the left-hand circularly polarized (LHCP) wave. These are the natural modes of the normally biased ferrite.

In the transverse case, we have two linearly polarized waves known as the ordinary and extraordinary waves. The ordinary wave is independent of the bias field; whereas, the extraordinary wave's μ_{eff} is defined by

$$\mu_{\text{eff}} = \frac{\mu^2 - \kappa^2}{\mu}. \quad (8)$$

For both cases, the propagation constant within the ferrite is calculated as

$$\gamma = j\omega \sqrt{\epsilon_0 \mu_0 \epsilon_r \mu_{\text{eff}}} = jk_0 \sqrt{\epsilon_r \mu_{\text{eff}}} = \alpha + j\beta. \quad (9)$$

Ferrite materials, due to their Hermitian (complex conjugate, transposed) tensor structure, exhibit several interesting features. The polarization properties depend on the orientation of the applied bias field as shown in (7) and (8). For example, if we assume z-directed propagation, for a z-bias or longitudinal-bias condition, ferrite materials “look” different to RHCP and LHCP polarized fields. Hence, the propagation velocity, loss, and other physical effects are different. This property suggests various special uses for ferrites in antenna design and adaptive integrated electronics. Alternatively, depending on the transverse bias state, a ferrite material can look nearly transparent to one linear polarization and nearly opaque to its orthogonal polarization.

C.2 The Finite Element (FE) Method

The FE method permits considerable geometrical flexibility (unlike the FD-TD method) and it has been used to model very complex interior geometries such as waveguide junctions and cavities. However, unlike the integral equation (IE) method, a direct enforcement of the radiation condition must be imposed in order to arrive at a unique solution for open domain problems such as antenna radiation and scattering calculations.

An alternative is to use a surface integral equation to close the mesh, thus creating a hybrid approach using the best qualities of the FE and IE methods. Hybrid finite element methods (HFEM) have been explored for several years, most often being called either the finite element-boundary integral (FE-BI)

or the finite element-integral equation (FE-IE) method which combines the finite element and integral equation methods. A general FE-IE method is not currently feasible because electric and magnetic currents are needed on the mesh boundary as well as the three components of the interior field. All IE formulations result in full matrices due to global coupling; hence, the two currents on the mesh boundary impose an excessive computational burden in terms of memory and compute cycles. Therefore, FE-IE formulations typically are restricted to specialized situations such as cavity-backed patches or slots recessed in an infinite metallic surface. In this case, the FE-IE method can be formulated such that it requires only one current (magnetic) over the apertures. This will be discussed further when the derivation is presented in Section C.2.2.

C.2.1 Finite Element Formulation for Anisotropic Materials

The finite element formulation presented herein is very general. It does not assume any particular element shape, expansion (or shape) function, or mesh termination condition. For practical analysis, the formulation will need to be specialized. Both MRC and UM used a boundary integral (BI) mesh closure; therefore, this special case is presented following the general discussion.

C.2.1.1 General Finite Element Formulation for Anisotropic Materials

The finite element formulation begins with Maxwell's equations

$$\nabla \times \mathbf{E}^{\text{int}} = -jk_0 Z_0 \bar{\bar{\mu}}_r \mathbf{H}^{\text{int}} \quad (10)$$

$$\nabla \times \mathbf{H}^{\text{int}} = +jk_0 Z_0 \bar{\bar{\epsilon}}_r \mathbf{E}^{\text{int}} \quad (11)$$

where the interior (e.g. within the computational volume) electric and magnetic fields are denoted by \mathbf{E}^{int} and \mathbf{H}^{int} , respectively. The relative permittivity ($\bar{\bar{\epsilon}}_r$) and permeability ($\bar{\bar{\mu}}_r$) are tensors and can vary on an element-by-element basis within the computational volume. The free-space wavenumber and impedance are denoted by $k_0 = \omega \sqrt{\mu_0 \epsilon_0}$ and $Z_0 = \sqrt{\mu_0 / \epsilon_0}$, respectively, where the free-space permittivity and permeability are represented by ϵ_0 and μ_0 , respectively. Pre-multiplying (10) by the inverse permeability tensor ($\bar{\bar{\mu}}_r^{-1}$), taking the curl of (10) and utilizing (11), the second-order PDE is obtained

$$\nabla \times [\bar{\bar{\mu}}_r^{-1} \cdot \nabla \times \mathbf{E}^{\text{int}}] - k_0^2 \bar{\bar{\epsilon}}_r \cdot \mathbf{E}^{\text{int}} = -[jk_0 Z_0 \mathbf{J}^{\text{imp}} + \nabla \times (\bar{\bar{\mu}}_r^{-1} \cdot \mathbf{M}^{\text{imp}})] \quad (12)$$

This is the vector wave equation in terms of the total electric field within the computational volume, V , illustrated in Figure C-2. In (12), \mathbf{J}^{imp} and \mathbf{M}^{imp} are the impressed electric and magnetic current within the computational volume, respectively, and the inverse permeability tensor is given by

$$\begin{aligned}
 \bar{\bar{\mu}}_r^{-1} &= \begin{bmatrix} 1 & 0 & 0 \\ 0 & \mu/\Delta & -j\kappa/\Delta \\ 0 & +j\kappa/\Delta & \mu/\Delta \end{bmatrix} \quad x\text{-bias} \\
 \bar{\bar{\mu}}_r^{-1} &= \begin{bmatrix} \mu/\Delta & 0 & -j\kappa/\Delta \\ 0 & 1 & 0 \\ +j\kappa/\Delta & 0 & \mu/\Delta \end{bmatrix} \quad y\text{-bias} \\
 \bar{\bar{\mu}}_r^{-1} &= \begin{bmatrix} \mu/\Delta & -j\kappa/\Delta & 0 \\ +j\kappa/\Delta & \mu/\Delta & 0 \\ 0 & 0 & 1 \end{bmatrix} \quad z\text{-bias}
 \end{aligned} \tag{13}$$

where the determinant is given by $\Delta = \mu^2 - \kappa^2$.

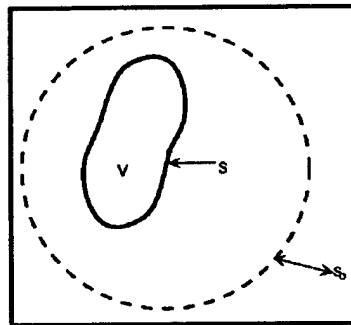


Figure C-2: Computational volume (V), bounding surface (S), and radiation condition surface (S₀).

Throughout this report, total electric fields will be the unknowns since the BI mesh closure used involved a half space Green's function (e.g. cavities recessed in an infinite metallic plane) and hence a total magnetic field formulation is impractical. This is not to say that a magnetic field formulation will not be preferable for ferrite materials. Indeed, the fact that a magnetic field formulation precludes the need for an inverse permeability tensor ($\bar{\bar{\mu}}_r^{-1}$) is desirable due to singularities in that tensor near the forced precession frequency.

Two methods are typically used to convert the continuous domain wave equation represented by (12) and a discrete approximation that can be solved on a digital computer: the method of functionals and method of weighted residuals. Throughout this report, the method of weighted residuals is used since it is familiar to electrical engineers that have used the method of moments. The method of weighted residuals begins by multiplying (12) with an arbitrary weight function (W_i^e) that has support only over one finite element (e). There are N such unique weights corresponding to the number of unknowns in the final system. After multiplication, (12) is integrated over the entire computational

volume (though of course the finite support of the weight functions will limit the integration to the element associated with the weight function) to get

$$\int_V \left\{ \mathbf{W}_i^e \cdot \nabla \times \left[\bar{\bar{\mu}}_r^{-1} \cdot \nabla \times \mathbf{E}^{int} \right] - k_0^2 \mathbf{W}_i^e \cdot \bar{\bar{\epsilon}}_r \cdot \mathbf{E}^{int} \right\} dV = \\ - \int_V \mathbf{W}_i^e \cdot \left[jk_0 Z_0 J^{imp} + \nabla \times \left(\bar{\bar{\mu}}_r^{-1} \cdot \mathbf{M}^{imp} \right) \right] dV = f_i^{e,int} \quad (14)$$

where the right-hand side (interior excitation) is represented by $f_i^{e,int}$ for the remainder of this report. This equation is not convenient for solution since the electric field receives two derivatives and the resulting formulation is unsymmetric. Therefore, it is advantageous to transfer one derivative from the unknown electric field to the weight function in the first integrand using the first vector Green's theorem

$$\int_V \mathbf{W}_i^e \cdot \nabla \times \left[\bar{\bar{\mu}}_r^{-1} \cdot \nabla \times \mathbf{E}^{in} \right] dV = \int_V \left(\nabla \times \mathbf{W}_i^e \right) \cdot \left(\bar{\bar{\mu}}_r^{-1} \cdot \nabla \times \mathbf{E}^{int} \right) dV - \oint_S \hat{\mathbf{n}} \cdot \left(\mathbf{W}_i^e \times \left[\bar{\bar{\mu}}_r^{-1} \cdot \nabla \times \mathbf{E}^{int} \right] \right) dS \quad (15)$$

Using (10) and a vector triple product, (15) becomes

$$\int_V \mathbf{W}_i^e \cdot \nabla \times \left[\bar{\bar{\mu}}_r^{-1} \cdot \nabla \times \mathbf{E}^{in} \right] dV = \int_V \left(\nabla \times \mathbf{W}_i^e \right) \cdot \left(\bar{\bar{\mu}}_r^{-1} \cdot \nabla \times \mathbf{E}^{int} \right) dV - jk_0 Z_0 \oint_S \mathbf{W}_i^e \cdot \left(\hat{\mathbf{n}} \times \mathbf{H}^{int} \right) dS \quad (16)$$

In this, the surface term relates the tangential electric field (\mathbf{W}_i^e) with the tangential magnetic field ($(\hat{\mathbf{n}} \times \mathbf{H}^{int})$) on the surface enclosing the volume (V) where $\hat{\mathbf{n}}$ is the outward directed normal to the surface S (∂V). Using (16) in (14), the weak-form of the vector wave equation is obtained

$$\int_V \left[\left(\nabla \times \mathbf{W}_i^e \right) \cdot \bar{\bar{\mu}}_r^{-1} \cdot \left(\nabla \times \mathbf{E}^{int} \right) - k_0^2 \mathbf{W}_i^e \cdot \bar{\bar{\epsilon}}_r \cdot \mathbf{E}^{int} \right] dV - jk_0 Z_0 \oint_S \mathbf{W}_i^e \cdot \left(\hat{\mathbf{n}} \times \mathbf{H}^{int} \right) dS = f_i^{e,int} \quad (17)$$

This equation satisfies (12) in the weak or integrated sense rather than at every point within the computational volume.

Finite element programs are typically divided into two groups based upon how the surface magnetic field is related to the surface electric field:

- locally through an approximate condition such as absorbing boundary conditions (ABC) or perfectly matched layers (PML), or
- globally via a boundary integral involving a dyadic Green's function for the external region.

During Phase II, both MRC and UM used the boundary integral method and its formulation is presented below.

C.2.2 Finite Element-Boundary Integral Formulation for Anisotropic Materials

The finite element-boundary integral formulation begins by postulating a magnetic field integral equation (MFIE) for the exterior region such as

$$\frac{\hat{\mathbf{n}} \times \mathbf{H}^{\text{ext}}(\mathbf{r})}{2} - \oint_S \hat{\mathbf{n}} \times \left(\nabla \times \bar{\bar{\mathbf{G}}} \cdot \hat{\mathbf{n}}' \times \mathbf{H}^{\text{ext}}(\mathbf{r}') \right) dS' - jk_0 Y_0 \oint_S \hat{\mathbf{n}} \times \bar{\bar{\mathbf{G}}} \cdot \hat{\mathbf{n}}' \times \mathbf{E}^{\text{ext}}(\mathbf{r}') dS = \hat{\mathbf{n}} \times \left[\mathbf{H}^{\text{inc}}(\mathbf{r}) + \mathbf{H}^{\text{ref}}(\mathbf{r}) \right] \quad (18)$$

where the field quantities are now in the exterior region (e.g. between S and S_0 in Figure C-2), the prime variable (\mathbf{r}') refers to the source point while the unprimed variable (\mathbf{r}) refers to the test point, and $Y_0 = 1/Z_0$. The excitation (the right-hand side) is separated in terms of an incident magnetic field (\mathbf{H}^{inc}) and a reflected magnetic field (\mathbf{H}^{ref}). For geometries involving an infinite metallic structure, this field representation is used. For geometries involving finite structures, the reflected field is omitted. For radiation analysis, both the incident and the reflected fields are omitted.

This MFIE is then tested with a separate vector test function (\mathbf{Q}_i^e)

$$\frac{1}{2} \oint_S \mathbf{Q}_i^e \cdot \hat{\mathbf{n}} \times \mathbf{H}^{\text{ext}} dS - \oint_S \oint_{S'} \mathbf{Q}_i^e \cdot \hat{\mathbf{n}} \times \left[\nabla \times \bar{\bar{\mathbf{G}}} \cdot \hat{\mathbf{n}}' \times \mathbf{H}^{\text{ext}} \right] dS' dS - jk_0 Y_0 \oint_S \oint_{S'} \mathbf{Q}_i^e \cdot \hat{\mathbf{n}} \times \left[\bar{\bar{\mathbf{G}}} \cdot \hat{\mathbf{n}}' \times \mathbf{E}^{\text{ext}} \right] dS' dS = \oint_S \mathbf{Q}_i^e \cdot \hat{\mathbf{n}} \times \left[\mathbf{H}^{\text{inc}} + \mathbf{H}^{\text{ref}} \right] dS = f_i^{e,\text{ext}} \quad (19)$$

and the interior and exterior fields are matched across the interface using either point-by-point coupling

$$\hat{\mathbf{n}} \times [\mathbf{E}^{\text{int}} - \mathbf{E}^{\text{ext}}] = 0 \quad \text{and} \quad \hat{\mathbf{n}} \times [\mathbf{H}^{\text{int}} - \mathbf{H}^{\text{ext}}] = 0 \quad (20)$$

or in an average sense

$$\oint_S \mathbf{Q}_i^e \cdot \hat{\mathbf{n}} \times [\mathbf{E}^{\text{int}} - \mathbf{E}^{\text{ext}}] dS = 0 \quad \text{and} \quad \oint_S \mathbf{Q}_i^e \cdot \hat{\mathbf{n}} \times [\mathbf{H}^{\text{int}} - \mathbf{H}^{\text{ext}}] dS = 0 \quad (21)$$

Although the formulation is appropriate for general structures, such as the one illustrated in Figure C-2, MRC and UM used a specialized FE-BI formulation for cavities recessed in an infinite ground plane, such as the one shown in Figure C-3, to save on computer resources. A general FE-IE method is not currently feasible because electric and magnetic currents are needed on the mesh boundary as well as the three components of the interior field. All IE formulations result in full matrices due to global coupling; hence, the two currents on the mesh boundary impose an excessive computational burden in terms of memory and compute cycles. Therefore, FE-IE formulations typically are restricted to specialized situations such as cavity-backed patches or slots recessed in an infinite metallic surface. In this case, the FE-IE method can be formulated such that it requires only one current (magnetic) over the apertures located within the ground plane or circular cylinder². Accordingly, the memory and computational requirements associated with the mesh boundary is minimized. In addition, very large apertures can be efficiently modeled by exploiting Toeplitz

² L.C. Kempel, J.L. Volakis, and R.J. Sliva, "Radiation by cavity-backed antennas on a circular cylinder," *IEE Proceedings, Pt. H*, 1995.

symmetry, present in the IE sub-matrix, provided these apertures lie in a metallic ground plane or circular cylinder and uniform sampling is used on the mesh boundary.

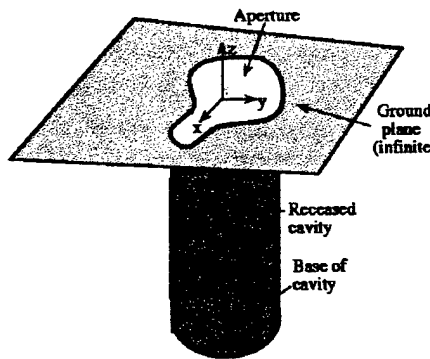


Figure C-3: Illustration of a cavity-backed aperture located in an infinite ground plane.

Such efficiency is important for performing an exhaustive investigation of potential ferrite antenna capabilities. This special formulation allowed the use of

$$\hat{\mathbf{z}} \times \mathbf{H}^{\text{ext}} = \hat{\mathbf{z}} \times [\mathbf{H}^{\text{inc}} + \mathbf{H}^{\text{re}}] + jk_0 Y_0 \oint_{S'} \hat{\mathbf{z}} \times \bar{\bar{\mathbf{G}}} \times \hat{\mathbf{z}} \cdot \mathbf{E}^{\text{ext}} dS' \quad (22)$$

where we have assumed that the metallic plane is at $z = 0$ and hence the normal unit vectors become $\hat{\mathbf{n}} = \hat{\mathbf{n}}' = \hat{\mathbf{z}}$. If identical expansion functions are used for both the exterior surface mesh and the interior volume mesh (that is the volume shape function reduces to the surface shape function as the evaluation point approaches the surface), this results in an implicit enforcement of (20), then (22) can be substituted into (17) yielding

$$\int_V [(\nabla \times \mathbf{W}_i^e) \cdot \bar{\bar{\mathbf{G}}}^{-1} \cdot (\nabla \times \mathbf{E}^{\text{int}}) - k_0^2 \mathbf{W}_i^e \cdot \bar{\bar{\epsilon}}_r \cdot \mathbf{E}^{\text{int}}] dV + k_0^2 \oint_{S'} \mathbf{W}_i^e \cdot [\hat{\mathbf{z}} \times \bar{\bar{\mathbf{G}}} \times \hat{\mathbf{z}}] \cdot \mathbf{E}^{\text{int}} = f_i^{\text{e,int}} + f_i^{\text{e,ext}} \quad (23)$$

which is the FE-BI equation used.

For cavities recessed in a metallic plane, the half-space dyadic Green's function is used in (23). This yields

$$\bar{\bar{\mathbf{G}}} = 2\bar{\bar{\mathbf{G}}}_0 = 2 \left[\bar{\bar{\mathbf{I}}} + \frac{\nabla \nabla}{k_0^2} \right] \mathbf{G}_0 = \left[\bar{\bar{\mathbf{I}}} + \frac{\nabla \nabla}{k_0^2} \right] \frac{e^{j k_0 |\mathbf{r} - \mathbf{r}'|}}{2\pi |\mathbf{r} - \mathbf{r}'|} \quad (24)$$

The FE-BI equation (22) is complete and it only remains to specify the finite elements and their associated shape functions. The FE method can use many different finite element shapes, MRC and UM have primarily used brick and tetrahedral elements shown in Figure C-4.

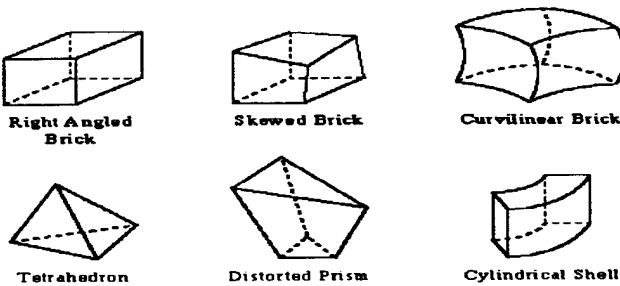


Figure C-4. Various finite element shapes.

D. Tasks

For each task we will begin with a summary of the accomplishments. Then we describe some important accomplishments and discoveries in more detail.

D.1 Task 1. Development of Finite Element (FE) Analysis Engines

Contractor shall develop a suite of codes, each of which will be optimized for particular antenna geometries. Many codes were developed under this project. The table below summarizes the various code capabilities.

Table D-1: FE Code Development Status

Code/Capability	Ferrite-Tetra linear elements	Ferrite-Tetra 2 nd order TVFE	Fema-Prism	Ferrite-Brick
ferrite	√	√		√
AIM	√		√	FFT (no need)
Auto meshing	√	√	√	√
Higher order TVFE		√		
PML (curved)	√ (not tested)			
Frequency Extrapolation	√		√	partial
SQP				√
Geometry/currents viewing	√	√	√	√ (GUI)

D.1.1 Enhancement of Brick-FFT (FE-BI) Code

Contractor shall develop a Brick-FFT code. This code will be used to support Advanced Waveform generator and Optimizers. The LM_Brick FE-BI code has been modified to model anisotropic gyromagnetic material. This code is called FERRITE. FERRITE forms the foundation of much of the work performed under this Phase II. It is one of the codes supported by the GUI and was used for the optimization work presented in a later section.

Status:

- FERRITE brick code incorporated into GUI (Appendix)
- Upgraded MRC's FERRITE brick code to include the flexible GMRES solver
- Added Preconditioning to the GMRES Solver
- Results with GMRES converged where BCG and LU
- Published paper based on results with GMRES

D.1.2 Development of PRISM Code

Contractor shall develop PRISM code. The prisms will be subdivided into tetrahedra. This code will enable analysis of doubly curved conformal antennas.

Status:

- Equipped PRISM code with GMRES solver
- Upgraded PRISM mesher for arbitrary rectangular and circular patches
- Mesher interfaced with visualization package MESHVIEW to view meshes (leveraged effort)
- Mesher upgraded to allow automated array modeling
- Completed and documented formulation of tetrahedral ferrite code
- PRISM used to model arrays to demonstrate beam steering
- Beam steering demonstrated
- Measurements carried out at UM to demonstrate changes in propagation constant as a function of applied bias
- Compared with PRISM calculations
- Completed and tested H-field (tetra) formulation of the eigenvalue problem with ferrite materials
- Code manual for PRISM written (Appendix)
- Used higher order hierarchical elements to solve problems with rapid field variations in ferrites
- Additional code called MR_TETRA developed which allows analysis of ferrite antennas using a mix of multiresolution elements (Discussed in Section D.1.2.1)
- MR_TETRA tested extensively. Provides for an excellent tool for accurate input impedance computations using only 2-3 percent of higher order elements within the domain
- Condition numbers of matrices based on multiresolution elements were studied and found quite good compared to previously available higher order elements
- Adaptivity was implemented in MR_TETRA. Permits the automated use of the code for including higher order elements based on predefined error criteria
- MR_TETRA includes AIM for speed-up of BI
- Documentation for MR_TETRA written
- Several papers published on multiresolution elements and their applications for antenna analysis.
- Code manual for MR_TETRA written (Appendix)
- Designed/modeled spiral antenna using combined distorted prisms and bricks (leveraged effort)
- Completed periodic array/frequency selective version of PRISM (FSS_PRISM) (leveraged effort)
- Included fast integral methods (AIM/FMM) in PRISM and FSS_PRISM (leveraged effort)
- Finished prism-to-tetra mesh geometry translation driver
- Incorporated optimizer into FERRITE Brick to track antenna resonance with biased substrates
- Doubly curved capability exists in PRISM using artificial absorber for mesh truncation. This option has not been extensively tested.

- Reduced order modeling and frequency extrapolation methods added to PRISM
- Two Ph.D. dissertations completed under this task

D.1.2.1 Multi Resolution FE-BI Code

In an effort to speed up the FEM calculations without sacrificing accuracy, mixed-order tangential vector finite elements (TVFE) for tetrahedral elements has been implemented [12]. TVFE guarantees tangential field continuity across element boundaries and suppresses spurious modes. The high order TVFE improves accuracy without requiring a finer mesh. Mixed order TVFE enables us to keep the same mesh size but model the ferrite region with high order TVFE to achieve greater accuracy (i.e., variable sampling). Consider a tetrahedral element with simplex/volume coordinates defined in the usual manner

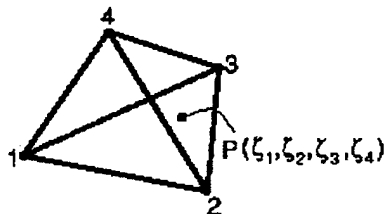


Figure D-1: Tetrahedral element defined with simplex volume coordinates

The number of vector basis functions for a mixed-order TVFE of order $n = 0.5$ is given by

$$N_n^{\text{tet}} = \frac{n(n+2)(n+3)}{2} \quad (25)$$

Therefore, a TVFE of order 0.5 has $n = 1$; hence, $N_1^{\text{tet}} = 6$ and the basis function is given by

$$\zeta_i \nabla \zeta_j - \zeta_j \nabla \zeta_i \quad i < j \quad (26)$$

A TVFE of order 1.5 has $n = 2$; therefore, $N_2^{\text{tet}} = 20$ and the higher order basis functions are given by

$$\zeta_i \nabla \zeta_j - \zeta_j \nabla \zeta_i \quad i < j \quad (27)$$

$$(\zeta_i - \zeta_j)(\zeta_i \nabla \zeta_j - \zeta_j \nabla \zeta_i) \quad i < j \quad (28)$$

$$\zeta_k (\zeta_i \nabla \zeta_j - \zeta_j \nabla \zeta_i) \quad i < j < k \quad (29)$$

$$\zeta_j (\zeta_k \nabla \zeta_i - \zeta_i \nabla \zeta_k) \quad i < j < k \quad (30)$$

These are called hierarchical basis functions because the lower order basis function is contained within the higher order set. This enables us to transition between higher order and lower order basis

function, using the higher order basis functions in regions of rapid fluctuations, and the lower order basis functions in smooth regions making this a multiresolution problem. Using these basis functions, an air dielectric case and a ferrite case have been analyzed to determine the improvement. With the mixed order basis function, the edge length could be decreased while maintaining the accuracy. The first case was the air dielectric case. The geometry is shown in Figure D-2.

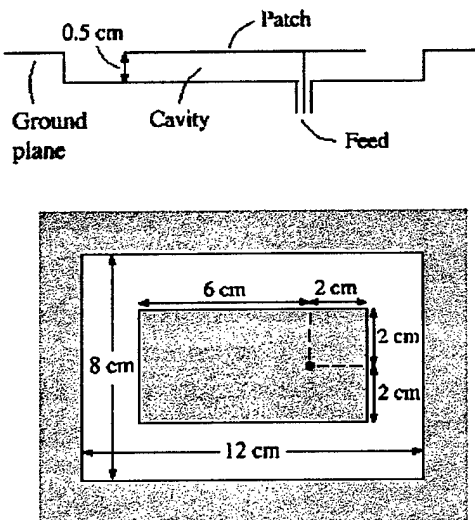


Figure D-2: Geometry for cavity-backed patch antenna with an air dielectric

Several different edge length and order combinations were run. These are shown in Table D-2.

Table D-2: Summary of cases using different edge lengths and order of basis functions (air)

Case	TVPE order(s)	Average edge length	# of unknowns	# of BI unknowns	# of matrix entries	Time per frequency point
1	0.5	1.09 cm	505	160	29607	12 sec
2	0.5	0.77 cm	1189	384	157291	107 sec
3	0.5	0.62 cm	2161	704	513807	501 sec
4	0.5/1.5	1.09 cm	1263	160	50989	32 sec

The plots are shown in Figure D-3. The difference in the calculation between case 3 and case 4 is insignificant; however, the difference in run time and unknowns is an order of magnitude.

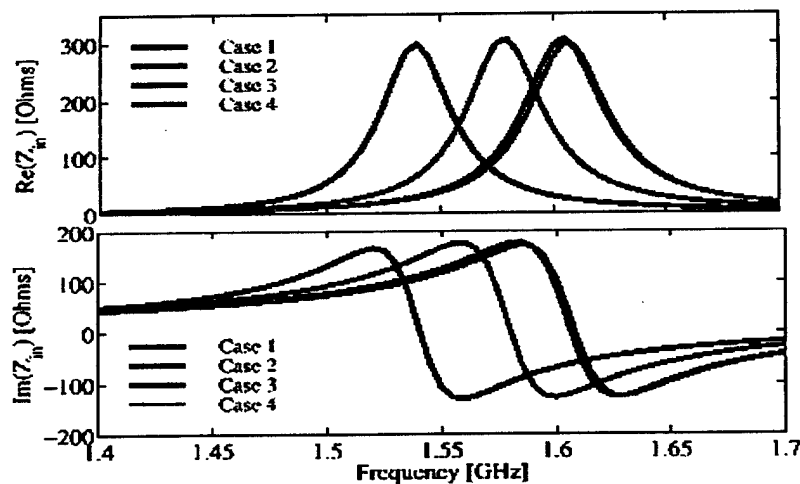


Figure D-3: Real and Imaginary impedance spectrum for the air-filled antenna

The next case is for a ferrite-loaded cavity-backed patch antenna. The geometry is shown in Figure D-4. The calculated data is shown in Figure D-5.

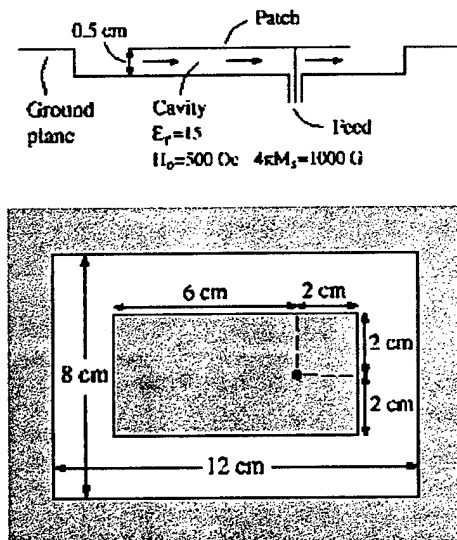


Figure D-4: Geometry for ferrite-filled cavity-backed patch antenna.

Note that the scale on Figure D-5 is such that the difference is not as much as it appears. Even though the plots for case 3 and case 4 look far apart, inspection of the scale shows that the difference in the peak location is only 0.0025 GHz (negligible). Once again showing the mixed order elements provide the same answer using a larger edge length which reduces the number of unknowns.

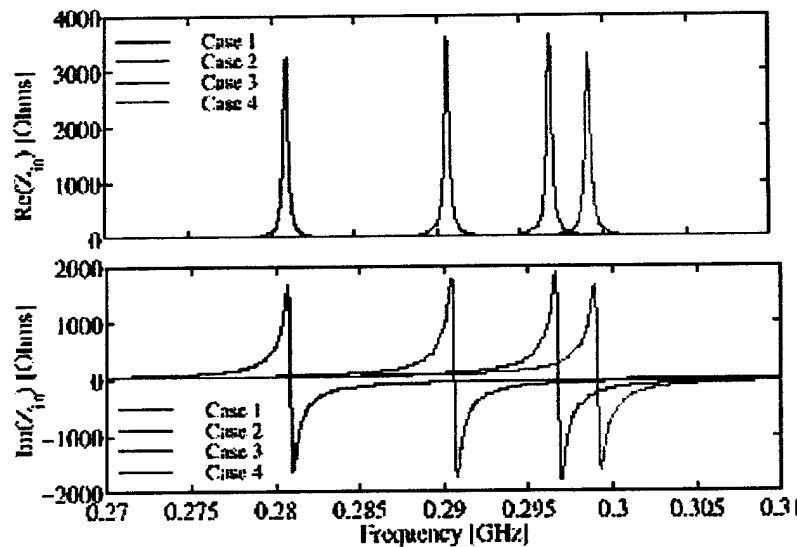


Figure D-5: Real and imaginary impedance spectrum for the ferrite-loaded antenna

D.1.3 Development of Perfectly Matched Layer (PML) Mesh Closure

Contractor shall develop PML mesh closure schemes for the codes developed in the above subtasks. The anisotropic PML will improve the capability and versatility of the FE codes.

Status:

- Tetra code using PML truncation (capability incorporated into code and mesher)
- Compared PML to FE-BI. PML was abandoned since it led to poorly conditioned systems. Better to have denser matrix than a poorly conditioned sparse matrix!!

D.1.4 Development of Static magnetic Field H_0 Model

Contractor shall develop a static magnetic field model for each of the codes developed. This solver will compute the non-constant magnetic field within the cavity to be used in the dynamic field analysis.

Status:

- EMA successful with techniques to ensure a uniform field across the patch
- Effort redirected to concentrate on validation of codes with measurements

D.2 Task 2. Validation of Computer Codes

D.2.1 Ferrite Antenna Design and Fabrication

Contractor shall design and fabricate various ferrite antennas to be used to validate the software. Ferrite Antenna Elements. EMA has built and measured the performance of circular patch antennas printed on a ferrite substrate. The substrate was biased using a permanent horseshoe magnet that provided a transverse magnetic field up to 1320 Oe in the central region of the substrate. Radiation patterns were measured in the two principal planes consisting of the main

feeder line or normal to the main feeder line, the H-plane and the E-plane, respectively. The antennas radiate in X-band (12 GHz) and the radiation patterns were measured using a HP-8510B network analyzer³.

Status:

- Fabricated 1.5-in x 1.5-in x .050-in circular and rectangular patch antennas
- Used transmission line feed with very high input impedance
- Built and measured phase shifter circuitry
- Fabricated 4x1 array using wedge ferrite phase shifter and meander line ferrite phase shifter (Discussed in Section D.2.3.1)
- 4x1 array with wedge phase shifter fabricated (discussed in Section D.2.3.2)
- 4x4 array fabrication abandoned due to biasing constraints

D.2.2 Ferrite Antenna Measurements

Contractor shall perform the following measurements, as a minimum, on the fabricated antennas and elements: input impedance versus frequency, voltage standing wave ratio versus frequency, gain at resonant frequency, and axial ratio.

Status:

- Measured 3-D contour plots of MRC's permanent magnets for bias field
- Designed/fabricated permanent magnets and yokes to provide uniform bias fields
 - Shaped magnet pairs—750 Oe over .4-in
 - Non-uniform magnetization— 1010 ± 110 Oe over 1-in.
 - Shaped Yoke rather than magnet—Variable field strength uniform $\pm 1\%$ over 2-in x 2-in area.
- Analyzed and measured phase shifter configurations to be used in arrays
- Measured 4x1 ferrite array (Discussed in Section D.2.3.2)

D.2.3 Comparison of Computed Data with Measured Data

Contractor shall compare the computed data with the measured data to determine the accuracy of the numerical computational technique. If the technique contains errors, the contractor shall inform the Government on measures to improve the comparison. Measurements were done on simple patches as well as ferrite arrays. We concentrated on the array problem. To that end, we first discuss the phase shifter circuitry followed by the application of the phase shifter to develop a steered array. This array was modeled with our codes and the results compared well for the main beam and the steering direction.

D.2.3.1 Novel Phase Shifter Technology

Phase shifters are often constructed in terms of frequency-agile materials whose electronic properties can be changed via the application of a voltage or a magnetic field. While it is possible to fabricate a phase shifter at low frequencies by using a ferroelectric substrate, say, below 5 GHz, it is not very feasible if the frequency is increased to X-band or beyond, since ferroelectric materials are generally lossy at high frequencies. At X-band and above, insertion losses are lower in ferrite substrates. By

³ H. How, T.M. Fang, W. Liu, and C. Vittoria, "Antenna array of circular patches on ferrite substrate," INTERMAG 96 Conference, April 1995, San Antonio, TX.

applying a bias magnetic field, the effective permeability of a ferrite substrate can be continuously changed, resulting in variable phase shifts for microwave signals propagating in a transmission line fabricated on a ferrite substrate.

The difficulty with using a ferrite substrate is the bias magnetic field is required to have a magnitude on the order of several thousand Oe to effectively change the permeability of the substrate at X-band frequencies. To achieve this, the bias field can be divided into two parts: the permanent part and the variable part. The permanent part of the bias field is furnished by using a permanent magnet, or, alternatively, by using the internal (uniaxial) anisotropy field of the substrate material, providing a constant background for magnetic biasing. The variable bias field is then superimposed to the permanent part, resulting in local variation of the bias field near its permanent field value. Ideally, the variable field should be small in magnitude in comparison to the permanent field, so the variable field can be conveniently obtained using a solenoid coil.

To reduce the bias current in the solenoid coil, and hence to enhance the switching speed of the phase shifter device and to lower power dissipation, the range that allows the variable bias field to change shall be kept as a minimum. For this purpose the bias condition is usually devised near ferromagnetic resonance (FMR). In the vicinity of FMR, the permeability of the ferrite material is a sensitive function of the bias field; hence, a slight change in the bias field results in a significant change in permeability. Ferrite phase shifters often utilize spinel or garnet ferrite materials. A typical phase shifter using nickel zinc ferrite exhibits the following properties: 360°/in, 1.38 lb/in, 17 GHz, and a drive current of 2 amps. This particular phase shifter, fabricated by S. Stitzer (1997 IEEE MTT Symposium Digest, p 117), is not a variable phase shifter, but a latched phase shifter such that the phase shift is fixed for a fixed operating frequency. We have fabricated a X-band phase shifter using

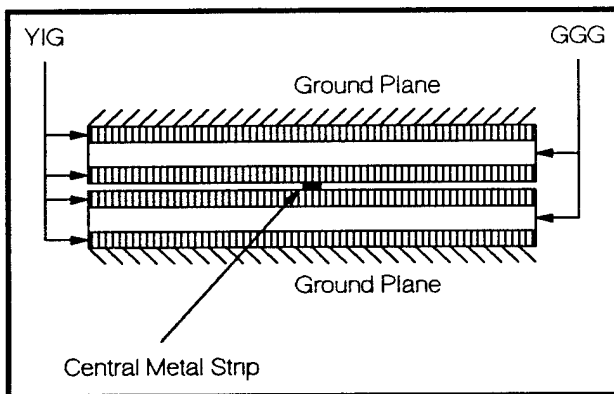


Figure D-6: Ferrite Phase Shifter Geometry with YIG/GGG/YIG substrates

single-crystal YIG/GGG/YIG substrate assemblies in the stripline geometry as shown in Figure D-6. The YIG/GGG/YIG material was purchased from Airtron, Charlotte, NC. The YIG films are of a nominal thickness of 100 μ m, which were epitaxially grown along the <111> direction on both sides of a GGG substrate (thickness 20 mil and dielectric constant 14.7).

The YIG films have the following parameters: saturation magnetization $4\pi M_s = 1750$ G, dielectric constant $\epsilon_r = 14.7$, anisotropy field $H_A = 82$ Oe, and an FMR line-width $\Delta H \approx 0.5$ Oe at 10 GHz. The dielectric loss-tangent for both YIG and GGG materials is 0.0002. Using the composite YIG/GGG/YIG materials as the substrate, a stripline circuit was fabricated. The stripline is of a length 0.782 cm, which is approximately one quarter wavelength long at 10 GHz in the absence of a bias magnetic field. The width of the central conductor strip is 0.0531 cm, corresponding to a characteristic impedance of 25Ω . The stripline circuit was connected to two air-filled quarter-wave transformers of an impedance of 35.4Ω . This device was then measured using a HP-8510B vector network analyzer. Figure D-7 shows the measured characteristics of the fabricated device. The phase shifter is a quarter wavelength in the absence of a bias magnetic field. The phase can be tuned 120° by varying the bias magnetic field from 3440 to 3720 Oe. The insertion loss variation is 0.5 dB.

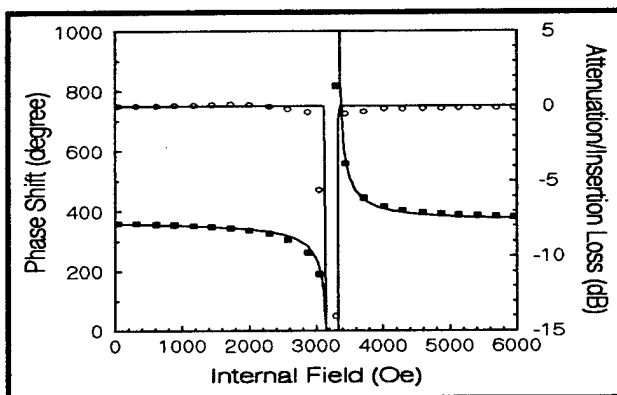


Figure D-7: Insertion loss and phase shift for our X-band ferrite phase shifter. Calculations are solid lines while measurements are the circles and squares.

The performance of the phase shifter was analyzed numerically by using the transfer-matrix theory in a transmission line. The transfer-matrix theory is usually used to translate the transverse electromagnetic boundary conditions occurring at one layer interface to another, expressing the continuity equation in the spectral domain. The formulation of the present problem is quite general, and can be applied to any planar-circuit geometries comprised of dielectric and magnetic layers biased not necessarily along the symmetry directions. First, we define a surface impedance matrix at a layer interface. The impedance matrices associated with an imperfect metal ground plane and an open half-space are then derived. A conventional transfer matrix correlates the tangential components of the RF-electromagnetic field over one layer thickness, the transformation of surface impedance can be defined, transforming the surface impedance matrix over one layer thickness. When two transfer matrices are multiplied, the associated impedance transformation will be compounded so the transformation is isomorphic to the multiplication of the two transfer matrices. As such, the surface impedance at the outermost surfaces of the layered structure can be translated to the plane(s) containing circuit inhomogeneities from which the (normal) metal boundary conditions can be applied and solved. The conventional transfer matrix technique can be found in Vittoria⁴.

⁴ C. Vittoria, Elements of Microwave Networks, World Scientific Publishing Co., Singapore, 1998

Our calculations compared very well with measurements. Details are available in preprints of our measurements and calculations⁵.

D.2.3.2 Steerable Ferrite Patch Antenna Arrays

Experience using electronically controlled phased arrays has shown high costs and fragility limit their impact on the user community for foreseeable future. As such, there is considerable interest in developing simpler, more robust and efficient antenna arrays. Traditional phased array antennas use individual ferrite phase shifters and delay lines that adjust the phase of each antenna element in a phased array to provide electronic steering. However, for large antenna arrays, the conventional delay line configuration is very bulky and requires multiple magnetic bias circuits to operate in unison. This large number of circuits results in excessive power consumption, and the complexity of such designs limits the scan rate of the antenna array. There is considerable interest in developing simpler, more robust technologies to increase reliability and to lower costs. To this end, we have fabricated a linear phased array antenna at X-band using single crystal yttrium-iron-garnet (YIG) as the frequency agile material adjusting the input phase of the elements. The array contains 4 square patches, connected to 4 stripline feeders with equal power. The feeders include YIG phase shifters whose output phases are progressively varied via an external magnetic field applied normal to the array substrate. The diagram is shown in Figure D-8. This results in one-dimensional steering of the radiated beam.

The fabricated antenna array consists of six regions. Region I has a width 2.5 inches and a length 0.0764 inches, containing a stripline of impedance 50Ω using air as the substrate/superstrate material. The stripline is connected to coax (OSM) launcher for microwave input. Region II, $2.5 \times 0.570 \text{ in}^2$, contains stripline power splitters, and the input microwave power is divided into 4 equal parts with minimal reflection. Region II is duroid (dielectric constant 2.2, thickness 0.031"; Rogers, Chandler, AZ) and is used as the substrate/superstrate material. Region V, $2.5 \times 0.199 \text{ in}^2$, includes 4 stripline transformers using the same duroid material as the substrate and the superstrate, and Region VI, $2.5 \times 0.75 \text{ in}^2$, contains 4 microstrip patches attached with feeders deposited on the same piece of the substrate extended from Region V. No superstrate is used in Region VI, radiating energy away from the antennas allowing measurements to be taken directly above Region VI. The microstrip patches are of a square geometry with dimension $0.388 \times 0.388 \text{ in}^2$.

Region IV contains the frequency agile material used to construct stripline phase shifters, and Region III is for phase compensation. That is, we require these two regions to have the same dielectric constant so we have equal phase at the input of the patch antennas in the absence of a bias magnetic field. The boundary between Regions VI and III is linearly tapered to provide progressive phase changes when the permeability of the substrate/superstrate of Region IV is varied. A bias field is applied normal to the substrate/superstrate surface. The magnitude of the bias field can be varied from 4000 to 8000 Oe. The magnetic field is supplied by using a pair of neodymium permanent magnets ($2 \times 2 \times 1 \text{ in}^3$) and the bias field can be varied by adjusting the gap distance of the yoke separation. The dielectric constant of the dielectric material used in Region III is 14 (Trans Tech, Adamstown, MD). The dimension of Region III plus Region IV is $2 \times 0.616 \text{ in}^2$.

⁵ H. How, W. Hu, L.C. Kempel, K. D. Trott, and C. Vittoria, "Phase Shifters at X-Band Using Single-Crystal YIG Films: Theory and Experiments," *IEEE Trans. Microwave Theory Tech.*, submitted, 1999.

As discussed in the phase shifter section, the frequency agile material used in Region IV is single-crystal YIG/GGG/YIG. The YIG/GGG/YIG material was purchased from Airtron, Charlotte, NC. The YIG films are of a nominal thickness of 100 μm , which were epitaxially grown along the $<111>$ direction on both sides of a single crystal GGG substrate (thickness 20 mil and dielectric constant 14.7). The YIG films are characterized by the following parameters: saturation magnetization $4\pi M_s = 1750$ G, dielectric constant $\epsilon_f = 14.7$, anisotropy field $H_A = 82$ Oe, and an FMR line-width $\Delta H \approx 0.5$ Oe at 10 GHz. The dielectric loss-tangent for both YIG and GGG materials is 0.0002.

Two designs were investigated as shown in Figure D-8. The first design used a wedge of thin-film ferrite to provide different path lengths through the ferrite to generate a progressive phase shift. The other used a meander line of different path lengths through the ferrite to provide a progressive phase shift between elements. In either case, this additional phase shift, controlled by an external static magnetic bias field, should cause the antenna beam to scan.

The ferrite wedge design was constructed and measured is shown in Figure D-9. It is possible to operate a ferrite phase shifter near FMR if the line width is narrow. Single crystal yttrium-iron-garnet (YIG) is an ideal material for fabrication of a 10 GHz phase shifter because it has a linewidth of $\sim .5$ Oe to 1 Oe at 10 GHz. This is the frequency agile material used to fabricate our four-element array. The two areas have similar dielectric constants so the phase would be equal when no bias is applied. The bias is normal to the substrate. The biasing circuit consists of a permanent magnet and solenoidal coils for adjustment and can be varied from 4000-8000 Oe. Measurements and calculations are shown in Figure D-10. The agreement between calculation and measurement is promising, in fact, it agrees very well for the peak of the beam and the steering direction. The first case steered to -17 degrees and the second to -41 degrees.

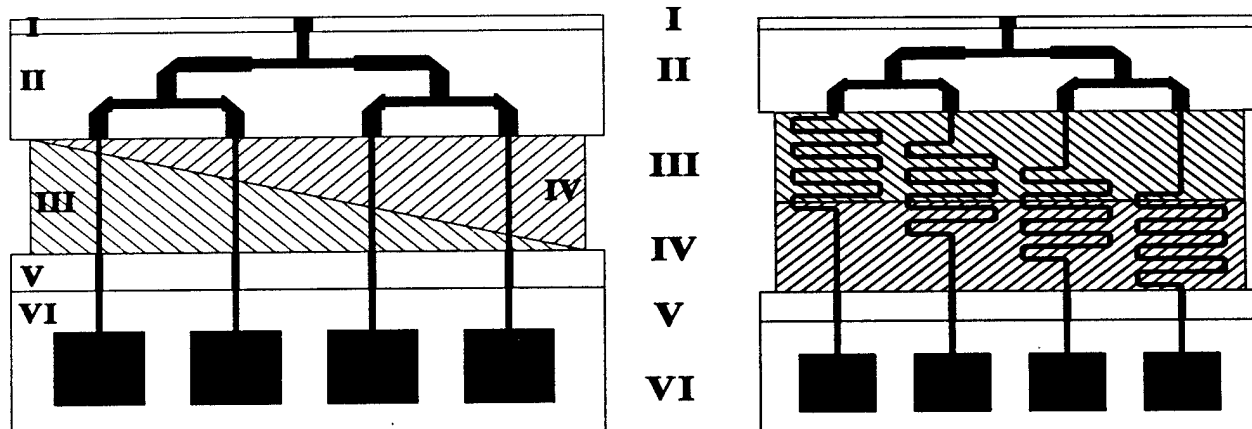


Figure D-8: Designs for 4-element Ferrite Array. Region IV is the Ferrite Material. Maximum phase shift occurs for the right-most element

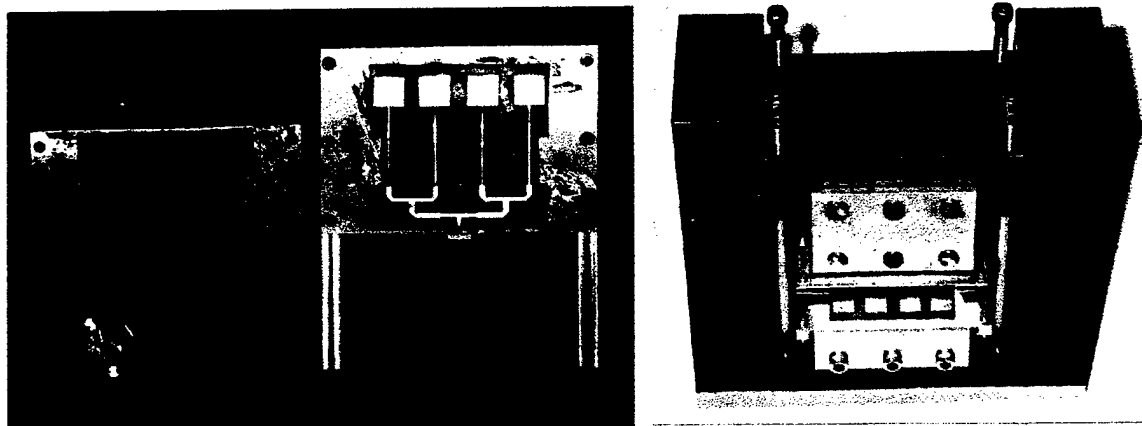


Figure D-9: Novel four-element ferrite phase shifter. *The dark wedge is the ferrite material. Design eliminates the need for a separate phase shifter for each channel of the antenna. Photo on the right shows the array installed in magnetic biasing circuit.*

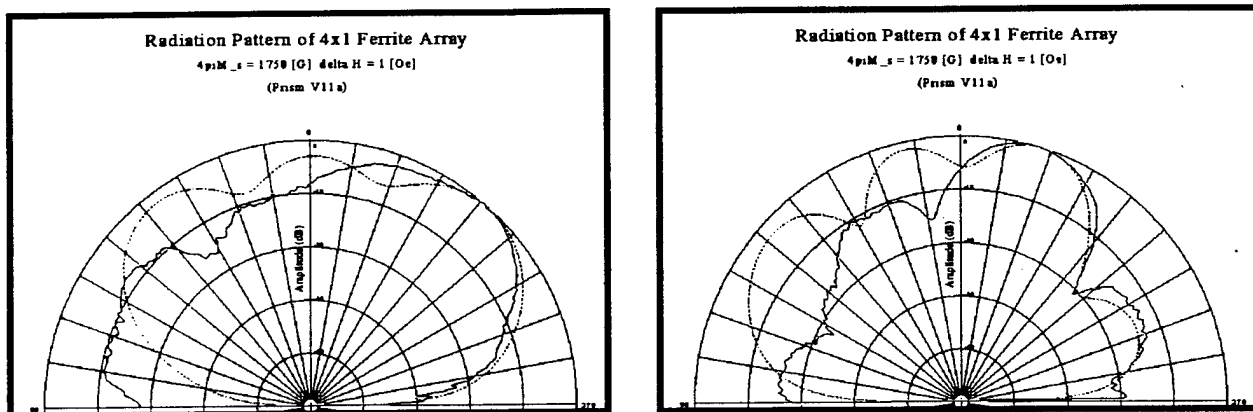


Figure D-10: Measured (solid) and calculated (dotted) patterns for two different bias levels of the four-element phased array. *External bias field for left plot is 4750 Oe and right plot is 4920 Oe. Measurement and calculation verify the ferrite phase shifter is capable of scanning a beam by varying the strength of the static bias field.*

One side effect of using this novel ferrite phase shifter was broadening of the beam. This is caused by non-progressive phase shifts between the antenna elements.

The radiation patterns for the antenna array were measured in an anechoic chamber located at Rome Laboratory, Hanscom, MA. The properties of the measured main-beam radiation are summarized in Figure D-11, where the location, the intensity, and the beam width, are plotted as a function of the applied bias-field strength, H_b . We see that useful radiation occurs when the bias field H_b is varied from 4920 to 5270 Oe, resulting in a beam steering angle of 15° without causing much beam broadening or attenuation.

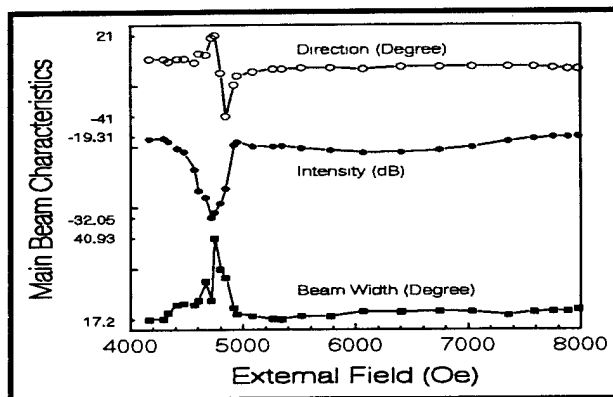


Figure D-11: Measured main beam properties plotted as a function of the external bias field

We conclude that practical phased array antennas operating at X-band and lower frequencies can be fabricated using single-crystal YIG material characterized by a narrow FMR line-width. While the transmission phase can be sensitively tuned by applying a bias magnetic field, the insertion loss through the phase shifters can be relatively constant and low level. In addition, it is necessary to bias the YIG-film material with a small variable field of magnitude ~ 100 Oe, which can be obtained using a solenoid coil. The discussion of our measurements and calculations is available as preprints⁶.

D.3 Task 3: Exploration of Ferrite Antenna Capabilities

Contractor shall use the validated codes to explore ferrite antenna capabilities:

- Non-uniform bias field effects
- Non-Cartesian bias field orientation effects
- Bias field effects on curved antennas
- Polarization and frequency diversity for planar and curved antennas
- Beam Steering capability for planar and curved antennas

Status:

- FERRITE brick code enhanced with design algorithms based on the SQP method for tracking resonances and designing subject to frequency, bandwidth, size, steering angle constraints (discussed in Section D.3.1)
- Several design examples were carried out to demonstrate the design algorithms
- Two papers published on design algorithms
- Dissertation halfway completed developing more robust algorithms for antenna design

⁶ H. How, C. Vittoria, M.H. Champion, L.C. Kempel, and K.D. Trott, "Steerable Phased Array Antennas Using Single-Crystal YIG Phase Shifters: Theory and Experiments," *IEEE Trans. Microwave Theory and Tech.*, submitted, 1999

D.3.1 Ferrite Antenna Optimization

We consider the effect of biased ferrite substrate on resonant frequency tuning and beam steering of patch antennas^{7,8}. The tools used will be the gradient-based optimization methods in conjunction with FE-BI method. The use of design optimization methods greatly facilitates the development of optimal performance antennas. Compared with traditional antenna designs, optimization processes not only decrease simulation time, but also save on hardware manufacturing costs by circumventing expensive trial and error processes.

D.3.1.1 Analysis and Synthesis Methods

The formal statement of a *constrained* design optimization problem can be written in the negative null form as

$$\text{Find } \mathbf{x} \quad \text{which minimizes } f(\mathbf{x}, \mathbf{p}) \quad (31)$$

$$\text{subject to } g(\mathbf{x}, \mathbf{p}) \leq 0 \quad (32)$$

$$h(\mathbf{x}, \mathbf{p}) = 0 \quad (33)$$

$$\mathbf{x} \in \chi \subseteq \mathbb{R}^n \quad (34)$$

where \mathbf{x} are called *design variables* with χ as *design space*; and \mathbf{p} are certain *parameters* with fixed values. $f(\mathbf{x}, \mathbf{p})$ is the *objective function*, $g(\mathbf{x}, \mathbf{p})$ are referred to as a group of *inequality constraints* and $h(\mathbf{x}, \mathbf{p})$ as *equality constraints*.

Typical gradient-based numerical optimization methods use iterative numerical searches to produce a sequence of improved approximations to reach a minimum. Starting with an initial point \mathbf{x}_0 where the function value is calculated, a direction is identified where the function value will be lower. This optimization phase is called **direction finding**. To find the direction of change using a gradient-based method (such as Newton's method), we must explore local information, especially gradient information in the vicinity of the evaluation point. Linear or quadratic approximations are employed, and controls on the amount of parameter movement along that direction may be imposed. Once the direction of movement is established, the next step is to determine a good value for the step size α_k (without violating any constraints). This phase of optimization algorithms is referred to as the **line search**. The goal of direction finding and line search is to create a sequence of points that converges to the minimum. Such a minimum may be interior to or on the boundary of the domain.

To conduct our study, we combined analysis and synthesis methods to obtain the desired antenna configurations. The antenna simulator is used by the optimizer. Here, the hybrid FE-BI (boundary integral) is used as the simulator to allow modeling of finite and inhomogeneous layers. The Bi-Conjugate (BiCG) solver is used to solve the general matrix system, but the general minimal residual (GMRES) altogether may be necessary in case BiCG experiences

⁷ D.M. Pozar, "Radiation and scattering characteristics of microstrip antennas on normally biased ferrite substrates," *IEEE Trans. Antennas Propagat.*, vol. 40, no. 9, pp. 1084-1092, Sept. 1992.

⁸ A. Henderson, J.R. James, and A. Fray, "Magnetized microstrip antenna with pattern control," *Electronics Letters*, vol. 24, no. 1, pp. 45-47, Jan. 1988.

convergence difficulties⁹. For the optimizer, the sequential quadratic programming (SQP) method is used¹⁰. This is a gradient-based optimization algorithm to find local optima and works well for continuous objective function. The search direction is found by solving a quadratic programming (QP) subproblem. The step size in that direction is determined by minimizing a one-dimensional penalty function along that direction. Computation of the pertinent gradients with SQP is important and is often done numerically (for example, by finite differences).

Basically, SQP algorithms have the following steps:

- Initialize.
- Solve the QP subproblem to determine a search direction s_k .
- Minimize a merit function along s_k to determine a step length α_k . The merit function should measure quality of current design variables and Lagrangian multipliers; thus, some form of penalty function is used that properly weighs objective function decrease and constraint violations.
- Set $\mathbf{x}_{k+1} = \mathbf{x}_k + \alpha_k s_k$.
- Check for termination. Go to step 2 if not satisfied.

D.3.2 Applications

D.3.2.1 Resonant Frequency Tuning

Biased ferrite substrates offer extra degrees of freedom for resonant frequency tuning. Also, circular polarization can be achieved with a single feed using a ferrite substrate (dielectric substrates cannot achieve this). We have verified this and obtained results in agreement with those in Pozar [7].

Because of the multitude of parameters, which control the resonance frequency of a ferrite patch, it is advantageous to use an optimizer to predict the resonant frequency of the ferrite patch. The optimization problem statement can be formulated as follows:

$$\text{Find } f, \quad \text{which minimizes } \text{Imag}(Z_{in}(f)) \quad (35)$$

$$\text{subject to} \quad f_L \leq f \leq f_U \quad (36)$$

where Z_{in} is the frequency-dependent input impedance and f_L / f_U refer to the lower / upper bounds of the frequency search. Here we use the definition that the antenna reaches resonance when the imaginary part of the input impedance is zero. In practice, the following objective function can also be used: Maximize $\text{Real}(Z_{in}(f))$.

⁹ A.D. Brown, J.L. Volakis, L.C. Kempel, and Z. Li, "Numerical analysis of the radiation properties of ferrite patch antennas," *Proc. of the 1998 IEEE Antennas and Propagation Society International Symposium*, Atlanta, Georgia, vol. 1, pp. 244-247, July 1998.

¹⁰ Z. Li, Panos Y. Papalambros, and J.L. Volakis, "Designing broadband patch antennas using the sequential quadratic programming method," *IEEE Transactions on Antennas and Propagation*, v.45, n.11, pp. 1689-1692, November 1997.

As an example, we consider an antenna with $L = W = 0.61\text{cm}$, $h = 0.127\text{cm}$, and $\epsilon_r = 15$. We place the antenna in a $1.22\text{cm} \times 1.22\text{cm}$ cavity, with a probe feed located at the mid-point of an edge as shown in Figure D-12. For this antenna, we note that for the isotropic substrate, the resonance occurs around 5.5GHz.

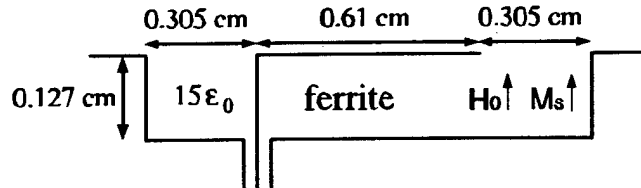


Figure D-12: Geometry of the cavity-backed patch antenna.

First, a normal biasing field is applied as in Pozar [7]. The results are shown in Figure D-13, and compared to those from Pozar [7], where the moment method (MoM) was used. We can draw the conclusion that our results are very consistent with the moment method data except for a slight shift in frequency. Basically we observe that the LHCP frequency is higher than the RHCP and that the resonant frequencies increase with increased normal biasing.

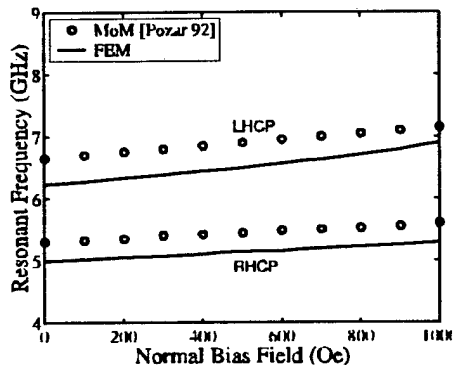


Figure D-13: Resonant frequency for the patch in Figure D-12 as a function of the bias field and saturation magnetization (normal bias).

Next, the antenna is also biased parallel to one of the edges of the patch. We solve the optimization problem (35) for various values of the bias field strength H_0 and saturation magnetization $4\pi M_s$. The results are plotted in Figure D-14 and Figure D-15 for x-bias (bias field perpendicular to the edge where the feed is located) and y-bias (bias field parallel to the edge where the feed is located), respectively. It is seen again that the resonant frequency of the antenna shifts to a higher frequency as H_0 or $4\pi M_s$ increases. However, x and y biasing provides linear polarization and greater dynamic range for frequency tuning. Also, the resonant frequencies for the y-bias are higher than those for x-bias. Other ferrite parameters may also play a role in determining the resonant frequency.

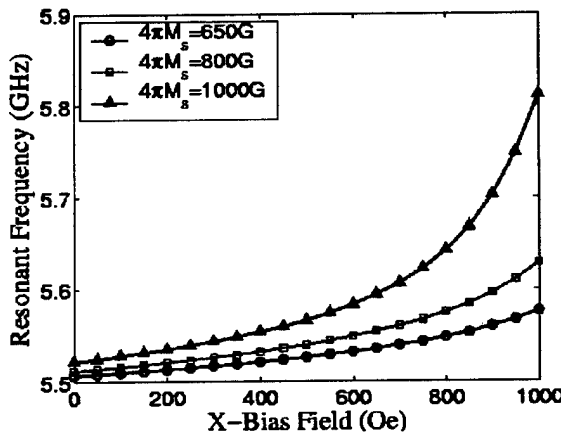


Figure D-14: Resonant frequency for the patch in Figure D-12 as a function of the bias field and saturation magnetization (x-bias).

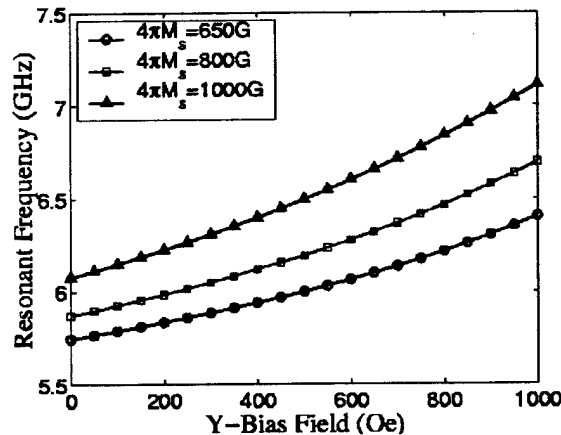


Figure D-15: Resonant frequency for the patch in Figure D-12 as a function of the bias field and saturation magnetization (y-bias).

D.3.2.2 Beam Steering

The most traditional approach for beam steering is to use delay lines/phase shifters, which has the disadvantage of being complex and expensive. Low-profile ferrite antennas can achieve beam steering with less elements and more degrees of freedoms. For ferrite antennas, beam scanning can be simply achieved by gradually changing the applied magnetic field. A convenient way to achieve pattern control is to put the antenna patch sandwiched between an upper ferrite superstrate layer and a lower dielectric substrate layer [8] (see Figure D-16). Without bias, the main beam of the H-plane pattern is normal to the antenna patch. When a bias field is applied, the main beam is shifted depending on the values of the bias field, the ferrite properties and the layer thickness. However, the primary interest is the a priori prediction of the bias field needed to achieve a given beam direction. This is an optimization problem where the objective function is the beam directing by adjusting a set of design variables.

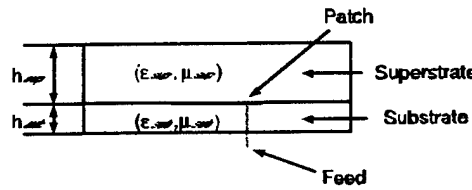


Figure D-16: Geometry of the cavity-backed patch antenna for the beam steering problem.

Let us first consider three design variables: the thickness of the ferrite superstrate h_{sup} , biasing field H_0 , and saturation magnetization $4\pi M_s$. The optimization model can be stated as follows:

$$\text{Find } h_{sup}, H_0, \text{ and } 4\pi M_s \text{ that minimize } |\theta_* - \theta_0| \quad (37)$$

where $\theta_* = \arg \max_{\theta} \text{(Relative Power)}$.

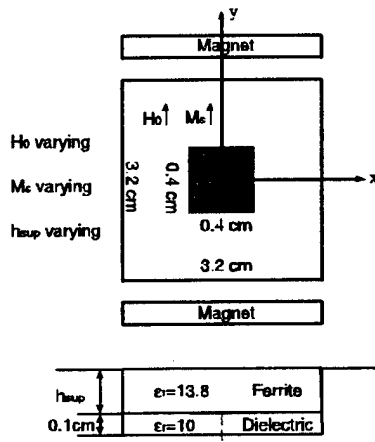


Figure D-17: Geometry of a single patch under a ferrite cover layer (superstrate).

The antenna configuration is shown in Figure D-17. We set the desired beam shift angles to be 10, 20 and 30 degrees, respectively, and the optimizer runs once for each angle. The results are shown in Figure D-18.

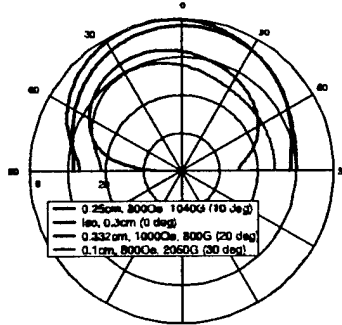


Figure D-18: Scanning of single patch at 6.180GHz: Y-bias, $\phi = 0$ cut, 3 variables.

The above optimization was not practical since the thickness was also allowed to vary. Thus, we instead considered the possibility of adjusting only the externally applied magnetic field H_0 to achieve scanning. In this design, all other variables are fixed except the magnetic field H_0 . The geometry is the same as in Figure D-17 except $h_{sup} = 0.2$ cm and $4\pi M_s = 1300$ G in current problem. Figure D-19 shows the results of H_0 to get desired beam angles. As seen, the resulting pattern has the prescribed beam direction of $\theta_0 = 10, 20$ and 30 degrees corresponding to $H_0 = 800, 2000$ and 2050 Oe. These values of H_0 were predicted by the optimizer after just a few iterations. On the average, 30-60 FEM calls are needed for each value due to the computation of objective function and gradients during the optimization process.

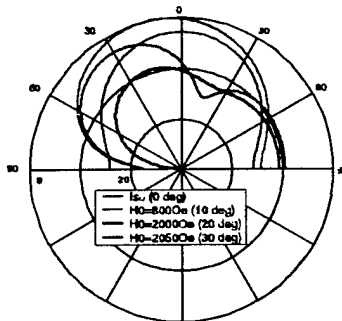


Figure D-19: Scanning of single patch at 6.9GHz: Y-bias, $\phi = 0$ cut. Only H_0 is varied, with $h_{sup}=0.2$ cm, and $4\pi M_s=1300$ G

Using the tools developed, we have shown the ability to apply optimization methods to synthesize antenna patterns as well as beam steering for ferrite arrays. This is a very promising area of future research.

D.4 Task 4: Integration of FE Engines with Graphical User Interface (GUI)

Contractor shall develop a graphical user interface (GUI) for each of the codes developed during this effort. The capability to run on multiple platforms shall be provided. Pre- and post-processing modules shall be provided. Pre-processing modules shall provide the geometry input required for the codes, the ferrite specification, the frequency, and the antenna output parameters requested. The GUI shall allow the user to select which code and optimization technique will be used for the calculation. Post-processing modules shall provide formatted data of the requested information and provide the means to graphically display computed antenna parameters.

Status:

- Includes FERRITE Brick code
- Includes TetraPrism FE-BI code
- Preprocessing module
- Provides graphical view of the antenna mounted on the substrate
- GeoView enables viewing of the generated mesh
- User input of antenna operating parameters

- Postprocessing routines enable viewing of calculated data
- User Manual complete (Appendix)

D.4.1 Graphical User Interface (GUI)

The GUI is designed to run LM_BRICK or TetraPrism in a user-friendly interactive fashion versus the typical command line mode. The operation and installation are detailed in the User's Manual provided as an Appendix. We will discuss the basic structure and available windows for running these codes.

The basis for our GUI is the Tool Command Language (TCL) and its widget toolkit TK. These were chosen to satisfy the requirement for a rapid development schedule and robust execution. The scripting nature of TCL and its adoption on many computing platforms make it very competitive against the traditional Graphical User Interface (GUI) development methods using unwieldy low level programming constructs such as C language and vast Application Programming Interface (API) libraries.

TCL/TK is a string-based command language that has few fundamental constructs and relatively little syntax. The commands are interpreted from ASCII files and require no compilation. TCL is the original set of commands designed for gluing together compiled application codes into a cohesive solution. The TK extension brought GUI commands into the TCL set, and provides fast development times, higher-level interfaces, and more isolation of the user interface from the application itself. TCL/TK 8.0 was used as the virtual machine for design and testing of the Ferrite GUI scripts. It provides an on-the-fly compiler for faster executing scripts, more efficient dynamic memory allocation, and new platform independent font mechanisms, native menus, and more native widgets for UNIX Xwindows, MS-Windows, and Macintosh. In addition, the Effective TCL extension is used to augment the widget set to include Folders and better radio box controls. TCL/TK 8.0 can handle rudimentary 2D graphics rendering needed for a complete integrated solution for displaying finite element grids and the line plots for postprocessing impedance, patterns, and RCS. If needed, 3D enriched graphics can be written in C using OpenGL and Motif Widgets for customized high performance rendering windows launched from TCL/TK scripts.

The main window of the GUI consists of a collection of folders that differentiate the categories of input to the codes (either LM_BRICK or TetraPrism). There is no menu bar with typical file, edit, and view options. Configuration of the GUI is done by selecting a folder, changing the state of a widget such as a check button or radiobox, and going on to the next folder. When the configuration is complete, the user can generate his run script to pass to the code. All information present in the GUI at that moment will be written to the run script. There are two types of run scripts to pass to the FEM code: the Preprocessor script for making a geometry file and the FEM run script for performing the calculations. The execution of the FEM code is done via piping and redirection operations.

As mentioned previously, there are separate GUI programs for LM_BRICK and TetraPrism due to the differing I/O requirements. The instructions for operating each GUI are included as an Appendix. The following discussion walks through the various folder screens that run as part of TetraPrism. The first Folder we access is the Cavity Folder. It is shown in Figure D-20.

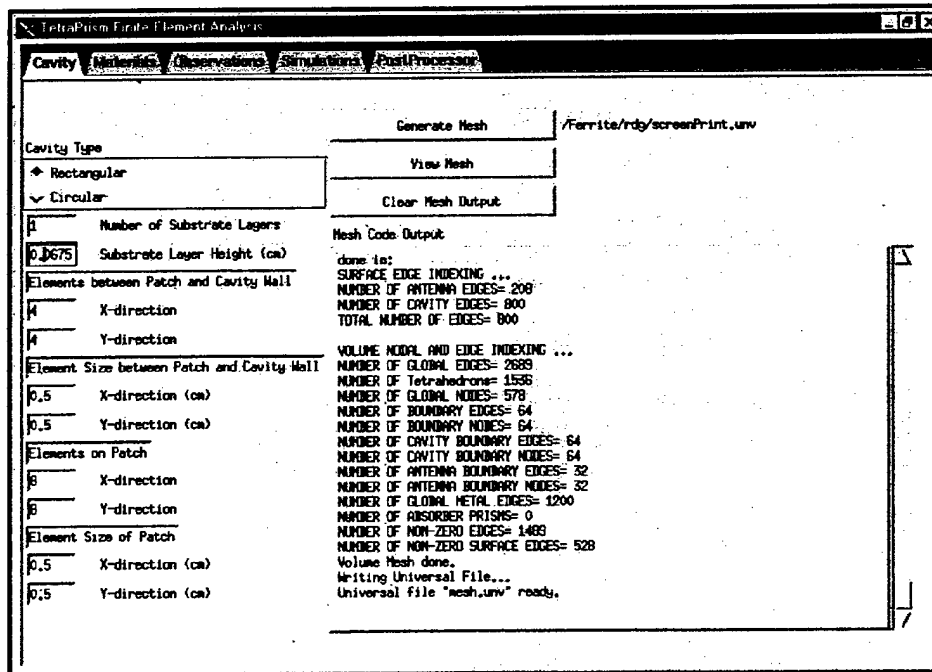


Figure D-20: GUI Cavity Folder screen. *Basic parameters for cavity and patch geometry are entered*

Once patch and cavity are created, we can use GeoView to view the geometry and the mesh. A patch geometry example is shown in Figure D-21.

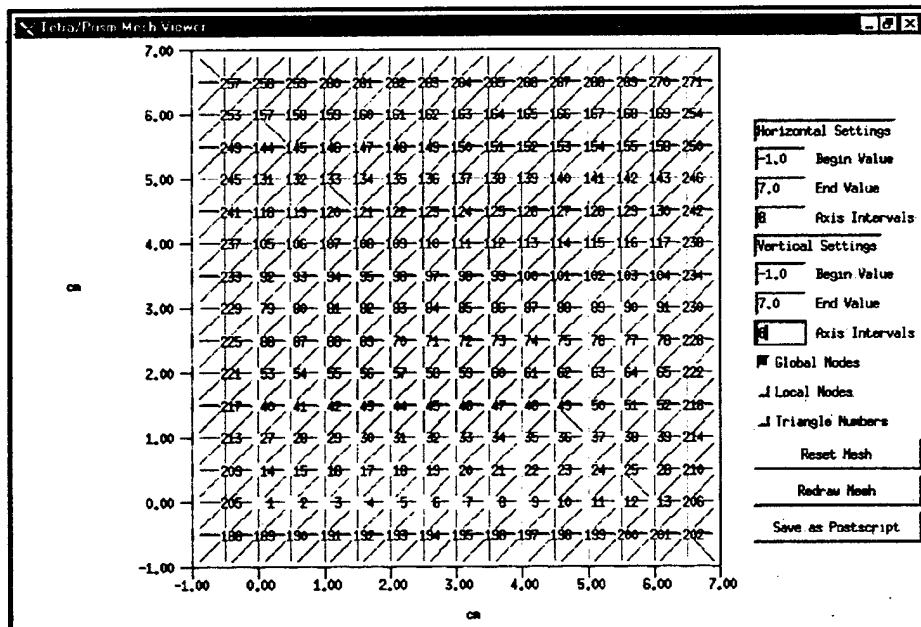


Figure D-21: GeoView output for a patch example. Displays the patch and the node numbers. Node numbers are needed to determine the feed locations. Red indicates the patch location.

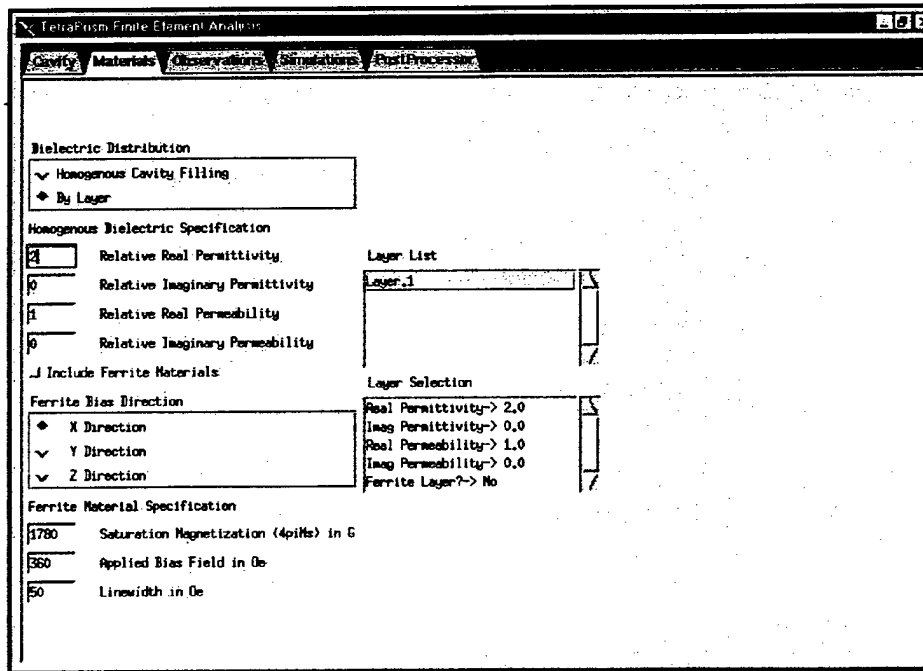


Figure D-22: GUI Material Folder screen. Sets up the material and ferrite properties.

Once the cavity properties are input, we set up the material parameters for the various areas with in the problem. The Material Folder screen is shown in Figure D-22. The next step is to decide on the desired observation parameters. These are input from the Observation Folder shown in Figure D-23.

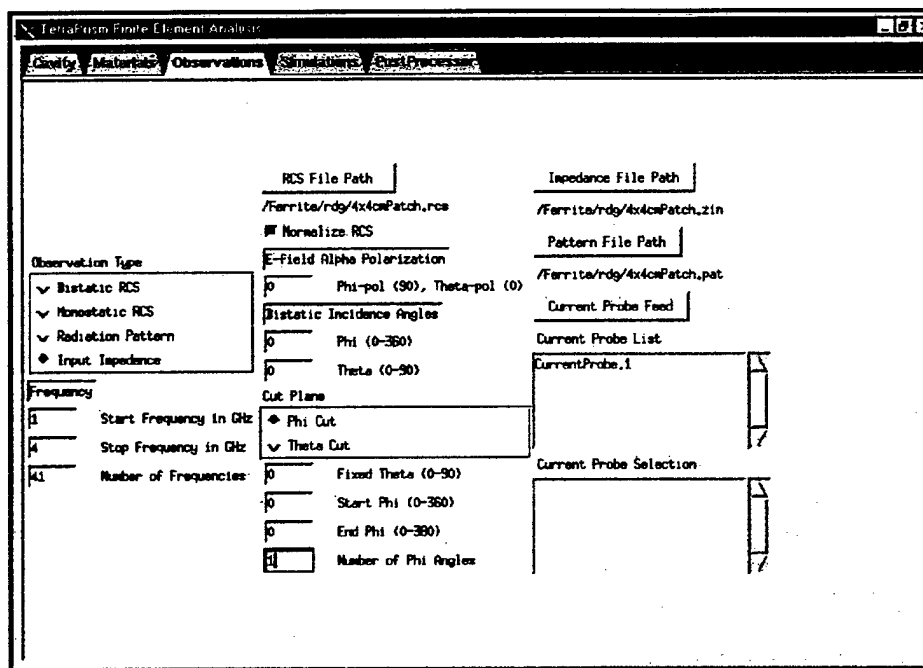


Figure D-23: GUI Observation Folder screen. Where observation parameters are entered.

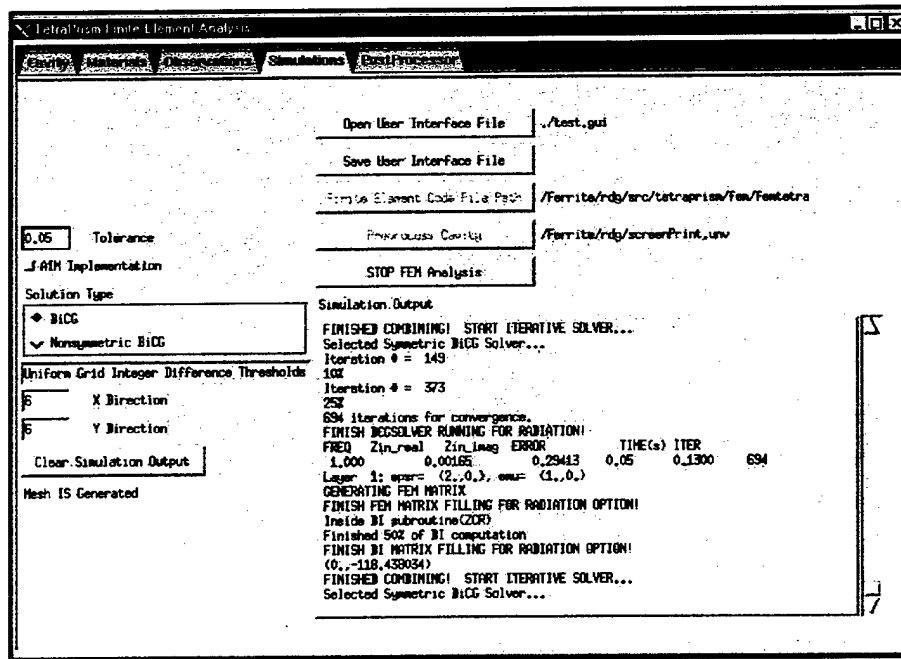


Figure D-24: GUI Simulation Folder screen. Where the desired simulation parameters are set. In this case, the FEM analysis is being accomplished.

Note, the FEM analysis status shows in the window on the lower right-hand side of the folder. The FEM analysis is done once the preprocessing is done. The output of the FEM analysis can be viewed in the GUI Postprocessing Folder screen shown in Figure D-25.

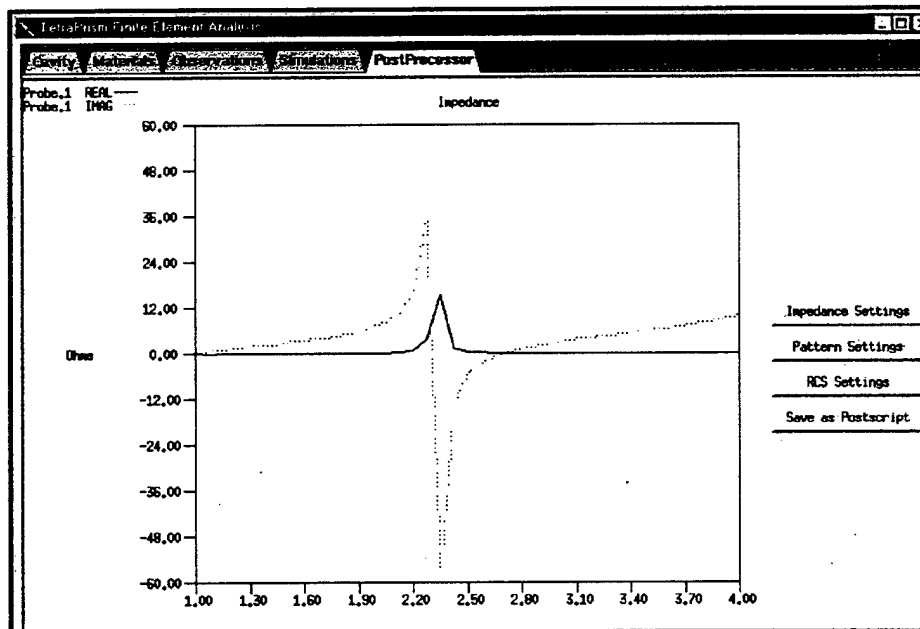


Figure D-25: GUI Postprocessing Folder screen. A patch impedance plot is shown.

The focus of the GUI development has been placed on Linux. It should easily translate to other UNIX platforms that have TCL/TK and a f77 fortran compiler. The GUI User's Manual contains test examples to be run with the codes.

E. Published Papers

- 1 H. How, C. Vittoria, M. H. Champion, L. C. Kempel, and K. D. Trott, "X-Band Phased Array Antennas using Crystal YIG Phase Shifters," *J. Appl. Phys.*, submitted, 1999.
- 2 J.L. Volakis, T. F. Eibert and K. Sertel, "Fast Integral Methods for Conformal Antenna and Array Modeling in Conjunction with Hybrid Finite Element Formulations," accepted in *Radio Sci.*
- 3 L.S. Andersen and J.L. Volakis, "Adaptive analysis of antennas using hierarchical mixed order vector finite elements for tetrahedra," submitted to *IEEE Trans. Antenna Propagat.*, 1999
- 4 H. How, W. Hu, L.C. Kempel, K. D. Trott, and C. Vittoria, "Phase Shifters at X-Band Using Single-Crystal YIG Films C Theory and Experiments," *IEEE Trans. Microwave Theory Tech.*, submitted, 1999.
- 5 D. Filipovic, L.S. Andersen and J.L. Volakis, "A multi-resolution method for simulating infinite periodic arrays," Submitted to *IEEE Trans. Antenna Propagat.*, 1999
- 6 Z. Li and J.L. Volakis, "Design of ferrite antennas using the sequential programming method,' to be submitted to *IEEE Trans. Antenna Propagat.*, 1999
- 7 H. How, W. Hu, C. Vittoria, L. C. Kempel, and K. D. Trott, "Single-Crystal YIG Phase Shifter at X-Band," *J. Appl. Phys.*, submitted, 1999.
- 8 H. How, C. Vittoria, M.H. Champion, L.C. Kempel, and K.D. Trott, "Steerable Phased Array Antennas Using Single-Crystal YIG Phase Shifters C Theory and Experiments," *IEEE Trans. Microwave Theory and Tech.*, submitted, 1999.
- 9 L.S. Andersen and J.L. Volakis, "Accurate and efficient simulation of antennas using hierarchical mixed-order tangential vector finite elements for tetrahedra," *IEEE Trans. Antenna Propagat.*, Vol. 47, to appear August 1999.
- 10 L.S. Andersen and J.L. Volakis, "Condition number of various FEM matrices," *J. Electromagnetic Waves Appl.*, Vol. 13, pp. 1661-1677, Dec. 1999
- 11 A.D. Brown, J.L. Volakis, L.C. Kempel, Y. Botros, "Ferrite Antennas on Ferromagnetic Substrates," *IEEE Trans. Antennas and Propagat.*, Vol. 47, pp. 26-32, Jan. 1999
- 12 Y. Botros and J. L. Volakis, "Preconditioned Generalized Minimal Residual Iterative Scheme for Perfectly Matched Layer Terminated Applications," *IEEE Microwave and Guided Wave Lett.*, Vol. 9, pp. 45-47, Feb 1999.

- 13 L.S. Andersen and J.L. Volakis, "Development and application of a novel class of hierarchical tangential vector finite elements for electromagnetics" *IEEE Trans. Antennas and Propagat.*, Vol. 47, No. 1, pp. 104-108, Jan. 1999
- 14 Y.E. Erdemli, C.J. Reddy and J.L. Volakis, "AWE Technique in Frequency Domain Electromagnetics," *J. Electromagnetic Waves Appl.*, Vol. 13, pp. 359-378, 1999
- 15 H. How, L.C. Kempel, K. D. Trott, C. Vittoria, "Green's Function Calculation on Circular Microstrip Patch Antennas," *IEEE Trans. Microwave Theory Tech.*, submitted, 1998.
- 16 L.S. Andersen and J.L. Volakis, "Hierarchical Tangential Vector Finite Elements for Tetrahedra," *IEEE Microwave and Guided Wave Letters*, vol. 8, No.3, pp. 127-129, March 1998
- 17 Z. Li, P. Papalambros, J.L. Volakis, "Designing broadband patch antennas using the sequential quadratic programming method," *IEEE Trans. Antennas and Propagat.*, pp. 1689-1692, Nov. 1997

Conference Papers

1. K. Trott, "Focused Application Software for the Design of Ferrite Patch Antennas", 1999 AFOSR Electromagnetics workshop, San Antonio, TX
2. A. Brown, L. Kempel, K. Trott, H. How and J. L. Volakis, "Compact, integrated coplanar phase shifter/antenna array", 1999 IEEE Antennas and Propagat Symposium, Orlando, FL.
3. Z. Li, J.L. Volakis and P. Papalambros, "Optimization of patch antennas on ferrite substrate using the finite element methods," 1999 IEEE Antennas and Propagat Symposium, Orlando, FL.
4. L.S. Andersen and J.L. Volakis, "Accurate and efficient simulation of antennas using hierarchical mixed order tangential vector finite elements for tetrahedra," 1999 IEEE Antennas and Propagat Symposium, Orlando, FL
5. L.S. Andersen and J.L. Volakis, "Condition number for various FEM matrices," 1999 IEEE Antennas and Propagat Symposium, Orlando, FL
6. J.L. Volakis, T. Eibert, K. Sertel, L. Andersen and D. Filipovic, "Fast hybrid finite element algorithms for conformal antenna analysis," 1999 IEEE Antennas and Propagat Symposium, Orlando, FL
7. L. Volakis, L.S. Andersen, T.F. Eibert, K. Sertel and Z. Li, "Fast Hybrid Finite Element Methods and Their Applications for Conformal Antennas," 1999 Applied Computational Electromagnetics Society (ACES) Conference, Monterey, CA, Digest pp. 250-258.

8. Y. Erdemli, A.D. Brown and J.L. Volakis, "Frequency and Angular Extrapolation in Hybrid Finite Element-Boundary Integral Systems," 1999 Applied Computational Electromagnetics Society (ACES) Conference, Monterey, CA, Digest pp. 302-307.
9. Y. Erdemli and J.L. Volakis, "AWE Technique in Frequency Domain," SC98, Reno, Nevada
10. L.C. Kempel and K.D. Trott, "Progress in Modeling Complex Conformal Antennas using the Finite Element-Boundary Integral Method", 1998 IEEE AP-S International Symposium and National Radio Science Meeting
11. A. Brown, J. Volakis, L. Kempel and Z. Li, "Numerical Analysis of the Radiation Properties of Ferrite Patch Antennas," *Proc. of the 1998 IEEE Antennas and Propagation Society International Symposium*, Atlanta, Georgia, vol. 1, pp. 244-247, July 1998.
12. L. Andersen and J. Volakis, "Hierarchical Tangential Vector Finite Elements for Tetrahedra," *Proc. of the 1998 IEEE Antennas and Propagation Society International Symposium*, Atlanta, Georgia, vol. 1, pp. 240-244, July 1998.
13. Y. Botros and J. Volakis, "Convergence Improvements of Iterative Solvers for Poorly Conditioned Antenna Applications," 1998 URSI Meeting, Atlanta, GA, p. 203
14. Ozdemir, Nuremberger, and Volakis, "A Thin Cavity-Backed Archimedian Slot Spiral for 800-3000 MHz Band Coverage", 1998 IEEE AP-S International Symposium and National Radio Science Meeting (leveraged effort)
15. J. L. Volakis, K. Sertel, and T. F. Eibert, "Hybrid Finite Element Modeling of Conformal Antenna and Array Structures Utilizing Fast Integral Methods", 4th International Workshop on Finite Elements for Microwave Engineering, From Electromagnetics to Microwave Electronics Software, Poitiers, Futuroscope, France, 1998.
16. Z. Li, P. Papalambros, J.L. Volakis, "Antenna Optimization Using Sequential Quadratic Programming(SQP) Algorithms, IEEE Antennas and Propagation Society International Symposium, Montreal, Canada, July 13-18 1997, Digest-vol.1, pp:514-517
17. Arik Brown, Jian Gong, Leo Kempel, John L.Volakis, "Patch Antennas on Ferromagnetic Substrates", IEEE Antennas and Propagation Society International Symposium, Montreal, Canada, July 13-18 1997, Digest-vol.2 pp:606-609
18. Lars S.Andersen, John L. Volakis, "A Novel Class of Hierarchical Higher Order Tangential Vector Finite Elements for Electromagnetics" IEEE Antennas and Propagation Society International Symposium, Montreal, Canada, July 13-18 1997, Digest-vol.2, pp:648-651
19. John L.Volakis, "Hybrid Finite Element Methods for Conformal Antenna Simulations", IEEE Antennas and Propagation Society International Symposium, Montreal, Canada, July 13-18 1997, Digest-vol.2,pp:1318-1321

F. Researchers and Students Supported

F.1 Mission Research Corporation (MRC)

- Keith D. Trott, Ph.D. Principal Investigator
- Rene D. Guidry Mesh generation design
- Christopher G. Repesh Graphical User Interface design

F.2 University of Michigan

- John L. Volakis, Ph.D. Professor
- Arik D. Brown (also supported by minority Fellowship for 2 semesters during the past 2.5 years)
Dissertation title: 'Characterization of ferrite patch antennas', to be completed Feb 2000.
- Lars Andersen (also supported by Danish fellowship for 1 year out the 2.5 years of the project)
Dissertation title: 'Multiresolution methods for simulation and design of antennas', to be published October 1999
- Zhifang Li Dissertation title: 'Gradient optimization methods for antenna design'. half completed.

F.3 ElectroMagnetic Applications, Inc, (EMA)

- Hoton H. How, Ph.D. Principal Investigator
- Carmine Vittoria, Ph.D. Senior Researcher

G. Inventions

There were no inventions as a result of this project.

H. Conclusions and Suggestions for Future Work

H.1 Conclusions

During Phase II of this SBIR effort, MRC, EMA, and UM demonstrated the feasibility of using modern FE analysis to characterize the behavior of ferrite materials and the benefits of using ferrite materials to achieve modified radiation characteristics from ferrite loaded antennas. However, there is still much work to be done.

H.2 Suggestions for Future Work

The MRC Team suggests the following finite element analysis and frequency agile material research and development be performed:

- Continue to investigate ferrite antenna uses through a combination of modeling, prototype fabrication, and measurement
- Further investigate the use of ferrites for shutterable radome applications
- Continue to investigate novel ferrite-based feed networks that will offer advantages in terms of size, weight, and reduced complexity as compared to current phased array feed networks
- Further refine and validate FEM modeling tools capable of modeling ferrites, ferroelectrics, dielectrics, and perfect electric conductors.

I. References

- [1] D.M. Pozar, Microwave Engineering, New York, Addison-Wesley, 1990.
- [2] L.C. Kempel, J.L. Volakis, and R.J. Sliva, "Radiation by cavity-backed antennas on a circular cylinder," *IEE Proceedings, Pt. H*, 1995.
- [3] H. How, T.M. Fang, W. Liu, and C. Vittoria, "Antenna array of circular patches on ferrite substrate," INTERMAG 96 Conference, April 1995, San Antonio, TX.
- [4] C. Vittoria, Elements of Microwave Networks, World Scientific Publishing Co., Singapore, 1998
- [5] H. How, W. Hu, L.C. Kempel, K. D. Trott, and C. Vittoria, "Phase Shifters at X-Band Using Single-Crystal YIG Films: Theory and Experiments," *IEEE Trans. Microwave Theory Tech.*, submitted, 1999.
- [6] H. How, C. Vittoria, M.H. Champion, L.C. Kempel, and K.D. Trott, "Steerable Phased Array Antennas Using Single-Crystal YIG Phase Shifters: Theory and Experiments," *IEEE Trans. Microwave Theory and Tech.*, submitted, 1999
- [7] D.M. Pozar, "Radiation and scattering characteristics of microstrip antennas on normally biased ferrite substrates," *IEEE Trans. Antennas Propagat.*, vol. 40, no. 9, pp. 1084-1092, Sept. 1992.
- [8] A. Henderson, J.R. James, and A. Fray, "Magnetized microstrip antenna with pattern control," *Electronics Letters*, vol. 24, no. 1, pp. 45-47, Jan. 1988.
- [9] Arik D. Brown, John Volakis, Leo C. Kempel, and Zhifang Li, "Numerical analysis of the radiation properties of ferrite patch antennas," *Proc. of the 1998 IEEE Antennas and Propagation Society International Symposium*, Atlanta, Georgia, vol. 1, pp. 244-247, July 1998.
- [10] Zhifang Li, Panos Y. Papalambros, and John L. Volakis, "Designing broadband patch antennas using the sequential quadratic programming method," *IEEE Transactions on Antennas and Propagation*, v.45, n.11, pp. 1689-1692, November 1997.
- [11] A.C. Polycarpou, et.al., "Radiation and scattering from ferrite-tuned cavity-backed slot antennas: theory and experiment," *IEEE Trans. Antennas Propagat.*, vol. 46, no. 9, pp. 1297-1306, Sept. 1998.
- [12] L.S. Andersen and J.L. Volakis, "Hierarchical tangential vector finite elements for tetrahedra," *IEEE Microwave and Guided Wave Letters*, vol. 8, pp. 127-129, March 1998.

Appendix A: User's Manual for the MRC Graphical User Interface

A. Focused Application Software for Ferrite Patch Antennas

LINUX Graphical User Interfaces

Table of Contents

Background
Installation
Example Data
Running FERRITE LM_BRICK
Running FERRITE TETRA AIM
Running GEO Mesh Viewer

This documentation and the TCL/TK scripts are maintained by Christopher Repesh at Mission Research Corporation and he can be reached via his email address repesh@fwb.gulf.net

Background on FERRITE LINUX Graphical User Interfaces

In the Fall of 1998, work began on a platform independent graphical user interface solution for a set of finite element codes developed under contract (SBIR II) Focused Application Software for Design of Ferrite Patch Antennas. Tool Command Language (TCL) and its widget toolkit TK were chosen to satisfy the requirement for a rapid development schedule and robust execution. The scripting nature of TCL and its adoption on many computing platforms make it very competitive against the traditional Graphical User Interface (GUI) development methods using unwieldy low level programming constructs such as C language and vast Application Programming Interface (API) libraries.

TCL/TK is a string-based command language that has few fundamental constructs and relatively little syntax. The commands are interpreted from ASCII files and require no compilation. TCL is the original set of commands designed for gluing together compiled application codes into a cohesive solution. The TK extension brought GUI commands into the TCL set, and provides fast development times, higher-level interfaces, and more isolation of the user interface from the application itself. TCL/TK 8.0 was used as the virtual machine for design and testing of the Ferrite GUI scripts. It provides an on-the-fly compiler for faster executing scripts, more efficient dynamic memory allocation, and new platform independent font mechanisms, native menus, and more native widgets for UNIX XWindows, MS-Windows, and Macintosh. In addition, the Effective TCL extension is used to augment the widget set to include Folders and better radio box controls. TCL/TK 8.0 can handle rudimentary 2D graphics rendering needed for a complete integrated solution for displaying finite element grids and the line plots for postprocessing impedance, patterns, and RCS. If needed, 3D enriched graphics can be written in C using OpenGL and Motif Widgets for customized high performance rendering windows launched from TCL/TK scripts.

After preliminary testing on both UNIX (via Linux) and MS-Windows, it was discovered that the MS-Windows GUI had severe limitations. Although the GUI appearance was fine, the operating system support lacked in several key areas:

- 1) No inherent scripting shell for installation of software (such as BASH)
- 2) Performance failures with executing compiled code via pipes and redirection.
- 3) No process ID methods for tracking jobs (such as pid)
- 4) No FORTRAN compiler included in base installation (such as g77)
- 5) No Postscript Level 2 support for graphics files

Focus has been placed on LINUX GUI development, and these efforts should easily translate to other UNIX platforms that have TCL/TK virtual machines and f77 compilers.

[Back to Table of Contents](#)

Installation of FERRITE LINUX Graphical User Interfaces

LINUX Installation

Recent versions of LINUX have the TCL/TK 8.0 interpreter installed in the default configuration. If this is not available, you can go to Scriptics Corporation (<http://www.scriptics.com>) to download the latest virtual machine in compiled form or source code.

You will need to know which wish interpreter you are using for TCL/TK. This will be asked for during the installation script execution. You can use the UNIX command which wish to find this executable. Once you have this accomplished, locate the distribution tar file ferritez.tar and lets begin.

1. Log in as Root.
2. Choose a 13 or less character pathname for untarring the distribution.
--- Due to a limitation in one of the source modules, this character limit is necessary for now. Each user that will run the code should have their own source to work with since they will compile their own solutions. For example,
--- /Ferrite/cgr/ is 13 characters long and would represent the user Christopher
--- Gary Repesh's ferrite code directory. Similarly add other personal initial
--- directories for other users.
3. In each directory created, untar ferritez.tar using tar -xzvf ferritez.tar
--- IMPORTANT! Use lower case z for gunzip, not Z for uncompress!!
--- Gunzip has a more efficient compression algorithm
4. Choose a directory and run the install_gui script
--- IMPORTANT! Root must have current path visibility, i.e. ./
5. Type in the name of the wish interpreter
6. Install the Effective TCL/TK toolkit if not already installed
7. Repeat for the other user directories
--- DO NOT install Effective Toolkit since it already was installed!
8. For each user, transfer ownership of the files for each personal directory
--- For /Ferrite/cgr/ you would type chown -R chrisr /Ferrite/cgr
if Chris's username is chrisr
9. Log out as Root. Each user can now run the codes in his/her directory
--- if they have current path visibility ./ (add entry to PATH variable)
--- PATH="\$PATH:./" defined in their shell script. They may also need their
--- DISPLAY variable set. This can be accomplished with BASH by adding the
--- following lines to their .bash_profile script
--- DISPLAY=:0.0
--- export DISPLAY

[Back to Table of Contents](#)

Data Runs for LM_BRICK, TETRA AIM

LM_BRICK Graphical User Interface

Data Runs for isotropic and ferrite substrates for a small rectangular patch. Monostatic RCS over an elevation cut in addition to probe impedance over a large bandwidth.

Look in data/bricks/isotropic and data/bricks/ferrite.

TETRA AIM code

Data Runs for isotropic and ferrite substrates for a small rectangular patch. Monostatic RCS over an elevation cut in addition to probe impedance over a large bandwidth.

Look in data/prisms/isotropic and data/prisms/ferrite.

The geometry, materials, and observation settings for LM_BRICK and TETRA AIM are identical for code comparison.

GEOVIEW

Look in data/geoview for the sinuous spiral mesh.

[Back to the Table of Contents](#)

Running LM_BRICK Graphical User Interface

Introduction

The user executes the GUI by running bricks in his installation directory. Before actually running the LM_BRICK code, the user will have to compile it as described in the following directions.

The main window of the GUI consists of a collection of folders that differentiate the categories of input to LM_BRICK. There is no menu bar with typical file, edit, and view options. All configuration to the GUI is done by selecting a folder, changing the state of a widget such as a check button or radiobox, and going on to the next folder. When configuration is complete, the user can generate his run script to pass to the LM_BRICK code. All information present in the GUI at that moment will be written to the run script. There are two types of run scripts to pass to the LM_BRICK code: the Preprocessor script for making a geometry file and the FEM run script for performing the calculation. The execution of the LM_BRICK code is done via piping and redirection operations.

There are 6 particular file types used by the GUI to generate and process the information specified in it. These fall into the following categories:

1. RCS (*.rcs)
2. Interior Fields (*.fld)
3. Pattern (*.pat)
4. Impedance (*.zin)
5. GUI state (*.gui)
6. LM_BRICK processed geometry (*.geo)

It is convenient to use the same name, e.g. patch12, for a particular problem specification and let the file extensions differentiate between the types of data stored. Thus there would be a patch12.zin, a patch12.gui, etc. The GUI file contains all the state variables of the GUI for reloading a configuration at a later time.

Folder Descriptions

Cavity
Materials
Observations
Simulations
Postprocess

[Back to the Table of Contents](#)

LM_BRICK Cavity Folder and its Specification

Array Settings

Specifies the XY dimensions of the cavity, where those dimensions are centered, and how they are discretized by grid cells (grid nodes - 1).

Plane Settings

Determines the view depiction of the cavity by defining the axis range, how that range is discretized in intervals, and what cut plane is visible.

Nodes

Specifies the XY surface node types of the cavity aperture. If Patch is not specified, then the patch information is ignored when the run script is generated.

Substrate

Specifies the substrate depth in layer size and number of layers. When value is entered and confirmed, hit the cancel to exit the dialog. This allows immediate graph update when specifying a side view of the cavity.

Metal Block, Patch

Enters the various metal boundary conditions in the cavity in terms of absolute grid coordinates. A conversion mechanism is available for translating these to centimeters. The listbox displays the current metal block/patch entries, and these may be edited or deleted by double clicking on the particular entity in

the listbox. The entity displayed in the grid may also be double clicked to invoke editing on that entity.

[Back to the Table of Contents](#)

LM_BRICK Materials Folder and its Specification

Dielectric Distribution

The dielectrics can be specified as one of three types: Homogenous, By Layer, or Homogenous covered walls. Both homogenous types use the homogenous edit fields for specifying permittivity and permeability. When By Layer is selected, the layer list must be edited to change ϵ , and μ , for each layer. Simply clicking on a layer entity in the list box will display that layer info in the Layer selection listbox. Double clicking on a layer entity will allow editing the layer information.

Ferrite Distribution

Ferrites are only included if the Check box is enabled to include ferrites. A ferrite material is entered by pressing the Add Ferrite button. This ferrite material has an associated ID that is seen in the ferrite listbox. Simply clicking a ferrite material will display the parameters for that material in the Ferrite Selection box. Double clicking a ferrite material allows editing and deleting the ferrite material. Ferrites can be homogenously distributed in the cavity or specified by layer. In both cases, the ferrite ID is used to specify particular ferrite materials.

[Back to the Table of Contents](#)

LM_BRICK Observations Folder and its Specification

Observation Type

Backscatter, Bistatic, or Radiation is selected via the radio box control. All angle and frequency sweeps apply to each observation type. The individual settings are specified in the middle column of widgets. Current probes for radiation analysis are added using the current probe button. The listboxes work just as they do in the Materials folder for manipulating the current probe parameters.

Observation Files

All pathnames for data generated from the LM_BRICK code are specified by clicking the appropriate button and choosing a pathname using a file browser. The selected path is displayed on the folder beneath the button.

[Back to the Table of Contents](#)

LM_BRICK Simulations Folder and its Specification

Convergence and Solution

The convergence criteria, solution type, and whether to monitor convergence are chosen.

Compilation

The LM_BRICK include parameters must be correctly set for the given problem size and the code recompiled. When the codes are first installed, there are no compiled codes to execute, so this step must be completed before any geometries are created or calculations performed.

GUI and LM_BRICK Files

The state of the GUI can be saved or read using the appropriate buttons. The location of the LM_BRICK code can be specified for using the GUI to initiate the LM_BRICK runs. Create Geometry will ask for a name to store the binary results of the LM_BRICK preprocessor, and will automatically initiate the preprocessor. Perform FEM Analysis will launch LM_BRICK in FE-BI mode. The feedback from the both the preprocessor and the FE-BI runs will be displayed in the Simulations Output text widget as they execute. The GUI generates run scripts (*.pre for running the preprocessor and *.fem for running the FE-BI) that can be redirected to the LM_BRICK executable from the command line.

[Back to the Table of Contents](#)

LM_BRICK Postprocessor Folder and its Specification

Impedance

The impedance data file is selected using a file browser. Once loaded, it remains in memory until another impedance file is read in. Both Resistance and Reactance are displayed on the same Cartesian plot. Frequency and Ohm regions of interest can be examined by selecting the limits of the plot view. The scale tick marks can also be set.

Pattern

The pattern data file is selected using a file browser. Once loaded, it remains in memory until another pattern file is read in. Both Theta-directed and Phi-directed gain can be selected for viewing on a Cartesian plot. The domain axis can be selected as either Frequency, Phi, or Theta and regions of interest can be examined by selecting the limits of the plot view. The scale tick marks can also be set.

Radar Cross Section

The RCS data file is selected using a file browser. Once loaded, it remains in memory until another RCS file is read in. Both Theta-directed and Phi-directed RCS can be selected for viewing on a Cartesian plot. The domain axis can be

selected as either Frequency, Phi, or Theta and regions of interest can be examined by selecting the limits of the plot view. The scale tick marks can also be set

[Back to the Table of Contents](#)

Running TETRA AIM Graphical User Interface

Introduction

The user executes the GUI by running `prisms` in his installation directory.

The main window of the GUI consists of a collection of folders that differentiate the categories of input to `prisms`. There is no menu bar with typical file, edit, and view options. All configuration to the GUI is done by selecting a folder, changing the state of a widget such as a check button or radiobox, and going on to the next folder. When configuration is complete, the user can generate his run script to pass to the TETRA AIM code. All information present in the GUI at that moment will be written to the run script. There are two types of run scripts to pass to the TETRA AIM code: the Preprocessor script for making a geometry file and the FEM run script for performing the calculation. The execution of the TETRA AIM code is done via piping and redirection operations.

Folder Descriptions

Cavity
Materials
Observations
Simulations
Postprocess

[Back to the Table of Contents](#)

TETRA AIM Cavity Folder and its Specification

Cavity Settings

The type of cavity (Rectangular or Circular) is selected and its associated dimensions are entered into the edit fields. These edit fields control the spacing between the cavity walls and the patch, the number of elements on the patch, and discretization size. The substrate layer depth and number of substrate Layers are also entered. Once this data is decided, the Generate Mesh button will commit the values to memory and proceed with compiling/running the mesh generation code.

Mesh Controls

The Generate Mesh button will ask for file path to place 4 files: `*.unv` (Universal file), `*.attr` (attributes), `*.meshds` (MeshDs), and `*.setup` (Setup).

Only one name is required, and is used for all four file types. Depending on cavity type, a mesh code is compiled and executed, the status of which is displayed in the mesh output widget. Once this is over, the Mesh Controls will come back on. The View Mesh button will ask for a Universal file (implicitly asking for the other three files) and spawn a view window for manipulating the 2D mesh depiction. Horizontal and Vertical controls enable viewing regions of interest. Global nodes, triangle numbers, and local nodes may be overlayed. Reset Mesh will resize the window to include the entire mesh. Redraw Mesh will update any edited settings for viewing.

It IS IMPORTANT that the status in the mesh output reflect that a mesh.unv file has been generated, otherwise the settings chosen have been processed into a failed mesh. This may happen for a number of reasons. Try Generate Mesh a few times on the same settings and if this still does not result in the "mesh.unv generated" mesh, then they should be changed.

[Back to the Table of Contents](#)

TETRA AIM Materials Folder and its Specification

Dielectric Distribution

The dielectrics can be specified as one of two types: Homogenous or By Layer. When By Layer is selected, the layer list must be edited to change ϵ , and μ , for each layer. Simply clicking on a layer entity in the list box will display that layer info in the Layer selection listbox. Double clicking on a layer entity will allow editing the layer information.

Ferrite Distribution

Ferrites are only included if the Check box is enabled to include ferrites. Only a single ferrite material is entered. This ferrite material can be homogeneously distributed in the cavity or specified by layer. The individual layer setting must be set for YES or NO depending on whether this layer is to be designated a Ferrite layer.

[Back to the Table of Contents](#)

TETRA AIM Observations Folder and its Specification

Observation Type

Bistatic RCS, Monostatic RCS, Radiation Pattern, or Impedance is selected via the radio box control. All angle and frequency sweeps apply to each observation type. The individual settings are specified in the middle column of widgets. Current probes for radiation analysis are added using the current probe button. The listboxes work just as they do in the Materials folder for manipulating the current probe parameters.

Observation Files

All pathnames for data generated from the LM_BRICK code are specified by clicking the appropriate button and choosing a pathname using a file browser. The selected path is displayed on the folder beneath the button.

[Back to the Table of Contents](#)

TETRA AIM Simulations Folder and its Specification

Convergence and Solution

The convergence criteria, solution type, and AIM threshold integers are chosen.

GUI Files

The state of the GUI can be saved or read using the appropriate buttons. The location of the FEMTETRA code can be specified for using the GUI to initiate the FEMTETRA runs. The GUI generates run scripts (*.pre for running the preprocessor and *.fem for running the FE-BI) that can be redirected to the FEMTETRA executable from the command line.

Preprocessing and Analysis

The mesh MUST BE Generated in the Cavity folder before preprocessing the mesh and its associated materials. Any dimension changes to the mesh or changes in the isotropic material attributes must be recompiled into the FEMTETRA code via the Preprocess function. Once this is accomplished, then analysis for the particular observation type may commence. This is done using the Perform Analysis function. Changes to Observations do not require a mesh or Preprocess regeneration IF you know this has been done for THIS particular geometry!

[Back to the Table of Contents](#)

TETRA AIM Postprocessor Folder and its Specification

Impedance

The impedance data file is selected using a file browser. Once loaded, it remains in memory until another impedance file is read in. Both Resistance and Reactance are displayed on the same Cartesian plot. Frequency and impedance regions of interest can be examined by selecting the limits of the plot view. The scale tick marks can also be set.

Pattern

The pattern data file is selected using a file browser. Once loaded, it remains in memory until another pattern file is read in. Directed gain can be selected for viewing on a Cartesian plot. The domain axis can be selected as either Frequency, or Angle (Theta or Phi) and regions of interest can be examined by selecting the limits of the plot view. The scale tick marks can also be set.

Radar Cross Section

The RCS data file is selected using a file browser. Once loaded, it remains in memory until another RCS file is read in. RCS can be selected for viewing on a Cartesian plot. The domain axis can be selected as either Frequency, or Angle (Theta or Phi) and regions of interest can be examined by selecting the limits of the plot view. The scale tick marks can also be set

[Back to the Table of Contents](#)

Running GEOVIEW Graphical User Interface

Introduction

The user executes the GUI by running GEOVIEW in his installation directory.

This mesh viewer is designed for a particular finite element mesh file format (NOT LM_BRICK *.geo!). The following is a description

```
1248 2775 2775 1432 1432 0
1 391 869 392
2 584 583 1139
3 1345 580 1360
4 1337 1295 575
5 1317 1337 1338
6 1352 576 1295
7 1139 1338 909
8 395 868 943
9 587 586 400
10 586 585 1151
```

```
.
.
.
1 2.681799 -0.416967 0
2 2.632088 0.177127 0
3 2.484313 0.626380 0
4 2.325516 0.878967 0
5 2.228431 0.917981 0
6 2.213173 0.741617 0
7 2.229809 0.356605 0
8 2.173369 -0.195730 0
9 1.945941 -0.805809 0
10 1.654356 -1.208636 0
```

This example can be found under /src/geoviewer/sin2.geo in the GUI installation directory, and is a sinuous spiral mesh. The view controls are identical to those described for the mesh viewer for TETRA AIM in the Cavity Folder.

[Back to the Table of Contents](#)

Appendix B: User's Manual for FemTetra: A Tetrahedral FE-BI Code

PROJECT INFORMATION

PROJECT TITLE: Focused Application Software for Design of Ferrite Patch Antennas

REPORT TITLE: USERS MANUAL FOR FEMTETRA: A TETRAHEDRAL FINITE ELEMENT-BOUNDARY INTEGRAL (FE-BI) CODE

U-M REPORT No.: 036307-5-T

CONTRACT

START DATE: July 1997
END DATE: June 1999

DATE: July 1999 (version 2)

SPONSOR:

S. McCool and K. Trott	Dr. Arje Nachman
Mission Research Corp.	Air Force Office of Scientific Research
147 John Sims Parkway	AFOSR/NM
Valparaiso, FL. 32580	Bolling AFB, DC 20332-0001
trott@fwb.gulf.net	nachman@afosr.af.mil
Phone: 904-729-4494	
Fax: 904-729-2443	

SPONSOR

CONTRACT No.: SC-0022-97-001
(Air Force Prime Contract no. F49620-97-C-0022)

U-M PRINCIPAL

INVESTIGATOR: John L. Volakis
EECS Dept.
University of Michigan
1301 Beal Ave
Ann Arbor, MI 48109-2122
Phone: (313) 764-0500 FAX: (313) 747-2106
volakis@umich.edu
<http://www-personal.engin.umich.edu/~volakis/>

CONTRIBUTORS

TO THIS REPORT: Arik Brown, Yunus Erdemli and J.L. Volakis

Contents

1	Introduction	5
1.1	Code Description	5
2	Mesher	7
2.1	Running the Automatic Mesher	7
2.1.1	Rectangular Meshes	7
2.1.2	Circular Meshes	9
3	Running <i>femtetra.f</i>	10
3.1	Preprocessor	10
3.1.1	Additional Key Information on Running the Preprocessor	10
3.2	Running <i>femtetra.f</i>	11
3.2.1	Additonal Information for Running <i>femtetra.f</i>	12
4	Demonstration Examples	13
4.1	Rectangular Patch: Z_{in}	13
4.1.1	Mesh Generation	13
4.1.2	Preprocessor	16
4.1.3	Running the Code and Code Output	16
4.2	Circular Patch: Backscattering	22
4.2.1	Mesh Generation	22
4.2.2	Preprocessor	24
4.2.3	Running the Code and Code Output	26
4.3	Rectangular Ferrite Patch: Backscattering	28
4.3.1	Mesh Generation	29
4.3.2	Preprocessor	30
4.3.3	Running the Code and Code Output	30

List of Tables

1	Description of input file in Figure 2.	7
2	Sample preprocessor file.	11
3	Input file <i>inputmeshZin</i>	14
4	Z_{in} preprocessor file	17
5	Z_{in} input file using AWE.	18
6	Z_{in} input file using AIM.	19
7	Output Data for Z_{in} Using AWE	20
8	Output Data for Z_{in} Using AIM	21
9	Input file to <i>meshcirc.f</i>	23
10	Circular patch preprocessor input file.	24
11	Circular patch input file.	25
12	Backscattering output file for circular patch.	27
13	Input file <i>inputmeshyang</i>	29
14	Ferrite patch preprocessor file	30
15	Ferrite patch input file.	31
16	Backscattering output file for ferrite rectangular patch.	33

List of Figures

1	Diagram of the procedure for running <i>femtetra.f</i> in conjunction with the automatic mesher.	6
2	Input file for <i>meshrect.f</i>	7
3	Surface mesh for the sample input file in Figure 2.	8
4	Input file for <i>meshcirc.f</i>	9
5	Surface mesh for the sample input file in Figure 4.	9
6	Rectangular patch geometry.	14
7	Surface mesh for the rectangular patch.	15
8	Plots of Impedance, $Z_{in} = R_{in} + jX_{in}$	21
9	Circular patch geometry.	22
10	Surface mesh for circular patch.	23
11	Plot of $\sigma_{\theta\theta}$	27
12	Rectangular patch geometry.	28
13	Surface mesh for the rectangular patch.	29
14	Plot of $\sigma_{\theta\theta}$	32

1 Introduction

1.1 Code Description

The program *femtetra.f* is written in Fortran77 and has been verified on Hewlett Packard(HP) and Sun workstations. The code has an internal preprocessor that uses a Universal file mesh(.unv) for input. The mesh can be generated using Ideas. The University of Michigan has developed an automatic mesher which can be used in conjunction with *femtetra.f*. The mesher allows the user to bypass generating a mesh manually and facilitates a simple and convenient interface between the mesher and *femtetra.f*.

Femtetra.f is used to analyze printed antennas on dielectric or anisotropic substrates. The code employs a hybrid Finite Element Method - Boundary Integral(FE-BI) approach using an Electric Field Integral Equation(EFIE) formulation. The resulting FE-BI system of equations is solved iteratively using a Bi-Conjugate Gradient(BiCG) solver. The code also has a Quasi Minimal Residual(QMR) solver. In addition, the code also has two additional features. The Adaptive Integral Method(AIM), which is a fast integral method, is used specifically in the BI portion of the formulation for improved speed. Also, the code has been equipped with the Asymptotic Waveform Evaluation(AWE) method for frequency extrapolation. The AWE implementation computes all elements of the BI impedance matrix, so it is limited to the memory capacity of the computer used for running *femtetra.f*.

Figure 1 gives an overview of the steps needed to run *femtetra.f* in conjunction with the automatic mesher. First, *meshrect.f* (rectangular geometries) or *meshcirc.f* (circular geometries) is run, to produce a Universal file. This Universal file is then given as input to *femtetra.f* which processes the file, and produces the necessary tetrahedral information and dimensioning information for the code. The code is then compiled using a **make** file. After compiling is completed, *femtetra.f* is then used to compute either scattering or radiation data.

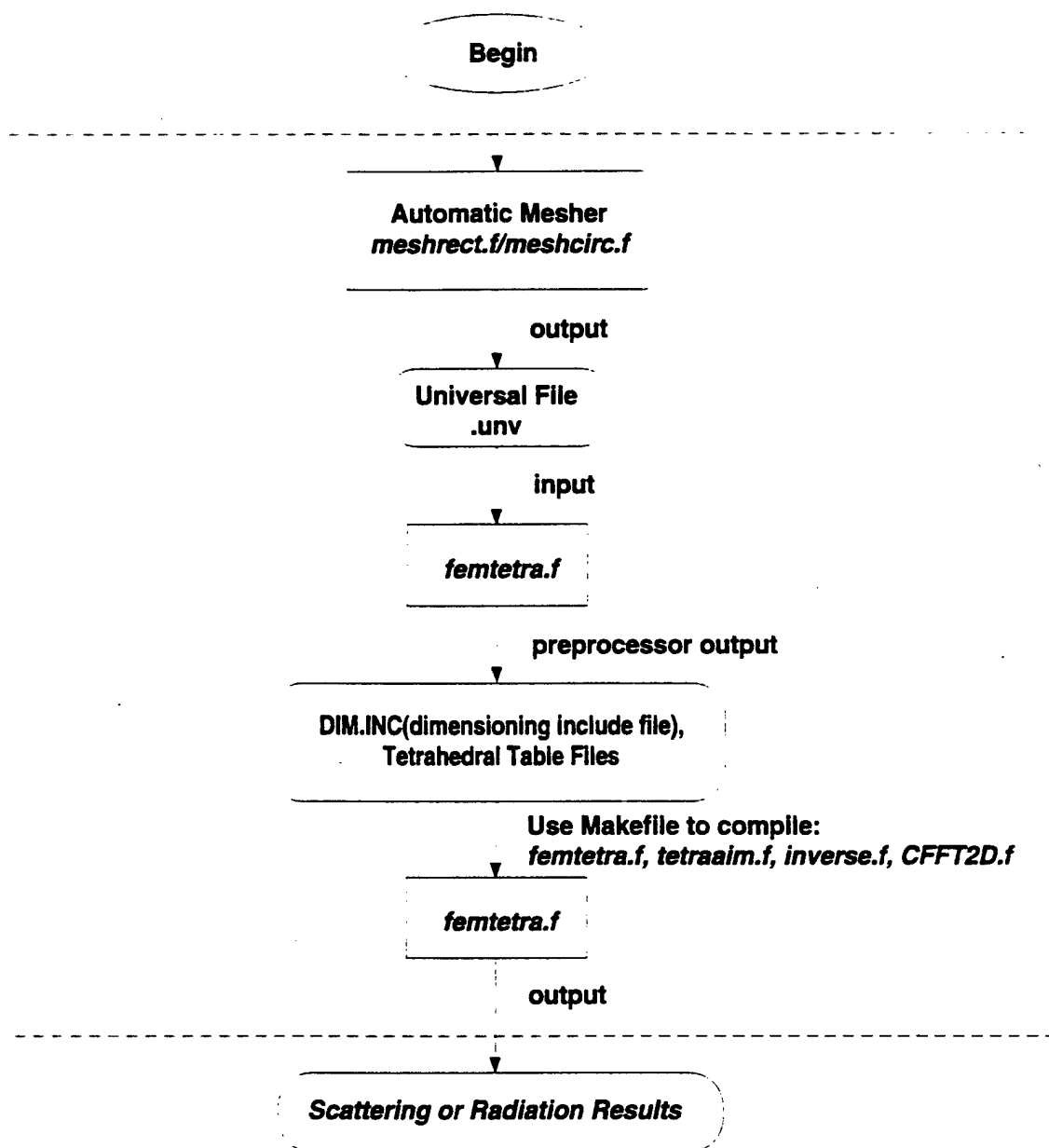


Figure 1: Diagram of the procedure for running `femtetra.f` in conjunction with the automatic mesher.

```

0
1
.4166667 .425
3 2
.4166667 .425
12 8
1
1
.08779

```

Figure 2: Input file for *meshrect.f*.

- 0; line1, Specifies whether surface nodes are all substrate(1=yes, 0=no).
- 1; line2, Specifies whether patch or slot(1=patch, 0=slot).
- .4166667 .425; line3, Specifies the **element size**(cm) in the x and y directions, respectively, between the *antenna* and *cavity wall*.
- 3 2; line4, Specifies the **number of elements** between the *antenna* and *cavity wall* in the x and y directions, respectively.
- .4166667 .425; line5, Specifies the **element size**(cm) in the x and y directions, of the *antenna* only.
- 12 8; line6, Specifies the **number of antenna elements** in the x and y directions, respectively.
- 1; line7, Specifies element type(1=tetras, 0=prisms).
- 1; line8, Specifies the number of substrate layers.
- .08779; line9, Specifies the height of the substrate layer.

Table 1: Description of input file in Figure 2.

2 Mesher

2.1 Running the Automatic Mesher

A Universal file is needed to run *femtetra.f*. The Universal file can be generated using the automatic mesher. Depending on whether the problem geometry is rectangular or circular, *meshrect.f* or *meshcirc.f* is the file needed for mesh generation.

2.1.1 Rectangular Meshes

Figures 2 and 3 show a sample input file for *meshrect.f*, and the corresponding surface mesh. An explanation of each line of the sample file, *inputrect*, is shown in Table 1.

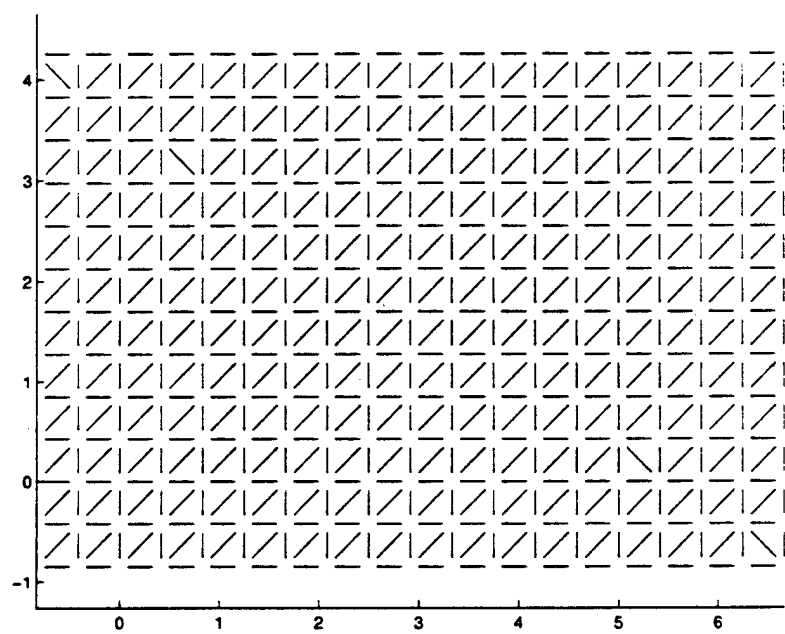


Figure 3: Surface mesh for the sample input file in Figure 2.

0
1
.0825
8
.082
5
1
1
.0508

Figure 4: Input file for *meshcirc.f*.

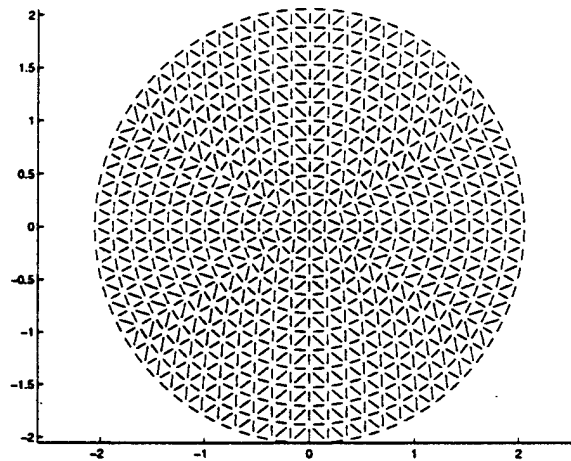


Figure 5: Surface mesh for the sample input file in Figure 4.

2.1.2 Circular Meshes

Figures 4 and 5 show a sample input file for *meshcirc.f*, and the corresponding surface mesh. The description of the file *inputcirc* is similar in structure to *inputrect* and will not be discussed.

3 Running *femtetra.f*

3.1 Preprocessor

Before running *femtetra.f*, it is necessary to process the Universal input file generated by the automatic mesher. When running the code initially, the user will be prompted with 3 menu options:

1. Run Preprocessor
2. Run Tetrahedral FEM-BI Code
3. Exit Code

In order to process the mesh file, the user must choose option '1'. The user will then be prompted with a series of questions about the mesh geometry. Since the preprocessor prompts the user at each entry, the user can easily apply the following example to other mesh geometries(i.e. open cavity, circular patch, circular cavity, etc...) with a clear understanding of how the preprocessor works. Table 2 shows a description of the input needed for the preprocessor. For this sample input file, it is assumed that the cavity is rectangular and that there is one pec patch on the aperture, and one substrate layer.

3.1.1 Additional Key Information on Running the Preprocessor

There are several important things the user should be cognizant of when running the preprocessor in *femtetra.f*. Initially, the user should have a dummy *DIM.INC* file in order to compile the code for the first time. See[1] for the structure of *DIM.INC*. In actuality, the user will be supplied with several demonstration runs which will include *DIM.INC* files that can be used to compile *femtetra.f* for the first time. In addition, if the user is modeling a ferrite material, the user should enter (1.0, 0.0) for the value of μ_r .

meshinput.unv(user supplied)	line1,	Specify input mesh file name.
1	line2,	Specify if there is a patch (1=yes, 0=no).
1	line3,	Specify cavity shape (1=rectangular, 0=circular).
1	line4,	Specify number of pec patches.
$x_{max,patch}$	line4,	Specify maximum x coordinate for the patch.
$x_{min,patch}$	line5,	Specify minimum x coordinate for the patch.
$y_{max,patch}$	line4,	Specify maximum y coordinate for the patch.
$y_{min,patch}$	line5,	Specify minimum y coordinate for the patch.
1	line6,	Specify number of cavity layers.
$(\epsilon_{r,real}, \epsilon_{r,imag}) (\mu_{r,real}, \mu_{r,imag})$	line7,	Specify ϵ_r and μ_r for each layer (in this case there is one substrate layer).

Table 2: Sample preprocessor file.

When running the preprocessor for a rectangular patch geometry, the user will need to first ascertain the maximum/minimum x-y coordinates of the patch, using either Ideas or the mesh viewer in Matlab, which is supplied with the automatic mesher. This is because the automatic mesher does not center the patch at the coordinates (0.0,0.0), thus the values for $x_{max,patch}$, $x_{min,patch}$, $y_{max,patch}$, and $y_{min,patch}$ can not be predetermined. This is not necessary for circular patches because the automatic mesher centers the patch at the coordinates (0.0,0.0)

3.2 Running *femtetra.f*

There are 3 files separate from *femtetra.f* which are needed in order to run the code. The files are:

- *tetraaim.f*
- *inverse.f*
- *FFT2D.f*

These files are included with the code. In order to compile *femtetra.f* and it's corresponding files, a *make* file is also included with the code. The name of this file is *Makefile*¹.

¹When compiling the code on a Sun workstation, the options +E1 and +U77 should be omitted.

After compiling *femtetra.f*, the user will then be able to run the code. When running the code, the user will once again be prompted with 3 menu options:

1. Run Preprocessor
2. Run Tetrahedral FEM-BI Code
3. Exit Code

The user should choose option '2' to generate the particular scattering or radiation information needed. Similar to the automatic mesher, and the preprocessor, when running *femtetra.f* the user will be prompted for the information needed for each line of input. In the next section, several demonstration examples are shown giving the user a chance to become familiar with the code.

3.2.1 Additonal Information for Running *femtetra.f*

Running *femtetra.f* is straightforward, although an additional comment will be made regarding geometries that include a probe-fed patch. When running *femtetra.f* for a problem with a probe feed, the user will be prompted to specify the global node numbers for the corresponding probe edges within the FEM volume. The global node numbers can be found in two ways. The first approach is to view the mesh file in Ideas before running the code, and locate the node numbers for the probe feed edges. The second and easier approach is to view the surface mesh using Matlab via the automatic mesher. See[1] for more information on using the mesh viewing option in the automatic mesher package. The mesh viewer displays the global node numbers for the surface mesh on the bottom of the cavity. To obtain the global node number for the node directly above the corresponding node in the surface mesh, simply add the number of aperture nodes to the corresponding node number. For example, if the bottom of the probe has the global node number 10, and there are 250 aperture nodes, then the node directly above node 10 would be global node number 260. In this manner the global node numbers for the probe edge(s) can be found easily.

4 Demonstration Examples

This section contains three different demonstration examples for *femtetra.f*. The examples will consist of the following:

- Single layer rectangular cavity with a rectangular patch, input impedance(Z_{in}).
- Single layer circular cavity with a circular patch, backscatter.
- Single layer rectangular ferrite cavity with a rectangular patch, backscatter.

Each individual example will include the following items:

- Input file for the automatic mesher.
- Surface mesh figure.
- Input file for the preprocessor in *femtetra.f*.
- Input file for running *femtetra.f*.
- Output data.

These examples allow the user to become familiar with the procedure for running *femtetra.f*.

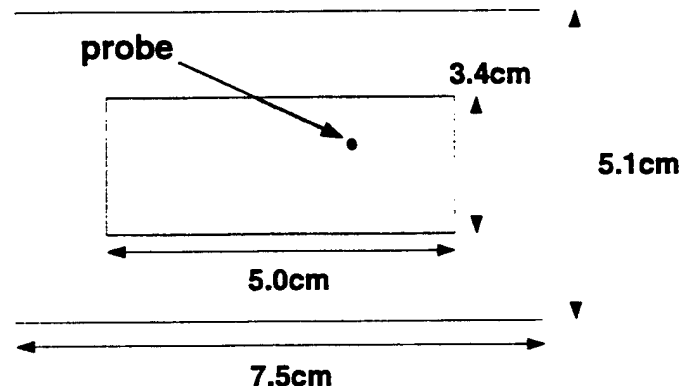
4.1 Rectangular Patch: Z_{in}

The rectangular patch shown in Figure 6 can be found in [2]. It consists of a rectangular patch residing in a cavity, with a single probe feed. The patch size is 5.0 cm x 3.4 cm and the cavity size is 7.5 cm x 5.1 cm. The substrate has a thickness of 0.08779 cm, $\epsilon_r = 2.17$, and a loss tangent of 0.0015. The probe is located at the coordinates ($x_p = 1.22$ cm, $y_p = 0.85$ cm).

4.1.1 Mesh Generation

In order to generate the Z_{in} for this geometry, the mesh must be generated. To accomplish this using the automatic mesher, the appropriate file to use is *meshrect.f*. The corresponding input file *inputmeshZin* is shown on page 14 with a description for each line of input. The surface mesh generated by the automatic mesher is shown in Figure 7.

Top View



Side View



Figure 6: Rectangular patch geometry.

0	Specifies that the surface substrate nodes are not all dielectric.
1	Specifies a patch geometry.
.4166667 .425	Size(cm) of the elements(x,y) between the patch and cavity wall.
3 2	Number of elements in the x-y direction between the patch and cavity wall.
.4166667 .425	Size(cm) of the elements(x,y) on the patch.
12 8	Number of elements in the x-y direction on the patch.
1	Specifies tetra elements.
1	Specifies one substrate layer.
.08779	Specifies the substrate height.

Table 3: Input file *inputmeshZin*.

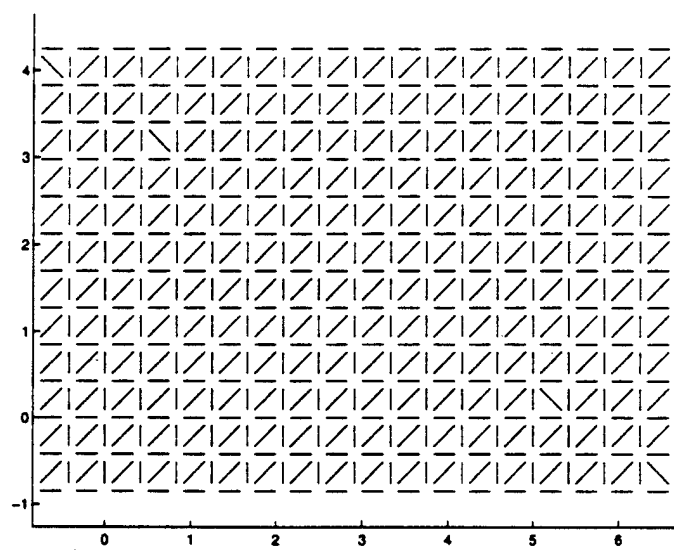


Figure 7: Surface mesh for the rectangular patch.

4.1.2 Preprocessor

Once the mesh has been created, it must then be processed by *femtetra.f*. The input file is shown on page 17 with a description for each line of input. Once the mesh has been processed, *femtetra.f* will automatically exit from the code. The user must then recompile *femtetra.f* using the *Makefile*. The preprocessor automatically creates the include file *DIM.INC* which contains the proper dimensioning. Thus the user does not have to change or adjust the dimensioning for the code at all.

4.1.3 Running the Code and Code Output

After the mesh has been processed and *femtetra.f* has been recompiled, the code is then ready to run. For this particular geometry, example files will be given for when AWE is used to compute the electric field solution, and the case when AIM is used to compute the electric field solution. Tables 5 and 6 show the input files for the rectangular patch for the AWE and AIM cases, with a description for each line of input. The output files for Z_{in} , for both cases, are shown in Tables 7 and 8. A plot of these files comparing the AIM and AWE results is shown in Figure 8. For Table 7, the first column is frequency(GHz), the second column is the input resistance R_{in} and the third column is the input reactance X_{in} . The first column in Table 8 is frequency(GHz), the second column is the input resistance R_{in} , the third column is the input reactance X_{in} , the fourth column is the residual error of the iterative solver, the fifth column is the time it takes to solve for the unknown electric fields, and the sixth column is the number of iterations needed for convergence.

1	Preprocessor menu option.
Zin.unv	Name of Universal file(mesh).
1	Specifies type of geometry.
1	Specifies a patch geometry.
1	Shape of cavity(1=rectangular).
1	Specifies number of patches.
5.41667	Maximum x value for patch. ²
0.4166667	Minimum x value for patch. ²
3.4	Maximum y value for patch. ²
0.0	Minimum y value for patch. ²
1	Specifies number of material layers.
(2.17,-0.003255) (1.,0.)	$(\epsilon_{r_{real}}, \epsilon_{r_{imag}}), (\mu_{r_{real}}, \mu_{r_{imag}})$.
400	AIM parameter specifying the maximum number of near field edge contributions for each BI edge.

Table 4: Z_{in} preprocessor file

²See Section 3.1.1.

2	Option to run the code.
1	Chooses computation type(1=AWE).
2	Specifies Z_{in} option
1.86	Specifies frequency expansion point
2	Specifies AWE order ³ .
1.8, 1.92, 61	Specifies frequency range: f_{start}, f_{stop} , number of frequency points.
Zinawe	Output file name.
0	Option to output electric field solution values(0=NO).
1	Number of current probes.
101	Global node #1 for current probe edge ⁴ .
348	Global node #2 for current probe edge ⁴ .
1	Check to see if input data is correct to this point(1=yes).
0.	Specifies phase for probe feed(Assume unit amplitude).
0	Specifies whether there are any ferrite layers(0=no).

Table 5: Z_{in} input file using AWE.

³See [3].

⁴See Section 3.2.1.

2	Option to run the code.
2	Chooses computation type(2=Normal FE-BI without AWE).
3	Specifies output data desired(3=Radiation).
1.8, 1.92, 7	Specifies frequency range: f_{start}, f_{stop} , number of frequency points.
2	Specifies radiation pattern, Z_{in} , or gain(2= Z_{in}).
Zin	Output file name.
0	Option to output electric field solution values(0=NO).
1	Number of current probes.
101	Global node #1 for current probe edge ⁵ .
348	Global node #2 for current probe edge ⁵ .
0	Specifies desired solver(0=Symmetric BiCG).
.01	Specifies tolerance.
1	Option to implement AIM(1=yes) ⁶ .
6,6	x-y integer threshold values for determining Z_{far}^{BI} and Z_{near}^{BI} .
21,42	Size of FFT grid(NXFFT) and FFT pad(NXFFTP); NXFFTP=2*NXFFT ⁷ .
1	Check to see if input data is correct to this point(1=yes).
0.	Specifies phase for probe feed(Assume unit amplitude).
0	Specifies whether there are any anisotropic layers(0=no).

Table 6: Z_{in} input file using AIM.

⁵See Section 3.2.1.

⁶See [4].

⁷After compiling, the user must look at the file *DIM.INC* in order to ascertain the value needed for input for NXFFTP. This value should be set to the value of *MAXFFTP* in *DIM.INC*.

Freq.(GHz)	R_{in}	Z_{in}	Freq.(GHz)	R_{in}	Z_{in}
1.800	2.56399	30.20102	1.862	174.04729	-99.63131
1.802	2.74554	31.06803	1.864	127.71570	-112.65808
1.804	2.94744	31.99648	1.866	92.78013	-109.96984
1.806	3.17289	32.99343	1.868	68.57820	-101.62691
1.808	3.42559	34.06636	1.870	51.99449	-92.13519
1.810	3.71009	35.22423	1.872	40.45283	-83.14964
1.812	4.03191	36.47742	1.874	32.22305	-75.15205
1.814	4.39771	37.83765	1.876	26.20168	-68.18757
1.816	4.81592	39.31943	1.878	21.69057	-62.16239
1.818	5.29673	40.93876	1.880	18.23612	-56.94492
1.820	5.85317	42.71538	1.882	15.53940	-52.40949
1.822	6.50168	44.67241	1.884	13.39750	-48.44540
1.824	7.26355	46.83810	1.886	11.67003	-44.96008
1.826	8.16621	49.24578	1.888	10.25799	-41.87802
1.828	9.24572	51.93568	1.890	9.08967	-39.13671
1.830	10.55072	54.95789	1.892	8.11249	-36.68521
1.832	12.14690	58.37277	1.894	7.28720	-34.48167
1.834	14.12541	62.25479	1.896	6.58400	-32.49142
1.836	16.61421	66.69392	1.898	5.98011	-30.68596
1.838	19.79808	71.79960	1.900	5.45776	-29.04147
1.840	23.94932	77.69994	1.902	5.00293	-27.53775
1.842	29.47790	84.53284	1.904	4.60448	-26.15785
1.844	37.01604	92.41735	1.906	4.25347	-24.88736
1.846	47.55867	101.36970	1.908	3.94266	-23.71391
1.848	62.67717	111.07082	1.910	3.66617	-22.62712
1.850	84.77413	120.26931	1.912	3.41912	-21.61786
1.852	117.01228	125.35600	1.914	3.19743	-20.67805
1.854	161.27016	117.73901	1.916	2.99778	-19.80102
1.856	210.34818	83.08347	1.918	2.81733	-18.98069
1.858	238.07552	15.75378	1.920	2.65368	-18.21176
1.860	220.59427	-56.54645			

Table 7: Output Data for Z_{in} Using AWE

Freq.(GHz)	R_{in}	Z_{in}	Res.	Time(s)	Iter.
1.800	2.45073	29.70736	.01	46.7300	570
1.820	5.70914	42.31318	.01	44.2200	796
1.840	23.54168	77.15297	.01	47.7100	761
1.842	28.98178	83.93197	.01	47.9500	655
1.844	36.33971	91.75127	.01	45.4600	585
1.846	46.57998	100.69490	.01	44.4100	1189
1.848	61.41567	110.38691	.01	53.7300	809
1.850	82.96812	119.73951	.01	47.7900	569
1.852	114.37048	125.35004	.01	44.0600	883
1.854	157.64174	119.35302	.01	48.9300	1191
1.856	207.34557	86.38136	.01	53.6200	1191
1.858	237.56779	20.86102	.01	53.6100	622
1.860	222.99960	-52.48045	.01	47.1000	901
1.880	18.38583	-57.17688	.01	49.2700	738
1.900	5.44361	-28.88870	.01	46.8100	796
1.920	2.58959	-17.84591	.01	47.6300	682

Table 8: Output Data for Z_{in} Using AIM

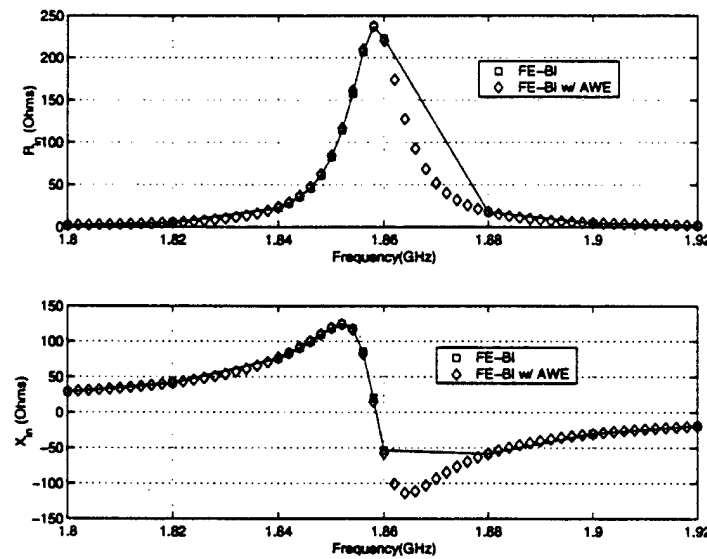


Figure 8: Plots of Impedance, $Z_{in} = R_{in} + jX_{in}$.

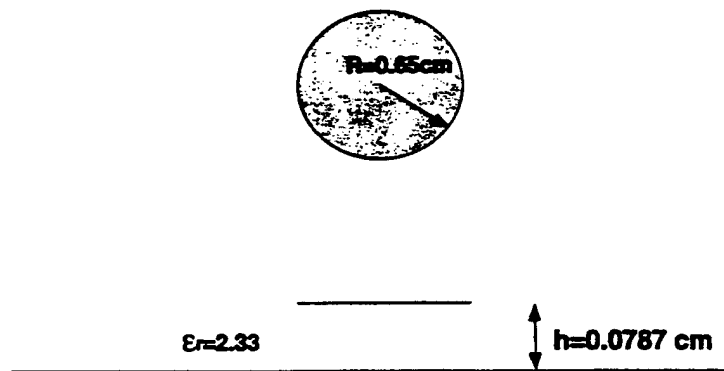


Figure 9: Circular patch geometry.

4.2 Circular Patch: Backscattering

The circular patch shown in Figure 9, can be found in [5]. It consists of a circular patch on an infinite dielectric substrate. The patch is modeled in a finite sized cavity, that is large enough to simulate the infinite substrate. The patch radius is 0.65cm, the substrate height is 0.0787cm, the distance from the cavity to the patch is 1.405cm, and the substrate has an $\epsilon_r = 2.33$.

4.2.1 Mesh Generation

In order to calculate the backscattering for this geometry, the mesh must be generated. To accomplish this using the automatic mesher, the appropriate file to use is *meshcirc.f*. The corresponding input file *inputmeshcircpatch* is shown on page 23 with a description for each line of input. The surface mesh generated by the automatic mesher is shown in Figure 10.

0	Specifies that the surface substrate nodes are not all dielectric.
1	Specifies a patch geometry.
.175625	Size(cm) of the radial elements between the patch and cavity wall.
8	Number of elements in the radial direction between the patch and cavity wall.
.1625	Size(cm) of the radial elements on the patch.
4	Number of elements in the x-y direction on the patch.
1	Specifies tetra elements.
1	Specifies one substrate layer.
.0787	Specifies the substrate height.

Table 9: Input file to *meshcirc.f*.

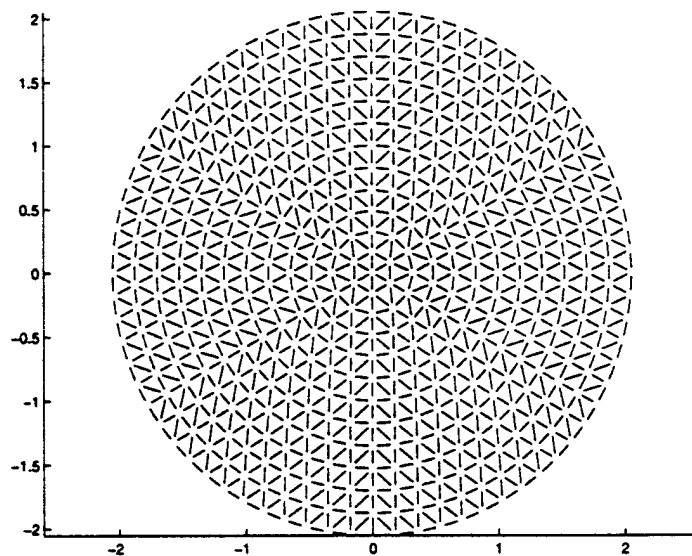


Figure 10: Surface mesh for circular patch.

1	Preprocessor menu option.
circpatch.unv	Name of Universal file(mesh).
1	Specifies a patch geometry.
1	Specifies type of geometry.
1	Specifies a patch geometry.
0	Shape of cavity(0=circular).
2.055	Radius of the <i>entire</i> cavity.
1	Specifies number of patches.
0.0	x coordinate for the center of the patch.
0.0	y coordinate for the center of the patch.
0.65	Radius of the circular patch.
1	Specifies number of material layers.
(2.33,0.0) (1.,0.)	$(\epsilon_{r,real}, \epsilon_{r,imag}), (\mu_{r,real}, \mu_{r,imag})$.
400	AIM parameter specifying the maximum number of near field edge contributions for each BI edge.

Table 10: Circular patch preprocessor input file.

4.2.2 Preprocessor

Once the mesh has been created, it must then be processed by *femtetra.f*. The input file is shown in Table 10. Once the mesh has been processed, *femtetra.f* will automatically exit from the code. The user must then recompile *femtetra.f*. The preprocessor automatically creates the include file *DIM.INC* which contains the proper dimensioning. Thus, the user does not have to change or adjust the dimensioning for the code at all.

2	Option to run the code.
2	Chooses computation type(2=Normal FE-BI without AWE).
2	Specifies output data desired(2=Backscatter).
7., 9., 9	Specifies frequency range: f_{start}, f_{stop} , number of frequency points.
rcscirc	Output file name.
0	Option to output electric field solution values(0=NO).
0	Option to normalize the Radar Cross Section(RCS).
0	Choose E field polarization angle, α (degrees) (0= $\theta - pol$).
2	Specifies cut(2= θ).
180.	Fixed start observation angle ϕ (degrees).
180.	Fixed start observation angle ϕ (degrees).
60.	Start observation angle θ (degrees).
60.	Start observation angle θ (degrees).
1	Number of observation points.
1	Number of <i>fixed</i> observation points.
0	Specifies desired solver(0=Symmetric BiCG).
.03	Specifies tolerance.
1	Option to implement AIM(1=yes) ⁸ .
6,6	x-y integer threshold values for determining Z_{far}^{BI} and Z_{near}^{BI} .
36,72	Size of FFT grid(NXFFT) and FFT pad(NXFFTP); NXFFTP=2*NXFFT ⁹ .
1	Check to see if input data is correct to this point(1=yes).
0	Specifies whether there are any anisotropic layers(0=no).

Table 11: Circular patch input file.

⁸See [4].

⁹After compiling, the user must look at the file *DIM.INC* in order to ascertain the value needed for input for NXFFTP. This value should be set to the value of MAXFFTP in *DIM.INC*.

4.2.3 Running the Code and Code Output

After the mesh has been processed and *femtetra.f* has been recompiled, the code is then ready to run. On page 25 is the input file for the circular patch, and a description for each line of input. The ouput file *rcscirc* is shown in Table 12. A plot of the file is shown in Figure 11. The first column in Table 12 is the backscatter angle θ (degrees), the second column is the backscatter angle ϕ (degrees), the third column is the frequency(GHz), the fourth column is σ (dBsm), the fifth column is $\sigma_{\theta\phi}$ (dBsm), the sixth column is $\sigma_{\theta\theta}$ (dBsm), the seventh column is the residual error, the eighth column is the time(sec.) it takes to solve for the unknown electric fields, and the ninth column is the number of iterations needed for convergence.

ϕ	θ	Freq(GHz)	σ	$\sigma_{\theta\phi}$	$\sigma_{\theta\theta}$	Res.	Time(s)	Iter.
180.000	60.000	7.000	-49.514	-80.000	-49.514	.0210	1060.87	156
180.000	60.000	7.250	-38.948	-80.000	-38.948	.0279	1122.71	225
180.000	60.000	7.500	-26.992	-98.964	-26.992	.0263	1081.23	179
180.000	60.000	7.750	-31.237	-103.721	-31.237	.0255	1071.01	166
180.000	60.000	8.000	-35.036	-107.449	-35.036	.0246	1109.24	210
180.000	60.000	8.250	-37.151	-108.184	-37.151	.0278	1074.67	171
180.000	60.000	8.500	-38.670	-108.764	-38.670	.0284	1047.25	141
180.000	60.000	8.750	-40.019	-108.835	-40.019	.0290	1046.36	140
180.000	60.000	9.000	-41.366	-108.713	-41.366	.0267	1046.63	140

Table 12: Backscattering output file for circular patch.

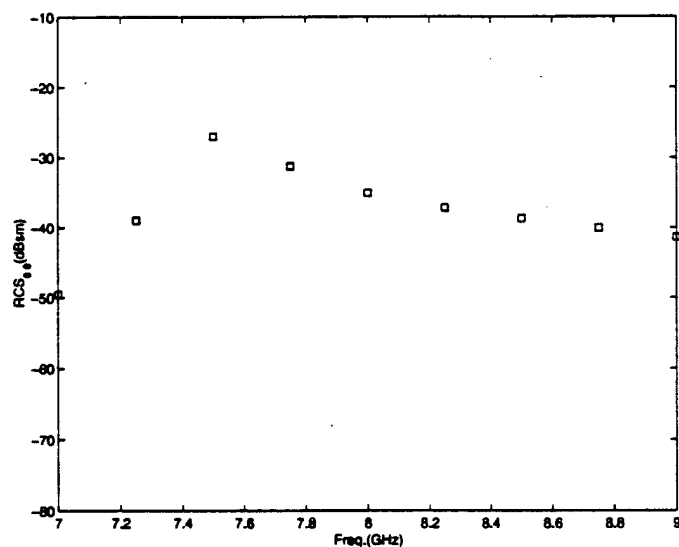
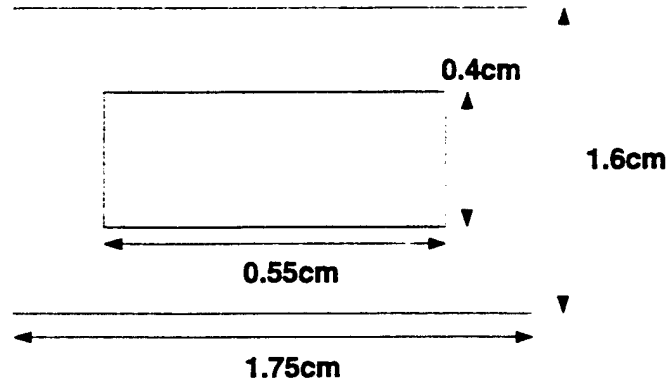


Figure 11: Plot of $\sigma_{\theta\theta}$.

Top View



Side View

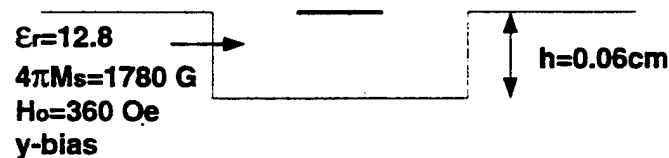


Figure 12: Rectangular patch geometry.

4.3 Rectangular Ferrite Patch: Backscattering

The rectangular patch shown in Figure 12 can be found in [6]. It consists of a rectangular patch residing on an infinite y-biased ferrite substrate. In order to model this a finite cavity was used. The patch size is 0.55 cm x 0.4 cm and the cavity size is 1.75 cm x 1.6 cm. The substrate has a thickness of 0.06 cm, $\epsilon_r = 12.8$, saturation magnetization($4\pi M_s$) = 1780 G and a y-bias magnetic field(H_o) = 360 Oe.

0	Specifies that the surface substrate nodes are not all dielectric.
1	Specifies a patch geometry.
.06 .06	Size(cm) of the elements(x,y) between the patch and cavity wall.
10 10	Number of elements in the x-y direction between the patch and cavity wall.
.06875 .06667	Size(cm) of the elements(x,y) on the patch.
8 6	Number of elements in the x-y direction on the patch.
1	Specifies tetra elements.
1	Specifies one substrate layer.
.06	Specifies the substrate height.

Table 13: Input file *inputmeshyang*.

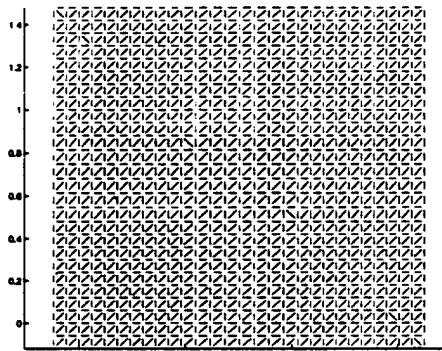


Figure 13: Surface mesh for the rectangular patch.

4.3.1 Mesh Generation

In order to generate the backscattering data for this geometry, the mesh must be generated. To accomplish this using the automatic mesher, the appropriate file to use is *meshrect.f*. The corresponding input file *inputmeshyang* is shown in Table 13 with a description for each line of input. The surface mesh generated by the automatic mesher is shown in Figure 13.

1	Preprocessor menu option.
yang.unv	Name of Universal file(mesh).
1	Specifies a patch geometry.
1	Shape of cavity(1=rectangular).
1	Specifies number of patches.
1.03	Maximum x value for patch ¹⁰ .
0.48	Minimum x value for patch. ¹⁰
0.88002	Maximum y value for patch. ¹⁰
0.48	Minimum y value for patch. ¹⁰
1	Specifies number of material layers.
(12.8,0.) (1.,0.)	$(\epsilon_{r,real}, \epsilon_{r,imag}), (\mu_{r,real}, \mu_{r,imag})$.
600	AIM parameter specifying the maximum number of near field edge contributions for each BI edge.

Table 14: Ferrite patch preprocessor file

4.3.2 Preprocessor

Once the mesh has been created, it must then be processed by *femtetra.f*. The input file is shown on page 30 with a description for each line of input. Once the mesh has been processed, *femtetra.f* will automatically exit from the code. The user must then recompile *femtetra.f* with the proper dimensioning. The preprocessor automatically creates the include file *DIM.INC* which contains the proper dimensioning. Thus the user does not have to change or adjust the dimensioning for the code at all.

4.3.3 Running the Code and Code Output

After the mesh has been processed and *femtetra.f* has been recompiled, the code is then ready to run. On page 31 is the input file for the rectangular patch, and a description for each line of input. The ouput file *yangferrircsy* is shown in Table 16 for the y-biased patch. A plot of the file is shown in Figure 14. Both biased and unbiased($4\pi M_s = 0$ G and $H_o = 0$ Oe) data are shown in the plot.

¹⁰See Section 3.1.1.

¹¹See [4].

¹²After compiling, the user must look at the file *DIM.INC* in order to ascertain the value needed for input for NXFFTP. This value should be set to the value of *MAXFFTP* in *DIM.INC*.

2	Option to run the code.
2	Chooses computation type(2=Normal FE-BI without AWE).
2	Specifies output data desired(2=Backscatter).
6.4,20.,35	Specifies frequency range: f_{start}, f_{stop} , number of frequency points.
rcscirc	Output file name.
0	Option to output electric field solution values(0=NO).
0	Option to normalize the Radar Cross Section(RCS).
0	Choose E field polarization angle, α (degrees) (0= $\theta - pol$).
2	Specifies cut(2= θ).
45.	Fixed start observation angle ϕ (degrees).
45.	Fixed start observation angle ϕ (degrees).
60.	Start observation angle θ (degrees).
60.	Start observation angle θ (degrees).
1	Number of observation points.
1	Number of fixed observation points.
0	Specifies desired solver(0=Symmetric BiCG).
.03	Specifies tolerance.
1	Option to implement AIM(1=yes) ¹¹ .
6,6	x-y integer threshold values for determining Z_{far}^{BI} and Z_{near}^{BI} .
47,94	Size of FFT grid(NXFFT) and FFT pad(NXFFTP); NXFFTP=2*NXFFT ¹² .
1	Check to see if input data is correct to this point(1=yes).
1	Specifies whether there are any anisotropic layers(1=yes).
1	Specifies isotropic, ferrite or general anisotropic material for each layer(1=ferrite).
1780.	$4\pi M_s$ value.
360.	H_o value.
0	Specifies whether bias is non-uniform or not(0=no).
0.	Linewidth(ΔH) value.
1	Direction of bias(1 = y-bias).

Table 15: Ferrite patch input file.

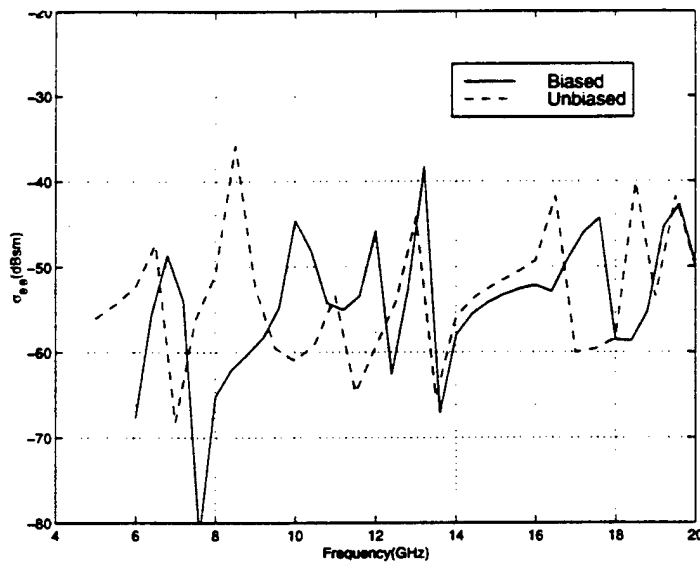


Figure 14: Plot of $\sigma_{\theta\theta}$.

The first column in Figure 16 is the backscatter angle θ (degrees), the second column is the backscatter angle ϕ (degrees), the third column is the frequency(GHz), the fourth column is σ (dBsm), the fifth column is $\sigma_{\theta\phi}$ (dBsm), the sixth column is $\sigma_{\theta\theta}$ (dBsm), the seventh column is the residual error, the eighth column is the time(sec.) it takes to solve for the unknown electric fields, and the ninth column is the number of iterations needed for convergence.

ϕ	θ	Freq(GHz)	σ	$\sigma_{\theta\phi}$	$\sigma_{\theta\theta}$	Res.	Time(s)	Iter.
45.000	60.000	6.400	-55.004	-63.503	-55.665	0.0263	5050.96	420
45.000	60.000	6.800	-47.834	-55.703	-48.609	0.0281	4020.92	286
45.000	60.000	7.200	-52.078	-56.610	-53.964	0.0212	4667.75	389
45.000	60.000	7.600	-66.251	-66.377	-81.703	0.0292	4165.59	299
45.000	60.000	8.000	-63.838	-69.537	-65.200	0.0284	3652.52	204
45.000	60.000	8.400	-61.424	-69.846	-62.099	0.0294	3799.83	207
45.000	60.000	8.800	-59.671	-68.418	-60.293	0.0297	3595.98	198
45.000	60.000	9.200	-57.619	-65.654	-58.362	0.0279	4244.96	275
45.000	60.000	9.600	-53.928	-61.069	-54.861	0.0291	5104.06	414
45.000	60.000	10.000	-43.544	-50.302	-44.572	0.0284	4453.91	300
45.000	60.000	10.400	-47.287	-54.831	-48.128	0.0286	4013.00	244
45.000	60.000	10.800	-53.797	-63.756	-54.259	0.0295	3925.36	234
45.000	60.000	11.200	-54.914	-68.964	-55.088	0.0247	3755.71	220
45.000	60.000	11.600	-53.402	-72.828	-53.451	0.0288	4204.11	308
45.000	60.000	12.000	-45.721	-67.884	-45.748	0.0287	4375.55	337
45.000	60.000	12.400	-62.062	-71.537	-62.582	0.0288	4868.86	414
45.000	60.000	12.800	-52.454	-65.255	-52.688	0.0225	4774.47	397
45.000	60.000	13.200	-37.413	-44.516	-38.354	0.0278	5583.75	525
45.000	60.000	13.600	-62.659	-64.600	-67.090	0.0285	3913.35	242
45.000	60.000	14.000	-57.752	-69.638	-58.043	0.0208	3861.77	225
45.000	60.000	14.400	-55.497	-72.225	-55.590	0.0296	3933.65	232
45.000	60.000	14.800	-54.167	-73.392	-54.219	0.0292	3913.48	229
45.000	60.000	15.200	-53.253	-73.352	-53.296	0.0287	3898.74	230
45.000	60.000	15.600	-52.574	-72.129	-52.623	0.0224	3944.39	255
45.000	60.000	16.000	-52.068	-69.457	-52.148	0.0295	4825.23	412
45.000	60.000	16.400	-52.393	-61.862	-52.914	0.0262	4337.27	328
45.000	60.000	16.800	-49.088	-68.792	-49.135	0.0251	4111.01	279
45.000	60.000	17.200	-45.704	-57.832	-45.979	0.0243	4143.86	289
45.000	60.000	17.600	-43.158	-49.604	-44.275	0.0275	5153.78	450
45.000	60.000	18.000	-56.564	-60.900	-58.559	0.0291	4267.26	300
45.000	60.000	18.400	-57.988	-66.222	-58.694	0.0276	4555.44	335
45.000	60.000	18.800	-55.211	-72.497	-55.293	0.0276	4514.57	345
45.000	60.000	19.200	-44.825	-54.051	-45.377	0.0272	5622.29	531
45.000	60.000	19.600	-42.380	-54.069	-42.685	0.0249	6569.80	713
45.000	60.000	20.000	-49.478	-59.978	-49.884	0.0259	4592.91	340

Table 16: Backscattering output file for ferrite rectangular patch.

References

- [1] A. Brown, Z. Li and J. Volakis, "Theory, Mesher and Users Manual for a Ferrite Finite Element-Boundary Integral Tetrahedral Code," University of Michigan Radiation Laboratory, Department of Electrical Engineering and Computer Science, Ann Arbor, MI, 1998
- [2] J. Jin and J.L. Volakis, "A hybrid finite element method for scattering and radiation by microstrip patch antennas and arrays residing in a cavity," *IEEE Trans. Antennas Propagat.*, vol. 39, no. 11, pp.1598-1604, 1991.
- [3] Y. Erdemli, C. J. Reddy and J. L. Volakis, "AWE technique in frequency domain electromagnetics," *J. Elec. Waves Appl.*, vol. 13, pp.359-377, 1999.
- [4] T. Eibert and J.L.Volakis, "Fast Spectral Domain Method for Hybrid Finite Element - Boundary Integral Modeling of Doubly Periodic Structures," University of Michigan Report #375458-3-T, Ann Arbor, MI, 1998
- [5] J.L.Volakis, J. Gong and A. Alexanian, "Electromagnetic scattering from microstrip patch antennas and spirals residing in a cavity," *Electromagnetics*, vol. 14, no. 1, pp.63-85, 1994.
- [6] H.Y. Yang, J.A. Castaneda, and N.G. Alexopoulos, "The RCS of a microstrip patch on an arbitrarily biased ferrite substrate," *IEEE Trans. Antennas Propagat.*, vol. AP-41, no. 12, pp. 1610-1614, 1993.

Appendix C: User's Manual for MR_Tetra: Multi-Resolution FE-BI Code

User manual for MR_TETRA.f : A multi-resolution finite element - boundary integral (FE-BI) code with hierarchical tetrahedral elements

Lars S. Andersen and John L. Volakis
Radiation Laboratory

Department of Electrical Engineering and Computer Science
University of Michigan
Ann Arbor, MI 48109-2122, USA

Abstract

The following is a manual for a multi-resolution finite element / boundary integral code for analysis of printed antennas backed by material-filled (dielectric or ferrite) metallic cavities recessed in infinite metallic ground planes. The main characteristic of the code is several attractive options for expanding the electric field within the cavity using lowest order, higher order or any combination of lowest and higher order hierarchical mixed-order tangential vector finite elements for tetrahedra.

1 Introduction

The following is a manual for a multi-resolution finite element / boundary integral (FE/BI) code (referred to as MR.TETRA in the following) for analysis of printed metallic antennas backed by material-filled metallic cavities recessed in infinite metallic ground planes. It is based on a standard FE/BI formulation where the cavity volume is discretized into tetrahedral elements using a FE approach and the mesh is rigorously truncated at the aperture surface using a BI [1]. The electric field within each tetrahedral element is expanded using hierarchical mixed-order tangential vector finite elements (TVFEs) of order 0.5 or 1.5 (referred to as lowest and higher order TVFEs in the following) as presented by Andersen and Volakis [2]. The resulting linear equation system is solved using an iterative solver. The matrix-vector products within the iterative solver can be carried out either directly or via a two-dimensional discrete Fourier transform (DFT) in the spectral domain through application of the adaptive integral method (AIM) [3]. A quasi minimal residual (QMR) [4] or conjugate gradient squared (CGS) [4] solver can be used in case matrix-vector products are computed directly while a QMR or biconjugate gradient (BCG) [4] solver can be used in

case matrix-vector products are computed using a DFT. Upon solution of the resulting linear equation system, input impedance and, optionally, near and far fields (patterns, polarization characteristics) are computed.

The purpose of this manual is to familiarize the reader with the steps involved in running MR_TETRA. This is achieved via a general description as well as a set of examples. It is not the purpose of this manual to demonstrate the merits of the approach on which the code is based. For such a demonstration, see for instance [5].

This manual is organized as follows. Section 2 provides a general description of how to run MR_TETRA. All relevant steps needed by the user will be presented. Section 3 outlines the construction of the input file for MR_TETRA. Section 4 offers a few examples of how to run MR_TETRA. Surface meshes, input files as well as results are given in order to demonstrate various capabilities of the code. Section 5 summarizes the manual.

2 General description of how to run MR_TETRA

The root directory of MR_TETRA consists of two sub-directories. The sub-directory `src` contains all source files (`.f`), parameter files (`.h`) and a makefile `MMR_TETRA`. Upon compilation, it will also contain all object files (`.o`). The executable `MR_TETRA` will be in the sub-directory `bin` where the input file `MR_TETRA.in` and the universal file describing the mesh (see below) must also be placed. Upon execution, this sub-directory will also contain all output files. The sub-directory `bin` further contains a sub-directory `plot` with MATLAB codes for plotting various output files. These MATLAB codes are not documented in this manual.

To run the code, the following steps must be followed :

1. A mesh in universal file format must be provided in the sub-directory `bin`.
2. In the sub-directory `src`, several dimensioning parameters in the file `param1.h` must be initialized. They must be estimated conservatively, otherwise the code will either crash or produce erroneous results. After a first run for a given mesh, they can manually be set to their smallest possible values for that particular mesh. The parameters are `Nnomax` (max number of nodes), `Nsnomax` (max number of metallic nodes), `Nedmax` (max number of edges), `Nsedmax` (max number of metallic edges), `Nfamax` (max number of triangular faces), `Nsfamax` (max number of metallic triangular faces), `Nmgmax` (max number of material groups), `Npredmax` (max number of probe edges), `Nhovolmax` (max number of higher order sections), `Nbifamax` (max number of triangular BI faces), `Nbiedmax` (max number of BI edges), `IAIMmax` (max number of AIM grid points in the *x*-direction), `JAIMmax` (max number of AIM grid points in the *y*-direction), `IJAIMmax` (max of `IAIMmax` and `JAIMmax`) and `Nnffamax` (max number of near field triangular AIM faces). Note that the file `param1.h` contains several additional dimensioning parameters. These have been set conservatively so the code will run for fully higher order cavities without AIM. This, however, is a tremendous overkill if lowest order

TVFEs and AIM is applied. The user is highly advised to familiarize himself / herself with these parameters and set them optimally for each application. Specifically, **BWmax1** and **Nunkmax** can be lowered from 100 and $2*\text{Nedmax}+2*\text{Nfamax}$ to 30 and **Nedmax** if only lowest order TVFEs are applied and **Nmatmax** can be lowered from $\text{BWmax1}*\text{Nunkmax}+\text{Nbiedmax}^{**2}$ to **BWmax1*Nunkmax** if AIM is used. This will lead to significant memory savings without altering the results.

3. Build the executable **MR_TETRA** (type `make -f MMR_TETRA` in the sub-directory `src`¹).
4. Construct the input file **MR_TETRA.in** in the sub-directory `bin` (see below).
5. Run the code (type **MR_TETRA** in the sub-directory `bin`).

3 Construction of input file

The input file for **MR_TETRA** can be broken into 12 different sections. The format of each of these 12 sections will be described below. “I” denotes an integer, “R” denotes a double precision real number and “C” denotes a double precision complex number. “Text” denotes a text line that allows the user to describe the following input parameter(s). Information in all such lines is irrelevant to the code but it makes the input file easier to read and hereby easier to modify. We note that some parts seem unnecessary or redundant. This is partly due to the fact that the code has more options than those described in this manual and partly a result of convenient choices made while the code was under development. We also note that the following description is very general and that specific examples follow later in the report.

Section 1

This section describes the universal file that represents the mesh. Users unfamiliar with universal file formats are referred to SDRC I-DEAS manuals. A universal file section with the descriptor 2411 must give the node coordinates in cm (the ground plane and the metallic antenna must be in the plane $z = 0$ and the cavity must be in the half space $z < 0$). A universal file section with the descriptor 2412 must give the element connectivity and a material group for each element. Optionally, a universal file section with descriptor 2417 (used to describe groups of nodes) and name starting with “F” can be added. This section is used for describing the metallic triangular faces forming the printed antenna. Each node triplet describes a metallic face and hence the group will contain three times as many nodes as there are metallic faces. Note that this is the only way to uniquely describe the metallic antenna. For simple geometries, it can be done with nodes alone or with node doublets (edges) but in the general case node triplets (triangular faces) must be used. **MR_TETRA** allows easy specification of rectangular and circular patches via simple geometrical parameters (see Section 2). In these cases, a universal file section with descriptor 2417 is unnecessary. Note that the universal file can be generated using SDRC I-DEAS, the automatic mesher written at

¹We note that the compilation of source files was tested on a SUN ULTRA30 work station. Certain parts of the makefile **MMR_TETRA** as well as the timing commands in the code may have to be modified on other platforms.

the University of Michigan or any other meshing package capable of producing a tetrahedral mesh described in universal file format. The format of this section is the following :

```
Text
"filename" : Universal file
```

Section 2

This section describes the metallic cavity and, optionally, the metallic patch. A cavity code is 1 / 2 for a rectangular / circular cavity. In the former case, $(x, y, z)_{start}$ and $(x, y, z)_{stop}$ for the rectangular cavity as well as $(x, y)_{start}$ and $(x, y)_{stop}$ for a rectangular patch in the plane $z = 0$ is given. In the latter case, the radius r_{cavity} and height h_{cavity} of a circular cavity centered at $(0, 0, -h_{cavity}/2)$ as well as the radius r_{patch} of a circular patch centered at $(0, 0, 0)$ is given. For cavities where the metallic faces are described in the universal file, all patch parameters should be set to zero. The format of this section is either of the following :

```
Text
1 : Cavity code (rectangular cavity)
```

```
Text
R : x_cavity_start
R : y_cavity_start
R : z_cavity_start
R : x_cavity_stop
R : y_cavity_stop
R : z_cavity_stop
R : x_patch_start
R : y_patch_start
R : x_patch_stop
R : y_patch_stop
```

```
Text
2 : Cavity code (circular cavity)
```

```
Text
R : r_cavity
R : h_cavity
R : r_patch
```

Section 3

This section describes the probe excitation. Each probe has unit magnitude and zero phase and must start and end at a node in the mesh. A probe code (must be 1) and the number of probes is given along with $(x, y, z)_{start}$ and $(x, y, z)_{stop}$ for each probe. The format of this section is the following :

```

Text
1 : Probe code
Text
I : Number of probes
Text
R : x_probe_start
R : y_probe_start
R : z_probe_start
R : x_probe_stop
R : y_probe_stop
R : z_probe_stop
}

```

Repeated for each probe

Section 4

This section describes the higher order sections in the mesh. A higher order code of 0 / 1 / 2 indicates that no higher order TVFEs are used / that higher order TVFEs are contained within rectangular brick sections of the mesh (for rectangular cavities) / that higher order TVFEs are contained within cylindrical shell sections of the mesh (for circular cavities). In case higher order TVFEs are used, the number of higher order sections is given along with a geometrical description of each higher order section. For rectangular brick sections, $(x, y, z)_{start}$ and $(x, y, z)_{stop}$ are given. The higher order section is then the brick having these points as opposite corners. For cylindrical shell sections, the inner and outer radii r_{start} and r_{stop} and the azimuthal angles ϕ_{start} and ϕ_{stop} are given. ϕ_{start} and ϕ_{stop} must be in degrees and be in the interval $[0^\circ, 360^\circ]$. The higher order section is then the shell from r_{start} to r_{stop} radially, from ϕ_{start} to ϕ_{stop} (counter-clockwise) azimuthally and from $-h_{cavity}$ to 0 in the z -direction. The format of this section is either of the following :

```

Text
0 : Higher order code (no higher order TVFEs)

Text
1 : Higher order code (rectangular cavity)
Text
I : Number of higher order sections
Text
R : x_ho_start
R : y_ho_start
R : z_ho_start
R : x_ho_stop
R : y_ho_stop
R : z_ho_stop
}

```

Repeated for each higher order section

```

Text
2 : Higher order code (circular cavity)
Text
I : Number of higher order sections
Text
R : r_ho_start
R : r_ho_stop
R : phi_ho_start
R : phi_ho_stop
} Repeated for each higher order section

```

Section 5

This section describes the TVFEs used for field expansion. A TVFE code 1 / 3 indicates that lowest order TVFEs / a combination of lowest and higher order TVFEs are used. Note that for a TVFE code of 1, the information about higher order TVFEs in Section 4 is not used. This allows the user to toggle between lowest order TVFEs and a combination of lowest and higher order TVFEs by changing only the TVFE code. The format of this section is the following :

```

Text
I : TVFE code

```

Section 6

This section describes the different material groups. The number of material groups is given. For each material group, the relative permittivity and permeability tensor is described. The former is described by the nine elements $\epsilon_{xx}, \dots, \epsilon_{zz}$ and a conductivity σ in S/cm that gives rise to a frequency dependent loss. The latter is either the unit tensor or a Polder tensor for a gyrotropic material. It is described by a bias code (0 means a unit tensor while 1 / 2 / 3 means a Polder tensor with x- / y- / z-bias) and the value of the precession and saturation frequencies f_0 and f_m in Hz [6]. The format of this section is the following :

```

Text
I : Number of material groups
Text
C : epsilon_xx
C : epsilon_xy
C : epsilon_xz
C : epsilon_yx
C : epsilon_yy
C : epsilon_yz
C : epsilon_zx
C : epsilon_zy
C : epsilon_zz
R : sigma
I : Bias axis
R : f_0
R : f_m
} Repeated for each material group

```

Section 7

This section describes the orders of the Gauss-Legendre integrations for computing the FEM matrix elements. BI near zone elements, BI far zone elements and far fields. The first type of integration is a volume integration over a tetrahedron where an integer 1 / 2 / 3 / 4 denotes 1- / 4- / 5- / 11-point Gauss-Legendre integration. The last three types of integrations are surface integrations over triangles where an integer 1 / 2 / 3 / 4 denotes 1- / 3- / 4- / 7-point Gauss-Legendre integration. The integration order for FEM should be at least 2 for lowest order TVFEs and 4 for higher order TVFEs if exact results are desired. Since accurate evaluation of the near zone elements in the BI matrix is crucial for accurate analysis, the integration order for the BI near zone elements should be set to 4. The integration order for the far zone elements in the BI matrix is usually set to 1 but can be increased to give slightly more accurate results at the price of a significantly slower code. The integration order for far fields is usually set to 4. The format of this section is the following :

```
Text
I : Integration order for FEM
I : Integration order for BI_near
I : Integration order for BI_far
I : Integration order for far field
```

Section 8

This section describes the frequencies at which the geometry is analyzed. The start and stop frequency in Hz as well as the number of frequency points is given. The format of this section is the following :

```
Text
R : f_start
R : f_stop
Text
I : Number of frequency points
```

Section 9

This section describes the iterative solver used for solving the resulting matrix equation system as well as the tolerance imposed on the relative residual as a stopping criterion. A solver code of 1 indicates a QMR solver. A solver code of 2 indicates a CGS solver for the case where matrix-vector products are computed directly and a BCG solver for the case where AIM is applied and matrix-vector products are computed using a DFT. The format of this section is the following :

```
Text
I : Solver code
Text
R : Solver tolerance
```

Section 10

This section describes whether AIM is used as well as all AIM parameters. An AIM code 0 / 1 indicates that AIM is not / is used. Regardless of the AIM code, $(x, y)_{start}$ and $(x, y)_{stop}$ for the AIM grid are given along with the number of AIM grid points in the x - and y -direction and the number of near zone AIM grid points in both directions. This information is not used when AIM is not used. Reading the information anyway allows the user to toggle between direct and DFT computation of matrix-vector products by changing only the AIM code. The format of this section is the following :

```
Text
I : AIM code
Text
R : x_AIM_start
R : y_AIM_start
R : x_AIM_stop
R : y_AIM_stop
I : N_AIM_x
I : N_AIM_y
I : N_AIM_near
```

Section 11

This section describes whether near and far field distributions are computed. For near fields, a near field code of 0 / 1 indicates that they are not / are computed. For far fields, a far field code of 0 / 1 / 2 / 3 indicates that nothing / patterns only / polarization characteristics only / patterns and polarization characteristics are computed. For near fields, the cavity is sampled in 33×33 points in 4 equidistant planes from the bottom of the cavity to the top, as illustrated in Fig. 1. The file `xypy.dat` has $33 \cdot 33 = 1089$ lines containing the values of (x, y) for the sample points in the plane $z = 0$. The file `FxFy.dat` has $33 \cdot 33 = 1089$ lines containing the corresponding values of the real part of the x - and y -directed electric field as well as the imaginary part of the x - and y -directed electric field. This surface electric field is the one that is being radiated (as an equivalent magnetic current) to give the far field. The file `xypyzp.dat` has $33 \cdot 33 \cdot 4 = 4356$ lines containing the values of (x, y, z) for the sample points in the 4 planes. The file `Fmgn.dat` has $33 \cdot 33 \cdot 4 = 4356$ lines containing the corresponding magnitudes $\sqrt{|E_x|^2 + |E_y|^2 + |E_z|^2}$ of the electric field. Note that an expert user can easily alter the routine `nearfielddist.f` to compute whatever near field quantity might be of interest or to change the sampling rate. For far fields, the half space above the antenna is sampled in $36 \times 16 = 576$ far field points (36 θ -values in $[0^\circ, 90^\circ]$ and 16 ϕ -values in $[0^\circ, 360^\circ]$ with θ and ϕ being the traditional polar and azimuthal angles of a spherical coordinate system related to the (x, y, z) -coordinate system). The file `ff.dat` has $36 \cdot 16$ lines containing the values of θ and ϕ along with a quantity proportional to $\sqrt{|E_\theta|^2 + |E_\phi|^2}$ in the far field. Note that an expert user can easily alter the routine `farfielddist.f` to compute whatever far field quantity might be of interest or to change the sampling rate. The file `pol.dat` contains information about the polarization of the far field normal to the plane of the antenna. It gives the axial ratio (in dB) of the polarization ellipse, the phase

difference (in degrees) between the two components and the tilt angle (in degrees) of the polarization ellipse measured from the x -axis. The format of this section is the following :

```
Text
I : Near field code
Text
I : Near field code
```

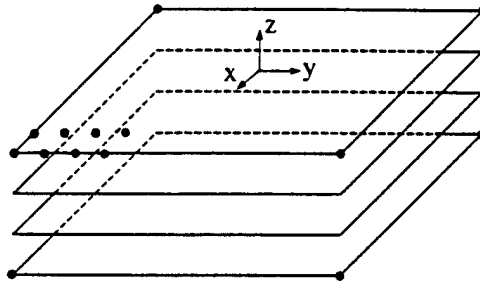


Figure 1: Illustration of cavity sampling.

Section 12

This section describes file names of output files containing geometrical parameters, input impedance information (the real and imaginary part of the input impedance for each frequency), convergence information (the number of iterations and the final relative residual for each frequency) and timing information (the time for the FEM part, BI part and solver for each frequency as well as time for pre-processing and “the rest of the code”). The format of this section is the following :

```
Text
"filename" : Geometry file
Text
"filename" : Impedance file
Text
"filename" : Convergence file
Text
"filename" : Timing file
```

4 Examples

Consider a square metallic patch antenna backed by a rectangular cavity recessed in an infinite metallic ground plane, as illustrated in Fig. 2 (side view) and Fig. 3 (top view). The cavity-backed patch antenna is situated in free space characterized by the permittivity ϵ_0 and the permeability μ_0 . The cavity is of dimensions $1.85 \text{ cm} \times 1.85 \text{ cm} \times 0.15 \text{ cm}$ and filled with a dielectric material of permittivity $10 \epsilon_0$ and conductivity 0.0003 S/cm . The patch is of side length 0.925 cm and centered in the cavity aperture. It is fed by a vertical coaxial

line whose outer conductor is attached to the ground plane and whose inner conductor is attached to the patch at the mid point of an edge, as illustrated in Fig. 2 and Fig. 3. The coaxial feed will be modeled as a vertical probe of constant current.

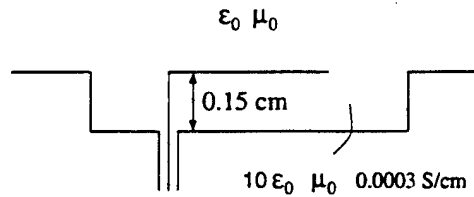


Figure 2: Side view of square metallic patch antenna backed by a dielectric-filled rectangular cavity recessed in an infinite metallic ground plane.

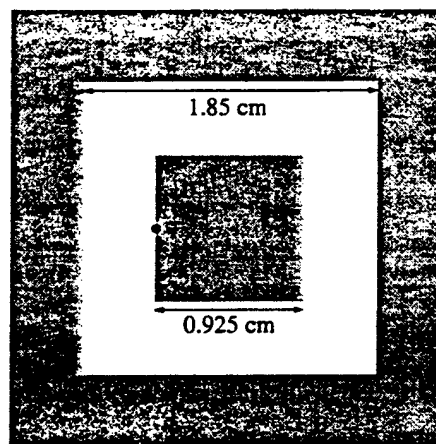


Figure 3: Top view of square metallic patch antenna backed by a dielectric-filled rectangular cavity recessed in an infinite metallic ground plane.

A coarse surface mesh is given in Fig. 4. For mixed-order TVFEs of order 0.5 and 1.5, the particular mesh is too coarse to yield the exact resonant frequency of 4.43GHz as obtained by Schuster and Luebbers [7] and confirmed by Andersen and Volakis for finer meshes [5]. Nevertheless, the mesh is very useful for illustrating the capabilities of MR_TETRA.

Let us analyze the above antenna at 21 frequency points in the interval [3.5GHz,4.5GHz]. We will solve resulting linear equation system using a QMR solver with tolerance 10^{-3} . AIM will not be used. The input file is given below.

```

Name of universal file
"mesh.unv"
PEC code
1
(x,y,z)_start, (x,y,z)_stop, (x_pa,y_pa)_start, (x_pa,y_pa)_stop
-0.4625d0
-0.4625d0

```

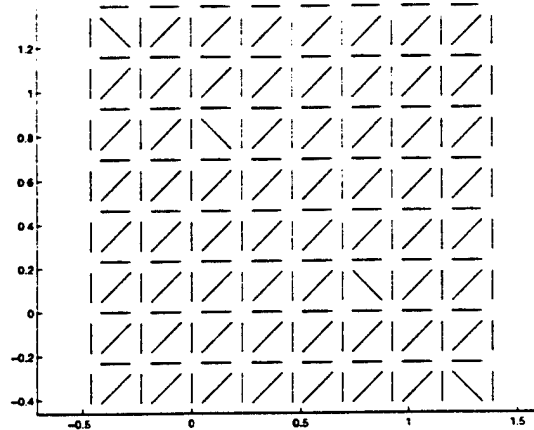


Figure 4: Top view of coarse surface mesh for square metallic patch antenna backed by a dielectric-filled rectangular cavity recessed in an infinite metallic ground plane.

```

-0.15d0
1.3875d0
1.3875d0
0d0
0d0
0d0
0.925d0
0.925d0
Probe code
1
Number of probes
1
(x_pr,y_pr,z_pr)_start, (x_pr,y_pr,z_pr)_stop for first probe
0d0
0.4625d0
-0.15d0
0d0
0.4625d0
0d0
H0 code
0
TVFE code
1
Number of material groups
1
Parameters for the first group
(10d0,-0d0)
(0d0,-0d0)
(0d0,-0d0)
(0d0,-0d0)

```

```
(10d0,-0d0)
(0d0,-0d0)
(0d0,-0d0)
(0d0,-0d0)
(10d0,-0d0)
0.0003d0
0
0d0
0d0
Integration order : FEM, BI_near, BI_far and farfield
4
4
1
4
Start and stop frequencies
3.50d9
4.50d9
Number of frequency points
21
Solvercode
1
Tolerance
1d-3
AIM code
0
AIM parameters (x_start, y_start, x_stop, y_stop, I, J, K)
0d0
0d0
0d0
0d0
0
0
0
Near field distribution code
0
Far field distribution code
0
Name of file with geometrical data
"3D-FEM-BI.out1"
Name of file with input impedances
"3D-FEM-BI.imp1"
Name of file with convergence data
"3D-FEM-BI.con1"
Name of file with timing data
"3D-FEM-BI.tim1"
```

The output file containing the input impedance for each frequency is given below and also plotted in Fig 5. The antenna is seen to experience the expected resonant behavior. Also, the resonant frequency is seen to be around 3.97GHz which is much smaller than the true resonant frequency 4.43GHz. This is due to the coarse mesh and the fact that lowest order TVFEs have been used.

3500000000.0000	2.5588456293470	41.628451744725
3550000000.0000	3.2429206914211	45.778072533465
3600000000.0000	4.2286657863228	50.904979316993
3650000000.0000	5.7163554782377	57.440189012613
3700000000.0000	8.1003200176110	66.098467821245
3750000000.0000	12.236883071922	78.132689480470
3800000000.0000	20.294341985730	95.967863359927
3850000000.0000	38.929881217035	124.44216366128
3900000000.0000	94.338002704657	169.57056063719
3950000000.0000	278.78777970206	152.06654344528
4000000000.0000	248.05473459466	-138.59626984899
4050000000.0000	87.641136274513	-133.27080997795
4100000000.0000	39.664558360104	-92.517092077889
4150000000.0000	22.234424951724	-66.678035812629
4200000000.0000	14.241706452950	-50.108946578041
4250000000.0000	9.9540096442860	-38.749056086777
4300000000.0000	7.3944826938964	-30.493855847262
4350000000.0000	5.7400309760047	-24.197511427906
4400000000.0000	4.6063185864701	-19.211509191283
4450000000.0000	3.8071120800757	-15.235725559360
4500000000.0000	3.2156270709780	-11.848352913871

At the resonant frequency 3.97GHz, let us now look at the polarization of the far field normal to the antenna as well as the far field patterns. Hence, we change Section 8 and 11 of the input file to read

Start and stop frequencies

3.97d9

3.97d9

Number of frequency points

1

Near field distribution code

0

Far field distribution code

3

The polarization of the far field normal to the antenna is described in the file **pol.dat** :

3970000000.0000		
26.122202028302	-85.365890875233	0.23007593744868

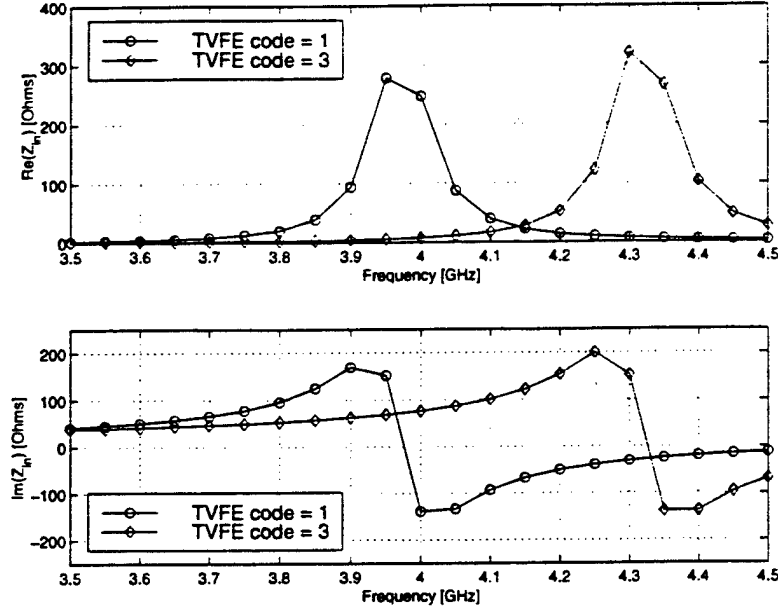


Figure 5: Real and imaginary part of the input impedance of the antenna in Fig. 2 and Fig. 3.

This output implies that the polarization ellipse is tilted 0.23° from the x -axis and has an axial ratio of 26.12dB. That is, we essentially have linear polarization along the x -axis which is what we expect for this patch. The patterns in the planes $y = 0$ and $x = 0$ at 3.97GHz are given in Fig. 6 (polar angles in $[0^\circ, 90^\circ]$ on the plot corresponds to ϕ -values in $[0^\circ, 180^\circ]$ while polar angles in $[90^\circ, 180^\circ]$ on the plot corresponds to ϕ -values in $[180^\circ, 360^\circ]$; also, the polar angle 90° on the plot corresponds to $\theta = 0^\circ$ and the polar angles 0° and 180° correspond to $\theta = 90^\circ$). These are consistent with the polarization of the far field normal to the antenna and exactly what we expect for this patch.

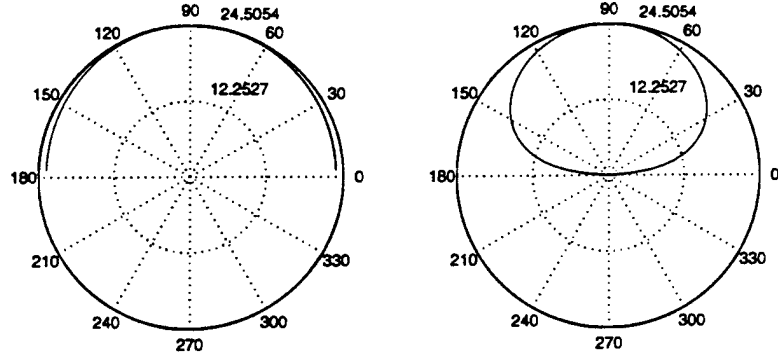


Figure 6: Patterns in the planes $y = 0$ and $x = 0$ at 3.97GHz for the antenna in Fig. 2 and Fig. 3.

To demonstrate the use of higher order TVFEs for improved field modeling, we apply higher order TVFEs around the radiating edges of the patch where the field is known to be the strongest and experience the most variation. Hence, we change Section 4 and 5 of the input file to read

```

HO code
1
Number of higher order volumes
2
(x,y,z)_start, (x,y,z)_stop for first higher order volume
-0.23125d0
-0.23125d0
-0.15d0
0.23125d0
1.15625d0
0d0
(x,y,z)_start, (x,y,z)_stop for second higher order volume
0.69375d0
-0.23125d0
-0.15d0
1.15625d0
1.15625d0
0d0

```

TVFE code

3

Let us consider the application of AIM and use a DFT to compute the matrix-vector products in the iterative solver. This is terribly inefficient for small problems like the one considered here and only serves the purpose of demonstrating how AIM is used. To invoke AIM. we change Section 10 of the input file to read

```

AIM code
1
AIM parameters (x_start, y_start, x_stop, y_stop, I, J, K)
-0.668055555555d0
-0.668055555555d0
1.593055555555d0
1.593055555555d0
23
23
8

```

The output file containing the input impedance for each frequency is given below and also plotted in Fig 5. The antenna is again seen to experience the expected resonant behavior. The resonant frequency is seen to be 4.32GHz which is much closer to the true resonant frequency 4.43GHz than the 3.97GHz found when lowest order TVFEs were used throughout the cavity.

3500000000.0000	1.0325245571199	37.824886278503
3550000000.0000	1.1787602915226	39.744351943887
3600000000.0000	1.3630059719665	41.855292671137

3650000000.0000	1.5908198292434	44.211407702366
3700000000.0000	1.8827809279585	46.855809984373
3750000000.0000	2.2511366594008	49.890077408460
3800000000.0000	2.7452949855043	53.404271011424
3850000000.0000	3.4128718362669	57.554844531757
3900000000.0000	4.3376897449660	62.542584004342
3950000000.0000	5.6748167344092	68.707629601590
4000000000.0000	7.6934532336221	76.555049192618
4050000000.0000	10.930495769666	86.945891370685
4100000000.0000	16.607146734682	101.292500931489
4150000000.0000	27.615471055343	122.03417410905
4200000000.0000	52.159382628536	154.29204802524
4250000000.0000	122.49555861383	200.49906174576
4300000000.0000	320.78659000805	152.29837557693
4350000000.0000	267.24188214807	-137.93155070714
4400000000.0000	103.160187785883	-137.62354804365
4450000000.0000	48.490909355324	-96.045352685244
4500000000.0000	27.621340718090	-67.895949125991

5 Summary

This manual describes how to run MR_TETRA, a multi-resolution finite element / boundary integral code for analysis of printed antennas backed by material-filled (dielectric or ferrite) metallic cavities recessed in infinite metallic ground planes. Both a general description as well as examples are given.

References

- [1] J.L. Volakis, A. Chatterjee, and L.C. Kempel. *Finite element method for electromagnetics*. IEEE Press, USA, 1998.
- [2] L.S. Andersen and J.L. Volakis. 'Hierarchical tangential vector finite elements for tetrahedra'. *IEEE Microwave and Guided Wave Letters*, vol. 8, pp. 127-129, March 1998.
- [3] E. Bleszynski, M. Bleszynski, and T. Jaroszewicz. 'AIM: Adaptive integral method for solving large-scale electromagnetic scattering and radiation problems'. *Radio Sci.*, vol. 31, pp. 1225-1251, 1996.
- [4] Y. Saad. *Iterative methods for sparse linear systems*. PWS Publishing Company, 1996.
- [5] L.S. Andersen and J.L. Volakis. 'Accurate and efficient simulation of antennas using hierarchical mixed-order tangential vector finite elements for tetrahedra'. Accepted for publication in *IEEE Trans. Antennas Propagat.*
- [6] D.M. Pozar. *Microwave engineering*. Addison-Wesley Publishing Company, Inc., 1990.
- [7] J.W. Schuster and R. Luebbers. Private communication.

Appendix D: User's Manual for Structured 2D and 3D Meshing

Structured 2-D and 3-D Meshing of Antenna Surfaces and Volumes: Users Manual Version 2

Zhifang Li and John L. Volakis
Radiation Laboratory

Department of Electrical Engineering and Computer Science

University of Michigan, Ann Arbor, MI 48109-2122

Email: zhifang@umich.edu, volakis@umich.edu

July 1999

Contents

1	Introduction	3
1.1	New Features for Version 2	3
1.2	Features of the Mesher	3
2	How to Use the Mesher	5
2.1	User-specified geometry	5
2.1.1	Single rectangular patch	5
2.1.2	Single circular patch	5
2.1.3	Rectangular arrays	6
2.2	SurfMesh file pre-supplied	7
2.3	Viewing the surface mesh in MatLab	8
2.4	Output files	8
3	Appendix. Disk Contents	9

1 Introduction

This manual is a supplement to a previous version (see "Theory, Mesher and Users Manual for a Ferrite Finite Element-Boundary Integral Tetrahedral Code" by Arik Brown, Zhifang Li and John L. Volakis, Rad Lab Report 036307-2-T, University of Michigan, May 1998) but can also be used independently. It describes a complete 2-D and 3-D mesher package for antenna patches or slots. All codes are written in FORTRAN 77.

1.1 New Features for Version 2

Because boundary integral (BI) truncation is more popular than the artificial absorber (AA) truncation, this new version considerably facilitates the meshing process for BI. The user specifies the geometric and electric parameters only once, and the codes will automatically run through the surface and volume mesh to generate an IDEAS-compatible universal file. New features of version 2 include:

- For BI truncation, one-step run of surface and volume mesh is available for rectangular and circular geometries;
- The mesher can start either from simple geometry inputs or an outside-supplied SurfMesh file and generate a volume mesh accordingly;
- Infinite/finite array geometry accepted.

1.2 Features of the Mesher

- The meshers can mesh patch or slot antennas of rectangular, circular, or log-periodic geometry;
- The mesh is terminated by either boundary integral (BI) or artificial absorber (AA) truncation;
- For BI truncation, non-uniform surface mesh is available of rectangular or circular geometry (log-periodic is intrinsically non-uniform);
- For AA truncation, meshing is done in two steps: surface first and then growing to volume; all rectangular, circular and log-periodic geometries are accepted;
- For AA truncation, cavity or microstrip configuration are both available; while for BI truncation only cavity configuration is available;
- In meshing the 3-D structure, either prismatic or tetrahedral elements can be chosen;
- Surface mesh can be viewed with Matlab; and Volume mesh is in the form of universal file, which is compatible with commercial software I-DEAS;

- The 3-D mesher is additionally capable of meshing non-planar platforms for circular antennas with BI termination;
- Multiple layers of substrates and/or superstrates can be dealt with;
- Multiple probe feeds coinciding with edges can be specified within the mesher.

In this manual, we will only provide brief usage when the geometry is terminated by BI truncation. For more illustrated examples and detailed instructions on AA truncation, please refer to the manual of Version 1: "Theory, Mesher and Users Manual for a Ferrite Finite Element-Boundary Integral Tetrahedral Code" by Arik Brown, Zhifang Li and John L. Volakis, Rad Lab Report 036307-2-T, University of Michigan, May 1998.

2 How to Use the Mesher

If you do not have any file at hand and would like to specify the geometry from scratch, please read section 2.1. If you already have a surface mesh and would like to expand it to volume mesh, please go directly to section 2.2.

2.1 User-specified geometry

2.1.1 Single rectangular patch

If you would mesh a single rectangular patch, you need to:

1. Compile the code 'meshrect.f':
f77 meshrect.f -o meshrect.e
2. Run the mesher by typing: *meshrect.e* and then hit return. Input your geometry as prompted by the code, which is self-explained. A sample file is shown in Table 1.

0	1 = cavity only; 0 = patch/slot
1	1 = patch; 0 = slot
0.5 0.5	Element size (cm) between antenna and cavity wall (x,y)
2 2	Number of elements between antenna and cavity wall (x,y)
0.25 0.25	Element size (cm) of antenna (x,y)
6 4	Number of antenna elements (x,y)
1	1 = Tetra; 0 = Prism
2	Number of substrate layers
0	1 = same thickness; 0 = no
0.1	Thickness (cm) of substrate layer 1 (from bottom up)
0.15	Thickness (cm) of substrate layer 2
1	Material code of substrate layer 1
2	Material code of substrate layer 2

Table 1: Sample input file for mesh of a single rectangular patch.

2.1.2 Single circular patch

If you would mesh a single circular patch, you need to:

1. Compile the code 'meshcirc.f':
f77 meshcirc.f -o meshcirc.e
2. Run the mesher by typing: *meshcirc.e* and then hit return. Input your geometry as prompted by the code, which is self-explained. A sample file is shown in Table 2.

0 1 = cavity only; 0 = patch/slot
 1 1 = patch; 0 = slot
 0.75 Element size (cm) of rings between antenna and cavity wall
 4 Number of rings between antenna and cavity wall
 1. Element size (cm) of antenna rings
 3 Number of antenna rings
 1 1 = Tetra; 0 = Prism
 1 Number of substrate layers
 0.1 Thickness (cm) of substrate layer 1 (from bottom up)
 Material code automatically assigned to be 1 for single layer

Table 2: Sample input file for mesh of a single circular patch.

2.1.3 Rectangular arrays

If you would mesh a rectangular array, you need to:

1. Compile the code 'meshrect_arr.f':
`f77 meshrect_arr.f -o meshrect_arr.e`
2. Run the mesher by typing: *meshrect_arr.e* and then hit return. Input your geometry as prompted by the code, which is self-explained. A sample file is shown in Table 3.

This code can also be used to mesh a single rectangular patch.

0 all surface nodes resistive? (1 = yes, 0 = no)
 1 Patch (= 1) or Slot (= 0)
 3 2 Number of patches in x- and y-direction
 0.2 0.2 Element size (cm) dX and dY
 4 4 Number of edges for every patch (x, y)
 2 2 Number of edges between LL patch and cavity wall (x, y)
 2 Number of edges between neighboring patches in x direction(>=2)
 1 Number of edges between neighboring patches in y direction(>=2)
 1 1 = Tetra; 0 = Prism
 1 Number of substrate layers
 0.1 Thickness (cm) of substrate layers

Table 3: Sample input file for mesh of a rectangular array.

2.2 SurfMesh file pre-supplied

If the user already has a surface mesh and would like to grow it to a 3-D volume mesh with prismatic or tetrahedral elements, he needs to have a file called 'SurfMesh' before running the volume mesh. The 'SurfMesh' file should have the format shown in Table 4.

40 278 278 164 164 0	no. of antenna tri, cavity tri, total tri, cavity nodes, total nodes. and absorber tri (for BI, 2nd entry = 3rd entry, 4th entry = 5th entry, and 6th entry = 0)
1 2 19 14	triangle number and the global numbering of its three nodes
...	...
1 .0 -2.0 .0	node number and its (x,y,z) coordinates
...	...

Table 4: Sample SurfMesh file.

Note: antenna triangles should be listed first, followed by non-antenna triangles.

After the SurfMesh file is generated, the user is ready to grow it to 3-D volume mesh. The steps are very simple:

1. Compile the code 'surfproc.f':
f77 surfproc.f -o surfproc.e
2. Run *surfproc.e*. This code reads in the 'SurfMesh' file and modifies it to get ready for the volume mesh.
3. Compile the code 'volproc.f':
f77 volproc.f -o volproc.e
4. Run *volproc.e*. This code conducts the volume mesh.

2.3 Viewing the surface mesh in MatLab

After the mesh has been generated, the 2-D surface mesh can be viewed in Matlab. There are several m files in the directory which can do different tasks. They are:

Setup sets up the screen and reads in the mesh data. Must be issued first prior to other MatLab commands.

Mesh displays the mesh.

GloNod numbers the nodes globally.

LocNod numbers the nodes locally with respect to each triangle.

TriNum numbers the triangular patches.

AngDst plots on a second window the distribution of internal angles in the mesh (this is useful for assessing the quality of the mesh).

Bound displays geometry with mesh in the background.

After the creation of the surface mesh, the user can start MatLab and issue the above commands as needed. Among the commands listed above, the most important one is the **GloNod**. This is a must for specifying feed location in the 'MainIn' file for the input of the 3-D mesher. Another important note is that the user must run 'Setup' first before running the command 'Mesh'.

2.4 Output files

Several auxiliary files will be created after the above procedures. Among them 'SurfMesh' is the 2-D surface file which could be used by Matlab to display the mesh. 'mesh.unv' is the 3-D universal file which is compatible for commercial software I-DEAS.

3 Appendix. Disk Contents

This is a list of directories and all files in this delivery.

DIRECTORY *src* contains all codes and files for the 2-D and 3-D meshers.

AngDst.m MatLab code to plot the internal angle distribution in the mesh.

AngInt contains information of distribution of internal angles created by surface mesher.

AntEdg contains information of antenna edges created by surface mesher.

ArrayDetector.f code needed in array meshing.

Attr file needed for surface mesh display.

Bound.m MatLab code to display surface geometry with mesh in the background.

CavEdg contains information of cavity edges created by surface mesher.

GloNod.m MatLab code to number nodes globally.

LocNod.m MatLab code to number nodes locally with respect to each triangle.

MainIn input file for *VolumeMesher.f*.

Mesh.m MatLab code to display the surface mesh.

MeshDs file generated for surface mesh display.

MesherScript a script file used internally by the mesher.

Plot.aux contains the statement 'axis('equal')' in its first line.

Setup.m MatLab code to set up the screen and read in the surface mesh data.
Must be issued prior to other MatLab commands.

SrfEdg contains information of surface edges created by surface mesher.

SurfChecker.f code to check the user-supplied 'SurfMesh' file and modify it to be used by volume mesher.

SurfIn input file for *SurfMesher.f*.

SurfMesh surface mesh file created by surface mesher.

SurfMesh.old if the SurfMesh file supplied by the user has been modified during the volume mesh, the original SurfMesh file will be saved in SurfMesh.old file.

SurfMesherBI.f FORTRAN code of the surface mesher.

SurfReader.f code to read in the 'SurfMesh' supplied by user and make necessary modifications.

TriNum.m MatLab code to number the triangles in surface mesh.

VolumeMesherBI.f FORTRAN code of the volume mesher.

dm.f FORTRAN code to read in the SurfMesh file and create a decent 'fema.dml' file before running volume mesh.

fema.dml contains the parameter statement for memory allocation.

fema.dm2 contains the parameter statement for memory allocation of circular patch.

mesh.unv universal file generated by volume mesher to view the mesh in I-DEAS.

meshcirc.f code to conduct BI mesh of single circular patch.

meshrect.f code to conduct BI mesh of single rectangular patch.

meshrect_arr.f code to conduct BI mesh of rectangular array.

surfproc.f code to read in a user-supplied 'SurfMesh' file and modify it to be used by volproc.f.

volproc.f code to conduct volume mesh with a pre-supplied surface mesh.

DIRECTORY *document* contains all the manuals and documents for the 2-D and 3-D mesher package.

manual.tex User's manual for the structured 2-D and 3-D mesher package (in La-Tex format).

manual.ps Postscript file of the manual.

example_array example input file for rectangular array mesh.

example_circ example input file for circular patch mesh.

example_rect example input file for rectangular patch mesh.